Calibration and Application of a Tidal-Timescale Sediment Transport Model for Simulation of Estuarine Geomorphic Change Under Future Scenarios

By

NEIL KAMAL GANJU
B.S. (University of Michigan, Ann Arbor) 1998
M.S. (University of Florida, Gainesville) 2001

DISSERTATION

Submitted in partial satisfaction of the requirements for the degree of

DOCTOR OF PHILOSOPHY

in

Civil and Environmental Engineering

in the

OFFICE OF GRADUATE STUDIES

of the

UNIVERSITY OF CALIFORNIA

DAVIS

Approved:

_____

_____

_____

Committee in Charge

2007

Abstract

Estuaries are dynamic zones of mixing between freshwater and oceanic water. Because of these competing forces, estuaries are seasonal sources/sinks for suspended sediment, depending on the strength of the tidal and riverine forcing. The geomorphic evolution of an estuary is sensitive to the net erosion or deposition of sediment as well as localized patterns. The response of estuarine geomorphology to future scenarios of climate change and sediment supply is difficult to evaluate, and must be performed with a robust, calibrated model.

In this study I have modified, calibrated, and applied the public-domain Regional Ocean Modeling System (ROMS) to simulate tidal, annual, and decadal-timescale sediment transport processes in Suisun Bay, the landward-most subembayment of San Francisco Bay. The importance of calibrating to processes, as opposed to point suspended-sediment concentrations is stressed: the tidal-timescale movement of the estuarine turbidity maximum and annual-timescale sediment budget of Suisun Bay are used as calibration data for the first two calibration steps. The decadal-timescale calibration, performed using bathymetric change data, is aided by the development of the morphological hydrograph concept, where a limited number of flow hydrographs induce the same geomorphic change as the full set of hydrographs.

The final, calibrated model is applied to four future scenarios, which combine changes in sea level, streamflow timing and magnitude, and watershed sediment supply. The differences between scenarios, which are insensitive to parameter uncertainty, are

investigated, as opposed to absolute predictions. Sea-level rise resulted in a reduction in wave stress on the sediment bed, reducing sediment redistribution and promoting overall sediment deposition in the shallowest 2 m of Suisun Bay, while decreased watershed sediment supply decreased deposition through most of Suisun Bay. The moderate warming signal of 2030, reflected in altered streamflow timing and magnitude, had the most minor effect on overall geomorphic change. However, changes by the end of the 21st century may be sufficient to alter the sediment transport patterns within Suisun Bay. In all cases, the observed deposition was not sufficient to counteract the increase in sea level, which has major ramifications for intertidal and marsh areas of Suisun Bay.

Acknowledgments

I first recognize my advisor, collaborator, and mentor, Professor David Schoellhamer. With his guidance over the last six years, at the U.S. Geological Survey and U.C. Davis, I have become a researcher and a contributor to science. His encouragement and contributions to my studies have improved the quality of my methods and analyses. I also thank the members of my dissertation committee, Professors Bassam Younis and Paul Teller, for their support and enthusiasm towards my work. I enjoyed discussions with them immensely, and always looked forward to meeting with them. I also thank the other members of my qualifying exam committee, Professors Geoff Schladow and Robert Shumway, for their input.

Thanks, in no particular order, to Michael Dettinger, Lester McKee, Curt Battenfeld, Greg Brewster, Paul Buchanan, Jay Cuetara, Megan Lionberger, Heather Ramil, Greg Shellenbarger, Brad Sullivan, Randal Dinehart, Jon Burau, John Donovan, Pete Smith, Aaron Blake, Catherine Ruhl, Noah Knowles, Lisa Lucas, Jan Thompson, Bruce Jaffe, Dano Roelvink, Mick van der Wegen, Dan Cayan, Jim Cloern, and Nancy Monsen, for various kinds of assistance and advice with this study.

John Warner of the USGS Community Sediment Transport Model project provided indispensable assistance with model development and application. Without his help this study would not have been possible. The entire ROMS community is also acknowledged for their countless hours of modeling and troubleshooting that have made ROMS possible.

Because of the heavily computational nature of this study, many trips were made, at all hours, to “check the model”. On most of those occasions, I was accompanied by my best friend (and wife), Diana “gotta check the model” Ganju. Her patience on most visits was critical to my success.

Finally, I thank my mother and father. This work is dedicated to them.

Many portions of this work are taken from journal articles that I authored, under the auspices of the U.S. Geological Survey, and are therefore copyright-free.

Table of Contents

Abstract ii

Acknowledgments iv

Table of Contents vi

List of Figures xv

List of Tables xxiii

List of Symbols xxv

Chapter 1: Introduction 1

1.1 Description of estuaries 1

1.2 Relevance of estuarine geomorphology 2

1.3 Simulating estuarine geomorphology 4

1.4 Simulating estuarine geomorphology with regard to climate change and decreased watershed sediment supply 7

1.5 Research objectives 7

Chapter 2: Literature review 10

2.1 Estuarine geomorphic change 10

2.1.1 Classic estuarine geomorphology 10

2.1.2 Observations of estuarine geomorphic change 11

2.1.3 Modeling of estuarine geomorphic change 11

2.1.4 Limitations of prior modeling efforts 13

2.2 Climate change and sea-level rise 13

2.2.1 Global scale 13

2.2.2 California 14

2.3 Decreased watershed sediment supply 15

2.4 Climate change effects on estuarine geomorphology 16

2.4.1 Changes in freshwater flow 17

2.4.2 Changes in sea level 18

Chapter 3: Objective A: Development of a reliable modeling approach 20

3.1 Reliability of models 20

3.2 Path to reliability 21

3.3 Simulation and exploratory modeling 24

3.4 Calibration, validation, verification, and the multiple-timescale approach 26

3.5 Scenarios of change 29

3.6 Sources of uncertainty 30

Chapter 4: Model equations, solution procedures, and infrastructure 37

4.1 Hydrodynamics and tracers 37

4.2 Suspended-sediment transport and bed model 42

4.3 Solution schemes 44

4.4 Boundary conditions and external forcing 44

4.4.1 Landward flow and tracer concentrations 44

4.4.2 Seaward velocity, stage, and tracer concentrations 45

4.4.3 Wave-induced orbital velocities 45

4.5 Infrastructure 46

4.5.1 Platform and operating system 46

4.5.2 Pre- and post-processing 46

Chapter 5: Site description 48

5.1 California climate 48

5.2 Central valley and watershed 48

5.3 Sacramento and San Joaquin River Delta 50

5.4 Suisun Bay 52

Chapter 6: Objective B: Calibration and application to tidal-timescale processes 55

6.1 Introduction 55

6.2 Field observations 57

6.2.1 Methods 57

6.2.1.1 Continuous monitoring 57

6.2.1.2 Tidal-cycle monitoring 59

6.2.2 Results 60

6.2.2.1 Continuous monitoring 60

6.2.2.2 Tidal-cycle monitoring 63

6.3 Modeling simulations 65

6.3.1 Methods 66

6.3.1.1 Modeling domain 66

6.3.1.2 Boundary conditions 67

6.3.1.2.1 Landward boundary conditions: freshwater flow, salinity, SSC 67

6.3.1.2.2 Seaward boundary conditions: tidal flow, salinity, SSC..... 68

6.3.1.3 Calibration and validation..... 70

6.3.1.4 Center of mass calculation..... 70

6.3.2 Results..... 71

6.3.2.1 Calibration and validation..... 71

6.3.2.2 Center of mass calculation..... 73

6.4 Discussion..... 74

6.4.1 Laterally averaged conceptual models of ETMs 74

6.4.2 Simulation and comparison with conceptual models 75

6.5 Conclusions..... 78

Chapter 7: Objective C: Calibration and application to annual-timescale processes 80

7.1 Introduction..... 80

7.2 Field observations 85

7.2.1 Methods 85

7.2.1.1 Spring monitoring period..... 85

7.2.1.2 Tidal-cycle cross-sectional measurements..... 85

7.2.1.3 Total channel discharge 87

7.2.1.4 Residual suspended-sediment flux calculation 87

7.2.1.5 Annual sediment flux estimation 88

7.2.1.6 Yearly sediment budgets for Suisun Bay..... 89

7.2.2 Results..... 90

7.2.1.1 Spring monitoring period 90

7.2.2.2 Tidal-cycle cross-sectional measurements 91

7.2.2.3 Total channel discharge 94

7.2.2.4 Flux calculation 97

7.2.2.5 Annual sediment flux estimation 98

7.2.2.6 Yearly sediment budgets for Suisun Bay 102

7.3 Modeling simulations 103

7.3.1 Methods 103

7.3.1.1 Modeling domain 103

7.3.1.2 Idealization of boundary conditions 106

7.3.1.2.1 Landward boundary conditions: freshwater flow, salinity, SSC 106

7.3.1.2.2 Seaward boundary conditions: tidal flow, salinity, SSC 107

7.3.1.2.3 Sediment bed parameters 110

7.3.1.2.4 Atmospheric forcing 110

7.3.1.3 Selection of calibration/validation years and calibration/validation goals . 111

7.3.1.4 Sensitivity analysis 112

7.3.2 Results 113

7.3.2.1 Calibration and validation 113

7.3.2.2 Sensitivity analysis 115

7.4 Discussion 116

7.4.1 Annual sediment flux estimates 116

7.4.1.1 Accuracy of long-term prediction 116

7.4.1.2 Dispersive flux prediction 118

7.4.1.3 Seasonal pattern of erosion and deposition 119

7.4.1.4 Ramifications of sediment flux patterns 120

7.4.2 Model response to forcings 122

7.4.2.1 Watershed delivery 122

7.4.2.2 Wind-wave resuspension 124

7.4.2.3 Gravitational circulation 125

7.4.2.4 Landward sediment flux at Mallard Island 125

7.4.2.5 Model calibration and validation performance 127

7.5 Conclusions 127

Chapter 8: Objective D: Calibration and application to decadal-timescale processes.... 130

8.1 Introduction 130

8.2 Field observations 132

8.3 Modeling simulations 133

8.3.1 Methods 133

8.3.1.1 Modeling domain 133

8.3.1.2 Idealization of boundary conditions 134

8.3.1.2.1 Landward boundary conditions: freshwater flow, salinity, SSC 134

8.3.1.2.2 Seaward boundary conditions: tidal flow, salinity, SSC 135

8.3.1.2.3 Sediment bed parameters 136

8.3.1.2.4 Atmospheric forcing 137

8.3.1.3 Idealized time-stepping: morphological hydrograph and morphological factor 139

8.3.1.4 Selection of calibration goals 142

8.3.1.5 Sensitivity analysis 143

8.3.2 Results 144

8.3.2.1 Bathymetric change induced by composite results 144

8.3.2.2 Bathymetric change anomalies induced by each morphological hydrograph 146

8.3.2.3 Calibration performance 149

8.3.2.4 Sensitivity analysis 151

8.4 Discussion 152

8.4.1 Mechanism for bathymetric change patterns 152

8.4.2 Importance of parameterizing major forcings 154

8.4.3 Concept of morphological hydrograph 155

8.4.4 Morphological acceleration factor in non-stationary systems 158

8.4.5 Morphological acceleration, episodic forcing, and wetting and drying 158

8.4.6 Evaluating performance 159

8.5 Conclusions 160

Chapter 9: Objective E: Application of calibrated model to future scenarios 162

9.1 Introduction 162

9.2 Methods 164

9.2.1 Modeling domain 164

9.2.2 Implementation of landward and seaward boundary conditions 165

9.2.2.1 Scenario B: base-case 165

9.2.2.2 Scenario WS: warming and sea-level rise by 2030 166

9.2.2.3 Scenario DS: decreased sediment supply and sea-level rise by 2030..... 168

9.2.2.4 Scenario WDS: warming, decreased sediment supply, and sea-level rise by 2030..... 168

9.2.3 Sensitivity analysis 169

9.3 Results..... 170

9.3.1 Specific and bulk changes in sedimentation 170

9.3.1.1 Scenario B: differences between morphological hydrographs 170

9.3.1.2 Scenario WS: effect of warming and sea-level rise 172

9.3.1.3 Scenario DS: effect of decreased sediment supply and sea-level rise 173

9.3.1.4 Scenario WDS: effect of warming, decreased sediment supply, and sea-level rise..... 174

9.3.2 Sensitivity analysis 176

9.4 Discussion..... 177

9.4.1 Comparison of dry and wet year bathymetric change 177

9.4.2 Effect of sea-level rise: scenario B vs. scenario WS 178

9.4.3 Effect of warming: scenario DS vs. scenario WDS..... 179

9.4.4 Effect of decreased sediment loads: scenario WS vs. scenario WDS 180

9.4.5 Changes in optical depth..... 181

9.5 Conclusions..... 184

Chapter 10: Conclusions..... 187

10.1 Satisfaction of research objectives..... 187

10.1.1 Objective A: Development of a reliable modeling approach 187

10.1.2 Objective B: Calibration and application to tidal-timescale processes..... 187

10.1.3 Objective C: Calibration and application to annual-timescale processes..... 188

10.1.4 Objective D: Calibration and application to decadal-timescale processes 188

10.1.5 Objective E: Application of calibrated model to future scenarios..... 189

10.2 Summary 190

10.3 Recommendations for future work 191

10.3.1 Study-specific recommendations..... 191

10.3.2 General recommendations 193

References..... 196

List of Figures

Figure 1.1 San Francisco Bay, and subembayments South Bay, Central Bay, San Pablo Bay, and Suisun Bay. Suisun Bay is the landward-most subembayment, adjacent to the Sacramento and San Joaquin River Delta 5

Figure 1.2 Suisun Bay and the locations of sediment flux data (McKee et al., 2006; Ganju and Schoellhamer, 2006) 6

Figure 1.3 Bathymetric change maps of Cappiella et al. (1999). Increased deposition between 1867-1887 resulted from seaward transport of hydraulic mining debris..... 6

Figure 5.1 California, Central Valley (bounded by dashed line), Sierra Nevada, and major rivers 49

Figure 5.2 Reservoir capacity in California. Increasing capacity signals increasing management of the hydrologic system 50

Figure 5.3 Land-water terrain map of San Francisco Bay and the Sacramento/San Joaquin Delta. State and federal programs export water from the southern Delta..... 51

Figure 6.1 Suisun Bay, and locations of measurement sites..... 58

Figure 6.2 Cross-section of Carquinez Strait at I-680 Bridge. Four optical sensors were situated within the cross-section; upper and lower water column at site NBen (NU and NL respectively) and upper and lower water column at site SBen (SU and SL respectively). Square indicates example of ETM center of mass, with x and y coordinate origins defined as shown. Depth is referenced to mean lower low water… 59

Figure 6.3 Time-series of SSC from four optical sensors at cross-section in Carquinez Strait: upper sensor at site NBen; lower sensor at site SBen; upper sensor at site SBen; and lower sensor at site SBen..... 61

Figure 6.4 Time-series of mean velocity in Carquinez Strait and SSC from lower sensors at sites NBen (solid) and SBen (dashed). SSC at SBen is typically maximum at the start of flood, while SSC at NBen is maximized at the end of ebb..... 62

Figure 6.5 Time-series of U_{rms} (measure of tidal energy) and tidally averaged stratification in Carquinez Strait; x-displacement of the ETM center of mass; and y-displacement of the ETM center of mass. Center of mass favors the north side and lower water column on neap tides during periods of reduced tidal energy, and migrates toward the south side and upper water column on spring tides during periods of increased tidal energy 63

Figure 6.6 Movement of ETM center of mass between slack before ebb to max flood, obtained by water column profiling of SSC in the transect seaward of the I-680 Bridge. Center of mass begins at circle marked 1 at slack before ebb, migrates to 3 at maximum ebb, 5 at slack after ebb, and 7 at maximum flood tide. Depth is referenced to mean lower low water..... 64

Figure 6.7 Computational grid of Suisun Bay, in ROMS orthogonal, curvilinear format. Depth is referenced to mean lower low water. Masked land cells are not shown 67

Figure 6.8 Model calibration to stage at Martinez and Mallard Island. The two sites represent the western (Martinez) and eastern (Mallard Island) ends of Suisun Bay. Stage is referenced to mean lower low water 72

Figure 6.9 Model validation to vertical salinity stratification at site NBen and longitudinal salinity gradient between site NBen and Mallard Island..... 72

Figure 6.10 Model results of U_{rms} and tidally averaged stratification; x-displacement of the ETM center of mass; and y-displacement of the ETM center of mass. In agreement with field observations, center of mass favors the north side and lower water column on neap tides during periods of reduced tidal energy, and the south side and upper water column on spring tides during periods of increased tidal energy..... 74

Figure 6.11 Model surface plot of strength of gravitational circulation on neap tide and change in strength from spring tide to neap tide. Increasingly negative values indicate larger negative product of surface and bottom velocities, and therefore stronger gravitational circulation 76

Figure 6.12 Modeled cross-channel and vertical velocity vectors on spring tide and neap tide. Lateral and vertical circulation are enhanced on spring tide, with near-bed velocities on the north side directed southward. Depth is referenced to mean lower low water..... 77

Figure 7.1 Suspended-sediment concentration (SSC) time-series from sites upper sensor at site NBen; lower sensor at site NBen; upper sensor at site SBen; and lower sensor at site SBen. Note higher data return from lower sensors. SSC was typically higher at lower sensors..... 90

Figure 7.2 Interpolated profiles of suspended-sediment concentration. Early ebb profile shows higher concentrations in the ebb-dominant north channel, while SSC is

maximized in the south channel at the beginning of flood. Maximum SSC in each profile is 320 and 1000 mg/L, respectively 91

Figure 7.3 Calibration of site NBen and SBen SSC to velocity-weighted SSC (SSC_u); index velocity to channel-average velocity (U); and stage to cross-sectional area (A). Tidal-cycle measurements were used to obtain relationships that can be extended over spring monitoring period, yielding advective ([U][A][SSC_u]), dispersive (U'[A][SSC_u']), and Stokes drift ($U'A'$ [SSC_u]) fluxes over the spring monitoring period 93

Figure 7.4 Instantaneous and tidally averaged discharge in Carquinez Strait (shifted, see Fig. 7.5), Q and [Q], respectively; velocity-weighted suspended-sediment concentration, SSC_u; and total, advective, dispersive, and Stokes drift flux components. Positive values indicate seaward (ebb) transport, negative values indicate landward (flood) transport..... 94

Figure 7.5 Cumulative water discharge calculated from Delta measurement sites (QWEST), Dayflow, discharge measured in Carquinez Strait ($Q_{original}$), and $Q_{original}$ with 1 cm/s ebb-directed shift ($Q_{shifted}$) 96

Figure 7.6 Linear regression of QWEST and lower SSC at site NBen (BenSSC) product to advective flux; multiple linear regression of RMS value of lower SSC at site NBen ($BenSSC_{rms}$), QWEST, and longitudinal salinity gradient (LSG) versus dispersive flux; and lower SSC at site NBen (BenSSC) to Stokes drift flux 99

Figure 7.7 Spring monitoring period measured and predicted fluxes; total flux (sum of advective, Stokes drift, and dispersive flux); advective flux; dispersive flux; and

Stokes drift flux. Positive values indicate seaward (ebb) transport, negative values indicate landward (flood) transport 100

Figure 7.8 Computational grid of Suisun Bay, in ROMS orthogonal, curvilinear format. Depth is referenced to mean lower low water 105

Figure 7.9 Formulation of idealized seaward SSC boundary condition for three water years, as the sum of a wind, spring-neap, and flow signal, plus a noise component (not shown) 109

Figure 7.10 Time-series of sediment fluxes at Mallard Island, I-680 Bridge, and the net budget for Suisun Bay. Dashed lines indicate model results, solid line are estimates of McKee et al. (2006) and Ganju and Schoellhamer (2006) 114

Figure 7.11 Net observed and modeled sediment budgets for five water years. Poor agreement in 1998 is due to error in the extrapolation of dry season relations (see Section 7.4.2.1) 115

Figure 7.12 Residual error generated by extrapolating dry period empirical relationships of Ganju and Schoellhamer (2006) to wetter periods 124

Figure 7.13 Model results for net sediment flux at the Mallard Island cross-section for water year 2002 126

Figure 8.1 Bathymetric change maps of Cappiella et al. (1999). Increased deposition between 1867-1887 resulted from seaward transport of hydraulic mining debris.... 132

Figure 8.2 Model domain for hindcasting simulations. Configuration of 1867 has greater extent of shallows and islands, and generally wider channels 134

Figure 8.3 Three synthetic signals used to generate wind speed time-series for hindcasting simulations. Final time-series is clipped so as to contain no values less than zero 138

Figure 8.4 Final synthetic signal compared with measured wind from 1998. Episodic winter storm winds (notably December) in the measured record are ignored in the synthetic record 139

Figure 8.5 Freshwater flows and sediment loads for the three morphological hydrographs (MH) 141

Figure 8.6 Depth ranges in Suisun Bay, referenced to MLLW. Darker areas indicate areas of specified depth range. 143

Figure 8.7 Profile of observed, composite, and individual morphological hydrograph depth changes 145

Figure 8.8 Observed and modeled bathymetric change for 1867-1887 period. Modeled change is the composite results obtained with three morphological hydrographs. Observed change results were interpolated on to the numerical grid used for this study; actual data density is substantially higher (Fig. 8.1). Locations Sh, Int, and Ch used in Fig. 8.11; cross-section AB used in Fig. 8.13 146

Figure 8.9 Bathymetric change anomalies for each morphological hydrograph, obtained by differencing individual and mean results. Positive values indicate deposition relative to the mean result, negative values indicate erosion relative to the mean result 148

Figure 8.10 Profile of simulated bathymetric changes for three morphological acceleration factors (MF) 152

Figure 8.11 Freshwater inflow (MH 1), wind speed, and tidally averaged bathymetric changes (in 15 min intervals) for three depth regimes of Suisun Bay (marked in Fig. 8.8): channel (Ch, landward end of main channel), intermediate (Int, mouth of Grizzly Bay), and shoal (Sh, head of Grizzly Bay) 154

Figure 8.12 Bathymetric change anomalies of MH 1 and MH 2, as compared to MH 3 …..... 157

Figure 8.13 Bathymetric change of a cross-section of the Reserve Fleet Channel (Fig. 8.8), for three morphological hydrographs 157

Figure 9.1 Hydrographs and sediment loads for base-case and 2030 conditions, for three morphological hydrographs (1999, 2001, 2006)..... 167

Figure 9.2 Bathymetric changes, by depth interval, induced by the morphological hydrographs for scenario B, and the composite result..... 171

Figure 9.3 Composite bathymetric change result, and anomalies (as compared to composite) of the three morphological hydrographs 172

Figure 9.4 Anomalies, relative to the base-case simulation, of bed level change for three scenarios. Positive values indicate increased sediment mass on the bed for the scenario, relative to the base case 175

Figure 9.5 Anomaly of bed level changes, by depth interval, between the base scenario and the three future scenarios. Results are the composite of three morphological hydrographs for each scenario 176

Figure 9.6 Anomaly between scenarios DS and WDS (showing the effect of warming and altered hydrograph) and anomaly between scenarios WS and WDS (showing the

effect of decreased watershed sediment supply). Negative values indicate decreased sediment mass on the bed for the WDS scenario relative to the DS and WS scenarios, respectively 180

List of Tables

Table 3.1 Multi-step calibration procedure for three process timescales. Sediment properties include bed shear strength and settling velocity 29

Table 6.1 Model parameters and values for tidal-timescale simulations. Values with an asterisk were used as calibration parameters 66

Table 7.1 Water year, cumulative flow, sediment flux at Mallard Island, sediment flux at Carquinez Strait, net sediment budget, and advective, dispersive, and Stokes drift flux components. Positive values indicate seaward transport 103

Table 7.2 Modeling parameters for annual-timescale simulations. Values with an asterisk were varied as calibration parameters. Sediment parameters are given for two sediment classes 104

Table 7.3 Annual-timescale modeling performance in regards to four goals..... 113

Table 7.4 Sensitivity analysis results; positive fluxes indicate seaward fluxes, negative values are landward fluxes..... 116

Table 8.1 Model parameters for decadal-timescale simulations. Values marked with an asterisk were varied for calibration..... 133

Table 8.2 Observed bathymetric change and modeled bathymetric change for three morphological hydrographs (MH), in depth intervals of 2 m. Mean error, in bold, is the sum of the weighted errors as a percentage of depth 145

Table 8.3 Decomposition of Brier Skill Score by depth interval, with proposed BSS classification of Sutherland et al. (2004) 150

Table 8.4 Bathymetric changes in depth intervals for three morphological acceleration factors (MF). Positive percent changes indicate more bathymetric change relative to the MF=20 case, negative percent changes less bathymetric change relative to the MF=20 case..... 151

Table 8.5 Flow, sediment load, and bed change characteristics of three morphological hydrographs..... 153

Table 9.1 Model parameters for future scenario simulations 165

Table 9.2 Total and peak flow and sediment load characteristics of morphological hydrographs and represented period (1990-2006). 166

Table 9.3 Bed level (BL) and relative water depth (RWD) changes for all scenarios. Positive BL values indicate deposition, positive RWD values indicate deepening, with sea-level rise included..... 171

Table 9.4 Sensitivity analysis results, comparing non-perturbed and perturbed simulations (scenario B and WDS), with wave period perturbed by a 10% decrease 177

Table 9.5 Percent area of Suisun Bay and western Delta characterized by optical depth ranges. 183

List of Symbols

Symbol	Description	Dimensions
A	channel area	m^2
B	production of turbulent kinetic energy by buoyancy	$m^2\ s^{-3}$
BSS	Brier Skill Score	--
C	tracer concentration	^oC, salinity, or kg m^{-3}
C_{sink}	tracer sink term	C units * m s^{-1}
C_{source}	tracer source term	C units * m s^{-1}
D	total water depth	m
F	total sediment flux	kg s^{-1}
H	grid cell thickness	m
K_c	scalar eddy diffusivity	$m^2\ s^{-1}$
K	momentum eddy viscosity	$m^2\ s^{-1}$
MF	morphological acceleration factor	--
MH	morphological hydrograph	--
OD	optical depth	--
P	production of turbulent kinetic energy by shear	$m^2\ s^{-3}$
Q	freshwater flow	$m^3\ s^{-1}$
Q_s	riverine sediment load	Mt (million metric tons)
S_0	boundary salinity	--
S	salinity	--
SSC	suspended sediment concentration	mg L^{-1}
SSC_{CAR}	SSC at Carquinez Bridge	mg L^{-1}
SSC_{comb}	combined SSC signal	mg L^{-1}
SSC_f	flow SSC signal	mg L^{-1}
SSC_{sn}	spring-neap SSC signal	mg L^{-1}
SSC_u	velocity-weighted SSC	mg L^{-1}

SSC_w	Wind SSC signal	mg L^{-1}
U	channel-average velocity	m s^{-1}
U_d	daily wind speed signal	m s^{-1}
U_f	final wind speed signal	m s^{-1}
U_s	seasonal wind speed signal	m s^{-1}
U_w	weekly wind speed signal	m s^{-1}
X	longitudinal estuary coordinate	km
$a_{1,2,3}$	synthetic SSC coefficients	--
a_{ssc}	light attenuation coefficient constant	L mg^{-1} m^{-1}
a_w	synthetic wind speed coefficient	--
b_w	synthetic wind speed coefficient	--
c	stability coefficient	--
c_w	synthetic wind speed coefficient	--
$c_{\varepsilon 1,2,3}$	turbulence closure coefficients	--
f	Coriolis parameter	s^{-1}
g	gravity	m s^{-2}
Δh	bathymetric change	m
k	turbulent kinetic energy	m^2 s^{-2}
k_p	phytoplankton component of light attenuation coefficient	m^{-1}
k_{ssc}	suspended-sediment component of light attenuation coefficient	m^{-1}
k_t	light attenuation coefficient	m^{-1}
l	generic length scale	m
n	sediment bed porosity	--
p	pressure	N m^{-2}
r	correlation coefficient	--
s	vertical sigma coordinate	--
t	time	s
u	velocity x-direction	m s^{-1}

u'	turbulent velocity x-direction	m s^{-1}
$\bar{u}$	depth-integrated velocity x-direction	m s^{-1}
u_s	surface velocity	m s^{-1}
u_b	bottom velocity	m s^{-1}
v	velocity y-direction	m s^{-1}
v'	turbulent velocity y-direction	m s^{-1}
$\bar{v}$	depth-integrated velocity y-direction	m s^{-1}
w'	turbulent velocity s-direction	m s^{-1}
w_s	sediment settling velocity	m s^{-1}
x	horizontal direction	m
y	horizontal direction	m
z	vertical elevation	m
z_0	total bottom roughness length	m
α	salinity gradient parameter, Brier Skill Score parameter	--
β	salinity gradient parameter, Brier Skill Score parameter	--
ε	dissipation rate	m^2 s^{-3}
ε_s	erosion rate constant	kg m^{-2} s^{-1}
γ	Brier Skill Score parameter	--
η	wave averaged free surface elevation	m
ρ	density	kg m^{-3}
ρ_0	reference density	kg m^{-3}
ν	kinematic viscosity	m^2 s^{-1}
ν_c	tracer kinematic diffusivity	m^2 s^{-1}
ξ	parameter space	--
ξ'	perturbed parameter space	--
σ_ε	Schmidt number for the eddy diffusivity of dissipation	--

σ_k	Schmidt number for the eddy diffusivity of turbulent kinetic energy	--
τ_c	bottom critical erosion stress	N m^{-2}
τ_w	bottom stress	N m^{-2}
ψ	transported quantity for turbulence model	--

1 Introduction

1.1 Description of estuaries

Estuaries are dynamic zones of mixing between freshwater and oceanic water, typically harboring diverse flora and fauna such as juvenile fish (Blaber and Blaber, 1980), seagrass beds (Orth et al., 1984), and mangroves (Lugo and Snedaker, 1974). Several of the United States' largest population centers are located adjacent to estuaries, such as New York (Hudson Estuary), Washington D.C. (Chesapeake Bay), Miami (Biscayne Bay), and San Francisco (San Francisco Bay). Settlements traditionally sprouted near estuaries due to waterborne commerce, fisheries, and local arable land. In modern times, estuaries warrant attention for a myriad of reasons, including harborage for vessel traffic, biological diversity, systemic contamination problems, and sensitivity to managed freshwater flows.

Located at the interface between riverine and oceanic forces, estuaries are subjected to hydrodynamic forcing from both the landward and seaward ends. Tidal forcing, from the seaward boundary, causes oscillating currents and periods of slack water, while episodic freshwater flows alter residual currents in the landward and seaward directions. Wind is an additional physical force applied to the water surface and capable of generating wind waves. These competing forces and sedimentary properties determine sediment erosion, transport, and deposition. The geomorphic evolution of an estuary, i.e. the progression of estuary depth and shape, is sensitive to the net erosion or deposition of sediment as well as localized patterns. As geomorphology evolves, there is a feedback to the hydrodynamics, as the system attempts to reach a quasi-equilibrium. For example,

deposition on a shoal decreases water depth, which increases bottom shear stress from wind waves, which in turn decreases deposition.

1.2 Relevance of estuarine geomorphology

Concerns about estuarine geomorphology originally arose from commercial and military interests related to ports and harbors. The need to maintain adequate depths for vessels led to bathymetric surveys in coastal and estuarine areas, which are essentially studies in sedimentation. Shipping channels, ports, and harbors may be low-energy areas, and can encourage sediment to deposit, thereby reducing depth and impeding navigation. Channels are then typically dredged deeper than this quasi-equilibrium state, and deposition is inevitable in most cases. Predicting the rate of deposition assists in planning dredge operations, which are time and cost-intensive. In the current era, dredging is still a necessity in most channels, ports, and harbors.

In many estuaries, alteration of the landscape for commercial and agricultural interests has reduced the area of natural tidal marshes. Tidal marshes are low-energy, depositional areas where vegetation is able to emerge and colonize the marsh plain (Leonard, 1997; Cahoon et al., 1996). They are common in estuaries due to the presence of fine sediments and regular tidal inundation. While a portion of marsh deposition is from local detritus sources, fine sediment from the watershed may be necessary to maintain marsh elevation as sea level rises (Bartholdy et al., 2004; Temmerman et al., 2004). Furthermore, the patterns of estuarine geomorphology, such as the presence of adjacent mudflats, will determine whether sediment will be available to fringing marshes. Recent interest in tidal

marsh survival springs from their role in the ecological framework as habitat for valued flora and fauna. Several sensitive species of vegetation, birds, and mammals require specific types of tidal marshes to remain viable. Due to the biological value of these systems, many regulatory agencies seek to restore lost tidal marshes and protect existing areas from drainage or development. Success of tidal marsh restoration is partially dependent on the availability of fine sediment and geomorphic evolution.

Estuaries trap sediment from the watershed, where anthropogenic activities have traditionally produced contaminants that reach rivers. Agricultural runoff, with elevated nutrient and pesticide concentrations, is a major source of estuarine contamination (Bergamaschi et al., 2001). Mining debris, rich in heavy metals, may also reach estuaries and contaminate bed sediments (Hornberger et al., 1999). In addition, civilizations have tended to develop near estuaries, and direct input of contaminants to estuaries is common. Hydrophobic contaminants are stored in the bed sediments because they tend to adsorb to the sediment particle surfaces, rather than remain in a dissolved state. While permanent contaminant storage in the bed sediments may seem inconsequential, food web dynamics may introduce the contaminants to species further up the chain, eventually reaching humans (Linville et al., 2002). As an estuary becomes erosional or depositional, the availability of contaminants in the water column may also change substantially due to gradients in bed contaminant concentration (Hornberger et al., 1999).

1.3 Simulating estuarine geomorphology

Conceptually, simulating geomorphic evolution of an estuary is as straightforward as modeling hydrodynamics and sediment transport. However, small errors in a model calibrated to tidal-timescale data can accumulate over decadal timescales to give unrealistic results for geomorphic evolution (Schoellhamer et al., in press). The solution to this problem is a robust calibration method, which involves calibrating to data of different timescales. For example, one can calibrate to tidal-timescale suspended-sediment dynamics, annual-timescale sediment fluxes, and decadal-scale bathymetric change in three distinct steps. These give confidence in both the formulation of the model and the application of the model by the modeler. Unfortunately, most estuaries do not have sufficient data for calibration, due to the difficulty and expense of data collection. Therefore these steps have not been taken in prior efforts, due to limited data and computational ability.

Suisun Bay, California (Figs. 1.1, 1.2), provides a unique opportunity for implementing a robust calibration procedure, because of the relative wealth of observational data. Hydraulic mining in the 19th century released large quantities of sediment, causing major perturbations to the geomorphology of the bay. These perturbations are quantified in the data of Cappiella et al. (1999), which represent five bathymetric surveys in 1867, 1877, 1922, 1942, and 1990 (Fig. 1.3). These data are ideal for calibrating a geomorphic model to bathymetric change. Intensive modern data collection efforts have produced temporally dense datasets of tidal-timescale currents, salinity, and suspended-sediment concentrations (this study; Ganju and Schoellhamer, in press(a); Ganju and

Schoellhamer, 2006; Ruhl and Schoellhamer, 2004; Schoellhamer, 2001; Warner et al., 2004). Lastly, further studies have used these data to produce annual sediment load estimates at the landward and seaward boundaries of Suisun Bay (McKee et al., 2006; this study; Ganju and Schoellhamer, 2006). With these three types of data available, a robust calibration will make modeling future geomorphic change possible. As climate change and anthropogenic actions in the watershed alter hydrology, these modeling techniques can be applied to future scenarios of geomorphic change, under altered hydrologic conditions.

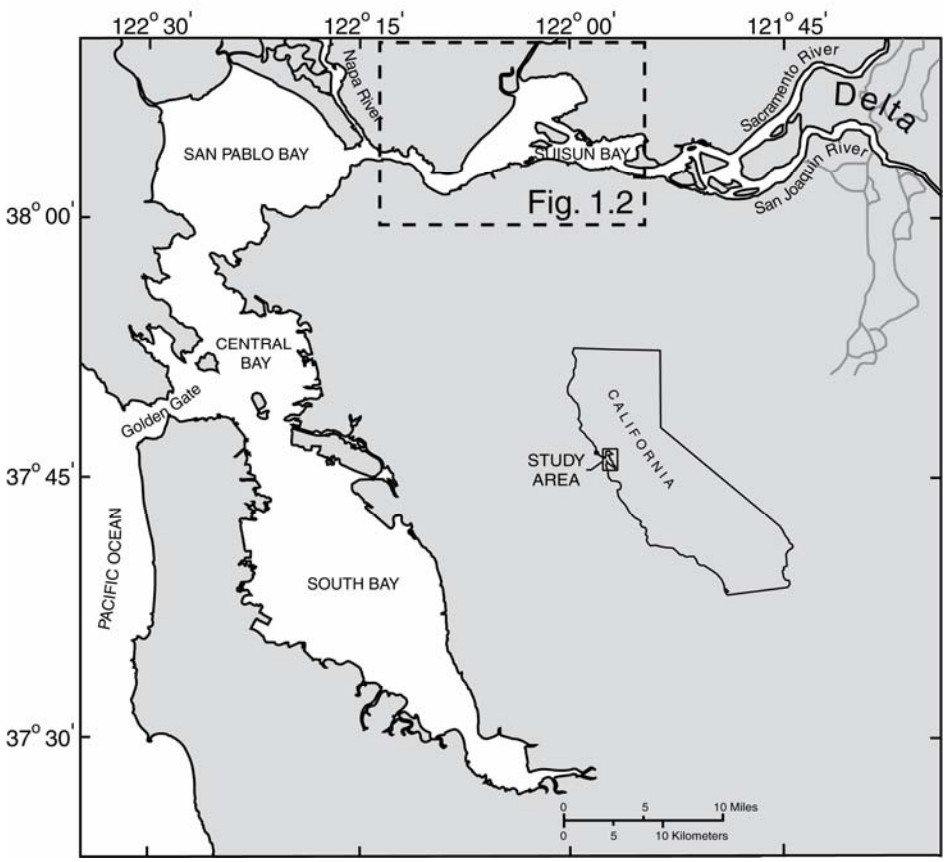

Figure 1.1 San Francisco Bay, and subembayments South Bay, Central Bay, San Pablo Bay, and Suisun Bay. Suisun Bay is the landward-most subembayment, adjacent to the Sacramento and San Joaquin River Delta.

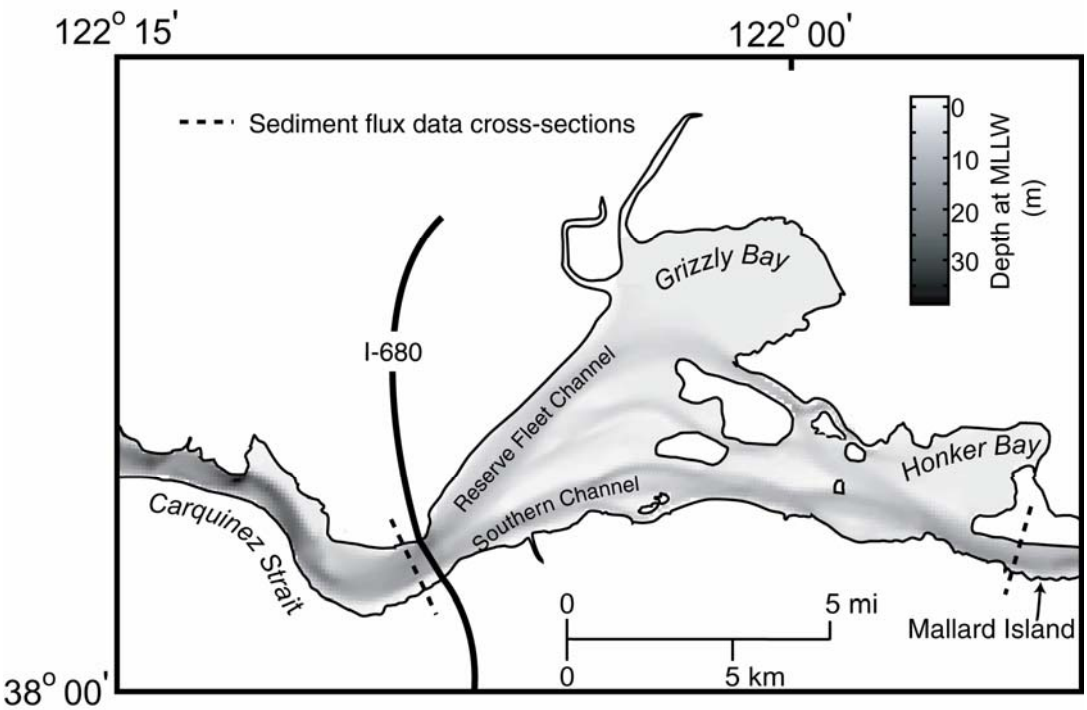

Figure 1.2 Suisun Bay and the locations of sediment flux data (McKee et al., 2006; Ganju and Schoellhamer, 2006).

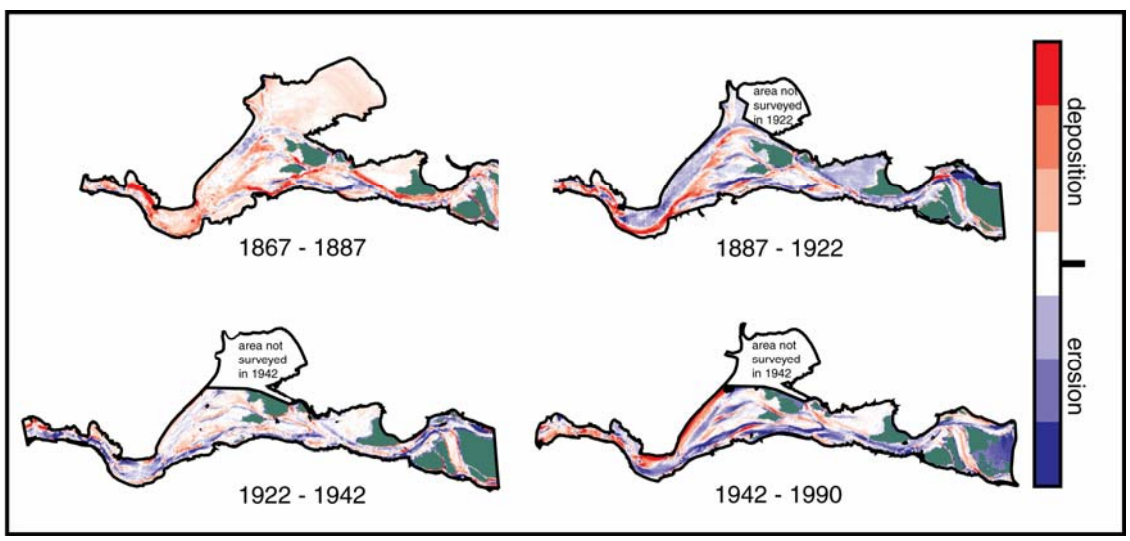

Figure 1.3 Bathymetric change maps of Cappiella et al. (1999). Increased deposition between 1867-1887 resulted from seaward transport of hydraulic mining debris.

1.4 Simulating estuarine geomorphology with regard to climate change and decreased watershed sediment supply

The response of estuarine geomorphology to future scenarios of climate change and decreasing sediment supply is unknown. Future climatic changes, specifically precipitation and air temperature, will alter the timing and magnitude of freshwater flows (Knowles and Cayan, 2002), and therefore sediment supply to estuaries. Accelerated sea-level rise (Meehl et al., 2007) will increase depth, salinity intrusion, and inundation of intertidal areas, thereby modulating the hydrodynamics and sediment transport in those areas. Worldwide, human activity in many watersheds has reduced sediment supply to estuaries and coastal seas, due to trapping behind dams and soil conservation measures (Walling, 2006). How these changes will effect geomorphic evolution (and therefore navigation, tidal wetlands, contaminant fate and transport) can be evaluated using a robust numerical model of hydrodynamics and sediment transport. Evaluating changes in geomorphology in response to future scenarios can be done by differencing the results of a base-case scenario simulation and a future scenario simulation. Therefore the goal is not a concrete prediction of future conditions, but a possible scenario of the change in conditions, under a prescribed future climate.

1.5 Research objectives

To date, a robust calibration of an estuarine model, at differing timescales, has not been performed. Modeling decadal-timescale estuarine processes, such as geomorphic change, is in the early stages of development. I intend to perform a robust calibration at several timescales of interest, due to the wealth of available calibration data. I then intend to

develop innovative techniques for decadal-timescale simulations of estuarine geomorphic change, using concepts developed by myself and others. The final framework will provide a guide for any modeling endeavor that addresses processes on varying timescales.

The specific objectives of this dissertation are:

a) Develop a reliable, physically based modeling approach that provides the greatest confidence in model output;

b) Modify, apply, and calibrate the model to tidal processes in Suisun Bay: tidal stage, salinity dynamics, and lateral movement of the estuarine turbidity maximum during the spring of 2004;

c) Modify, apply, and calibrate the model to annual processes in Suisun Bay: suspended-sediment fluxes at two cross-sections (landward and seaward boundaries), and ultimately the net sediment budget of Suisun Bay on the annual timescale during 1997-1998, and 2002-2004;

d) Modify, apply, and calibrate the model to decadal processes in Suisun Bay: historical bathymetric change, distributions of depth, and evolution of subtidal habitat from 1867-1887; this step will define how I apply a three-dimensional tidal-timescale model to simulate geomorphic change;

e) Apply the model to base-case and future scenarios of geomorphic change, and evaluate model sensitivity, changes in net sediment supply, optical depth, and habitat distribution for a 20 year future period.

2 Literature review

2.1 Estuarine geomorphic change

2.1.1 Classic estuarine geomorphology

At a basic geologic level, estuarine geomorphology is determined by the initial mode of formation. Four major geologic classifications of estuaries are coastal plain, tectonic, bar-built, and fjord-type estuaries (Pritchard, 1967). Coastal plain estuaries are formed through the drowning of post-Ice Age river valleys, as sea level rose and river valleys were flooded. In general, these estuaries have mild sloping bottoms; many estuaries on the east coast of North America are of this type (e.g. Chesapeake Bay; Narragansett Bay). Tectonic estuaries are formed through folding or faulting in the earth surface crust, which causes subsidence relative to sea level. The sea subsequently fills the void, creating an estuary. Many estuaries on the tectonically active Pacific coast have these features, such as San Francisco Bay, and the Nicoya Estuary in Costa Rica (Vargas, 1995). Bar-built estuaries are characterized by seaward bar features, that create an estuarine lagoon behind the bar. These estuaries may become closed seasonally, as coastal processes transport sand in both the cross-shore and along-shore direction. Many estuaries on the southeastern Atlantic coast of the United States fall under this classification (Dame et al., 2000). Fjord-type estuaries are characterized by deep, narrow geometry, caused by the scouring action of receding glaciers. Many areas once covered by glaciers (e.g. Chile, New Zealand, Norway) have several fjord-type estuaries. These initial formation modes determine the linkage between watershed and ocean, and the resulting hydrodynamic and sediment transport patterns modulate the relatively short-term (centuries) configuration.

2.1.2 Observations of estuarine geomorphic change

Geomorphic evolution of estuarine habitats and landscapes over decadal timescales (>10 y) is sensitive to sediment supply from the watershed, seaward embayments, and the bed, as well as estuarine hydrodynamics and anthropogenic activities. Van der Wal et al. (2002) analyzed bathymetric data for the Ribble Estuary, demonstrating the effects of human manipulation of channels and banks on sediment deposition. Reduced tidal prism, and ultimately reduced velocities, led to increased sedimentation in this case. Burningham and French (2006) consider the morphology of a mixed sand-gravel delta at the mouth of the Deben Estuary, and link long-term shoreline recession to changes in sea-level, while the steepening of the nearshore resulted from subsequent armoring of the coast. In the Mersey Estuary, bathymetric change over the 20th century was deemed largely a function of anthropogenic activities in Liverpool Bay, the seaward embayment (Thomas et al., 2002). Construction of a training wall in Liverpool Bay and dredging in seaward channels caused sedimentation that reduced estuary volume by 10%. The subembayments of San Francisco Bay filled rapidly during the hydraulic mining period (Cappiella et al., 1999; Jaffe et al., 1998), and have been erosional as the mining pulse has reduced. It is clear from these studies that changes in configuration alter hydrodynamic patterns, and therefore sedimentation patterns. Dramatic changes in sediment supply (e.g. hydraulic mining) can cause perturbations that last for decades.

2.1.3 Modeling of estuarine geomorphic change

Modeling estuarine geomorphic change over decadal timescales is hampered by a relative lack of data regarding boundary conditions, initial bathymetric configuration, and

temporally varying forcings. Computational expense is also a major difficulty, as a spatially and temporally detailed model requires significant resources in terms of computing power, and model development. Early discussion of morphological modeling (e.g. de Vriend et al., 1993, Latteux, 1995) highlighted the need for input reduction and idealization, not only for computational efficiency, but for robustness of the simulation. Representative sets of forcing data must be selected because measured data (e.g. tides, winds, freshwater flows) are unavailable in the future and limited in the past. As an example, both de Vriend (1993) and Latteux (1995) discuss the selection of a limited set of wave climates. Analysis of wave data will suggest the dominant wave climate, in terms of height, direction, and period. Then a suitable set of frequently occurring climates, weighted by frequency of occurrence, can be used as input to the geomorphic model.

Several idealized case studies have emerged in recent years, using the concepts of input reduction, representative forcings, and idealization. Hibma et al. (2003) model the evolution of an idealized estuary over 100 y, recreating patterns of channel-shoal interaction, while Roelvink (2006) focused on the implementation of the bed-updating routines and their effect on the evolution of an idealized tidal inlet. Lesser et al. (2004) review the development, validation, and testing of a three-dimensional geomorphic model, including a comparison of model performance with bathymetric data near a modified harbor. These studies use the concept of the morphological scaling factor, whereby the bathymetric change over a short timescale is accelerated linearly. This allows the bathymetry to evolve relatively quickly; feedback between the bathymetry and currents is still allowed, though the response is accelerated.

2.1.4 Limitations of prior modeling efforts

Most geomorphic modeling efforts in estuaries are lacking calibration data over decadal timescales. To date, there has not been an attempt to calibrate a tidal-timescale hydrodynamic/sediment transport model to decadal-scale bathymetric change. Evaluating future scenarios of change can only be done if calibration to the proper type of data is performed. Prior efforts have relied on calibration to modern data such as tidal stage, salinity, or suspended-sediment concentration (SSC), and then extrapolation of the results over annual timescales (e.g. Lumborg and Pejrup, 2005). While these data may be appropriate for tidal-timescale analyses, decadal scale modeling is subject to large errors due to incorrect parameter specification (Schoellhamer et al., in press). Spin-up errors, where the bathymetry adjusts to the incorrect parameters, can be a major source of uncertainty. The efforts of Hibma (2003), Lesser et al. (2004), and Roelvink (2006), while laying the groundwork for the bed-updating procedures and schemes, have not performed a quantitative comparison with actual bathymetric change data, as I will attempt here.

2.2 Climate change and sea-level rise

2.2.1 Global scale

Climatic changes over millennia have been observed in field data ranging from ice cores (e.g. Barnola et al., 1997) to pollen signatures (Haberle and Maslin, 1999). Recent anthropogenic climate change is very likely, as observations of ecological communities, glaciers, atmospheric patterns, and ocean circulation have made clear (IPCC, 2007). The trapping of heat by greenhouse gases (e.g. methane, carbon dioxide) is thought to be

responsible for the pronounced warming trend present in the last century. Computational ability in the last few decades has enabled atmospheric modelers to perform decadal-scale projections of future climate with global climate models (GCMs), under several scenarios of greenhouse-gas emissions (e.g. Washington et al., 2000; Hulme et al., 1999; Roeckner et al., 1999). These simulations are at coarse resolutions that must be downscaled or used as input to finer resolution models, in order to examine climate effects over smaller areas.

Sea-level change throughout the oceans is a cyclical process, due to thermal expansion of the oceans and the melting of polar icecaps caused by warming of the atmosphere (Revelle, 1990). Recent accelerated warming may cause a drastic increase in ocean temperatures (and therefore expansion), while melting and fragmenting of polar ice will increase the volume of ocean water (Meehl et al., 2007). Sea level rise estimates indicate a possible increase in sea level of about 0.58 m by 2100, which is a faster rate than previously observed (Meehl et al., 2007). These increases in sea level will propagate into estuarine environments, altering the water level, hydrodynamics, and salinity.

2.2.2 California

GCMs are usually run at a spatial resolution of hundreds of kilometers, and nested models can improve resolution. Regional climate modelers use GCM output to drive regional climate models over California, that are downscaled to a finer resolution (e.g. Wilby and Dettinger, 2000). A further downscaling step improves resolution to 4 km, which is needed for coupled snowpack/watershed models of California. Because most of California's water is derived from snowmelt (stored in reservoirs), the condition of

snowpack (i.e. thickness, water content) is critical for the state's water supply. Knowles and Cayan (2002) have shown that future warming scenarios can cause significant snowpack loss, thereby altering the runoff regime in California. The slight increase in temperature causes a greater fraction of precipitation to fall as rain, rather than snow. This shift causes the freshwater flow hydrograph to represent accentuated rainfall-related peaks, and dampened snowmelt-related peaks.

Along the California coast, data from the 20th century show a 2 mm/y trend of increasing sea level (Flick et al., 2003; Ryan et al., 1999), though yearly mean sea level can fluctuate due to atmospheric and oceanic patterns (e.g. El Nino Southern Oscillation, ENSO). The average trend follows global sea level rise closely, though other parts of the earth experience different rates of rise. Cayan et al. (in press) estimate a range of sea-level rise along the California coast of 11 to 72 cm by 2099, reflecting rates of 1 to 7 mm/y. Included in this analysis are astronomical tides and meteorological forcing. The final projections therefore account for the storm surge associated with low-pressure systems, and any possible co-incidence with astronomical high tides. Also considered are low-frequency meteorological events such as ENSO. The synergy between sea-level rise and storm-associated rise provides greater risk for coastal and estuarine environments (Cayan et al., in press).

2.3 Decreased watershed sediment supply

Anthropogenic activities in many watersheds have reduced the delivery of sediment from the watershed to estuaries and coastal seas (Walling, 2006). The construction of dams on

some the world's major rivers (e.g. Nile River, Colorado River), have completely eliminated net sediment loads past the dams. Inevitably this starves the deltaic and estuarine areas of new sediment, leading to seaward erosion. Further up the watershed, soil conservation measures, intended to reduce adverse effects of logging and urbanization, have simultaneously reduced riverine sediment loads. In California, the reduction of the hydraulic mining pulse and construction of dams have led to a 50% decrease in sediment supply from the Sacramento River between 1957 and 2004 (Wright and Schoellhamer, 2004). During that same period, Suisun Bay eroded at a rate of 0.01 m/y. A continuing decrease of sediment supply could lead to increased erosion in Suisun Bay over the next century.

2.4 Climate change effects on estuarine geomorphology

Research on climate effects on estuarine geomorphology is in its infancy, but there are some recent studies which quantify possible changes in estuary-adjacent marshes. Simas et al. (2001) simulated salt marsh development under sea-level scenarios, and found mesotidal salt marshes to be threatened under worst-case scenarios. Marshes that are accustomed to large tidal ranges are less sensitive to relatively small mean increases in sea level, assuming sediment input is not limited. Pont et al. (2002) reinforce the importance of mineral (sediment) input in light of sea-level rise; they suggest that current sediment supply from the Rhone River is not sufficient to maintain marsh elevation at its mouth.

The dearth of literature on climatic effects on estuarine geomorphology springs from the difficulty of monitoring estuaries over decadal timescales, and the inherent complexity of linking climate, watershed, and estuarine transport models. The effort required to develop and calibrate each model is substantial, and most estuarine transport models are not suited for simulating decadal-scale geomorphology (if calibration data are even available). Nonetheless, understanding modern sediment transport patterns and how freshwater flow and water levels modulate transport allows for an intuitive understanding of climatic effects.

2.4.1 Changes in freshwater flow

Freshwater flows from the watershed are responsible for the majority of new sediment input to many estuaries (Wright and Nittrouer, 1995). In stratified or partially mixed estuaries, the timing and magnitude of flows can significantly alter the vertical and lateral circulation, thus modulating sediment transport within the estuary. In many estuaries the peak freshwater pulse is responsible for delivering an annual pulse of sediment, and also transporting estuarine sediment seaward (e.g. Krone, 1979; Woodruff et al., 2001). If the precipitation regime over the watershed changes in response to climate change, the timing and magnitude of these flow and sediment pulses will change. For instance, in the event of sustained drought, watershed sediment supply would reduce, possibly changing the net direction of sediment transport within the estuary. The estuary would become more oceanic in nature, and salinity and near-bed convergence of flow and sediment would propagate up-estuary. Conversely, in a prolonged wet period, the estuary would become more riverine, encouraging net seaward sediment transport. The timing of

freshwater flow may also be important in estuaries with a seasonal wind signal. For example, the diurnal wind signal in San Francisco Bay is responsible for wind-wave generation starting in the late spring, which in turn resuspends sediment and winnows out fines by then end of summer (Ruhl and Schoellhamer, 2004). If the freshwater flow and sediment pulse were to occur earlier, the length of time for the wind-wave resuspension period and tides to act on flood deposit sediments would be extended. Over decadal timescales, this may lead to an overall deepening of the estuary, and more seaward transport.

2.4.2 Changes in sea level

Sea-level rise directly affects estuaries by modulating water levels within the estuary. Pethick (1993) used changes induced by tectonic sea-level rise to infer changes induced by global warming-related sea-level rise; he found intertidal profiles shifting landward while the estuarine channels became wider and shallower. Other landward movement in biological communities suggested an overall more oceanic condition. Fenster and Fitzgerald (1996), studying the Kennebec River estuary, showed that slowing sea-level rise shifted the estuary towards ebb-dominance, leading to net seaward sediment transport. If one imagines sediment transport within an estuary as riverine forces pushing against oceanic forces, sea-level rise favors the oceanic forces. This will promote up-estuary sediment transport, relatively speaking. A gradual increase in water levels will also increase the inundation of tidal wetlands. If sediment inputs are large enough, the wetlands will accrete and maintain their level, relative to the tide. If sediment inputs are not sufficient, wetlands will recede and regress towards the land (Pethick, 1993; Day et

al., 1999). Prior work has also demonstrated the retreat of coastal forest in response to sea-level rise (Williams et al., 1999). Because sea-level rise is a gradual process, it may be that estuaries can accrete fast enough to not allow for increased tidal prism or increased basin volume. But this is dependent on sediment inputs, mainly from the watershed.

3 Objective A: Development of a reliable modeling approach

3.1 Reliability of models

Reliability of any method, as a measure of performance, indicates reproducibility, stability, and accuracy, among other things. For any measurement method, reliability suggests that results are consistently reproducible and accurate (relative to some standard). The reliability of a model is also based on reproducibility and accuracy, but with regards to the equations it solves and the phenomena being modeled. Debate about the reliability of models must consider where models sit relative to theory and the world.

Morrison and Morgan (1999) identify three features of models: 1) they are constructed in partial independence and dependence on both the world and theory; 2) they function autonomously from the world and theory; and 3) they are capable of representing aspects of the world and theory at the same time. These three features eliminate the common burden that many modelers and users of model-derived knowledge share: the expectation that model results should mimic both the world and theory exactly in every respect. Similar to the idea of conformation, where a representation of a system conforms to some aspect of the system (i.e. a road map of Albuquerque can reliably represent the roads of Albuquerque, but not the distribution of lizard habitat in Albuquerque), reliable models can only be expected to conform to the discretized equations they are solving, or type of observational data they are calibrated to. A reliable model still cannot be expected to represent every aspect of the observational data (e.g. temporal resolution of the model is coarser than real-time), nor is the representation exactly accurate (there is always some quantifiable error). Longino (2002) writes, “Conformation is more suitable than true or

false for expressing the ways in which complex content, such as a theory or model, is successful representation." Therefore, a model that reliably conforms to some aspect of the system of interest can be considered a successful and reliable representation of that aspect. Again, reliability indicates that the model consistently and accurately (within some error tolerance) represents the equations being solved and observations of interest.

Of course this is easier said than done. For a given specialized field of science, there is a path to reliability that may take years, decades, or even centuries to traverse. Examples abound, from thermometry to weather prediction to hydrodynamic modeling. Understanding the complexity and the truly experimental nature of scientific progress, using these examples, will place the current endeavor in the context of the larger path to simulating estuarine geomorphology.

3.2 Path to reliability

In the field of thermometry, investigations sprung from the inadequacy of the qualitative sense of hot and cold. Quantifying the temperature in an absolute sense was the ultimate goal. One of the earliest devices, from the early 17th century, was a simple inverted flask, placed in a vessel of water. It was observed that as the air cooled, the level of water in the flask moved up as the air contracted. Unfortunately, it took further investigations by Pascal, later in the century, to show that the device was also affected by barometric pressure, which had not been understood until his experiments were complete. The natural progression led thermometry towards liquid thermometers, where a sealed tube was filled at high heat with a liquid. Problems arose once it was realized that different

liquids expand at different rates, and that the expansion rate of glass and certain liquids (e.g. mercury) were not as dissimilar as hoped. The subsequent discovery of the ideal gas law, however, led thermometry back to gas, as different gases would respond similarly in a volumetric sense to changes in temperature (i.e. PV=rT). Later on, it was realized that thermal gradients in conductors, such as metals, generated a measurable voltage, and the thermocouple was born. Nowadays, thermocouples are a ubiquitous, cheap, and reliable form of relative temperature measurement. Nonetheless, even these relative temperature instruments are calibrated with gas thermometers, connecting the 21st century to the work of 18th century scientists (Preston-Thomas, 1990). This example shows that a measurement such as temperature, which we consider simple and obvious, requires decades of exploration, discovery, and refinement to become consistent and accurate (to the point where we can take it for granted). Embedded in this process is a seldom-linear interaction between crude observations (inverted flask), theory development (Pascal and barometric pressure), refined observations (sealed flask), and refined theories (ideal gas law) that repeats until stability and reliability are achieved.

If one defines “measurement” as “quantified representation of some quantity”, numerical models provide a measurement method in situations where direct observation is difficult or impossible, as well as a method to predict the evolution of certain parameters with time. In the historical trajectory of science (observation, theory development, and refinement of observation and theory), numerical modeling constitutes an increasingly important component of the process. Modeling integrates observations and theories, and the path to reliability is the same.

A measurement method such as environmental hydrodynamic modeling (where temperature is but one of a plethora of variables) may seem more complex than thermometry, but the progression to reliability is relevantly similar. The basic equations of fluid flow are the Navier-Stokes equations, which balance momentum and viscous forces, based on Newtonian mechanics. The path to these equations was by no means simple; Navier's derivation, which included viscous forces, came almost a century after Bernoulli's dissertation on hydrodynamics, a phrase which he coined (Darrigol, 2005). Solving these equations analytically is only possible for a limited class of problems with specific boundary conditions. For example, a solution can be found for cases of steady, laminar, parallel, one-dimensional flow between two plates (Couette flow). Approximately solving the full set of equations for less stringent cases has only recently become possible, through the use of finite-difference schemes and computer-solvers. Idealizing the Navier-Stokes equations into a set of discretized equations still requires simplifications and assumptions, but use of three-dimensional hydrodynamic models is now considered reliable after three centuries of work. This reliability springs partly from the relationship of the model to the equations (discretization), but also from relationship of the models to observations in the world (calibration). Those observations of things like temperature, flow velocity, and pressure, were all possible through successes and failures analogous to thermometry.

Similar to the task in this study, Lynch (2006) details the history of numerical weather prediction, through the work of L.F. Richardson. Richardson used a finite-difference scheme, by hand, to calculate changes in weather variables. Though his results were not

satisfactory, modern methods have validated his approach, and suggested that the flaw lay in the initial conditions (see Section 3.5). At the time, Max Margules, an Austrian meteorologist, suggested that prediction of the weather was "immoral and damaging to the character of a meteorologist" (Lynch, 2006). Margules based this statement on analysis of predicting pressure changes, finding that the methods were subject to large errors. Modern meteorology has shown this alarmism to be premature, and efforts on the part of Richardson, though they may have been error-prone, laid the groundwork for future research. In a recent book, Pilkey and Pilkey-Jarvis (2007) paint quantitative modeling with a broad brush, labeling the use of environmental models as "useless arithmetic". This declaration is an echo of Margules, who suggested that numerical weather prediction should have ground to a halt in the early 20th century. It is far easier to quit because of a difficult road ahead, than to advance the method through alternating failure and success.

The task for this study, the numerical prediction of estuarine geomorphology, is still very well in its infancy. As noted in Section 2.1, conceptual efforts towards numerical prediction began in the last decade of the 20th century, so the field is barely two decades old. Whatever successes or failures are realized by this study will become part of the progression towards a reliable scientific method.

3.3 Simulation and exploratory modeling

Murray (2003) identifies an axis of modeling practice that ranges from "simulation" models to "exploratory" models. The latter practice involves representing what appear to

be the most crucial processes, and eliminating second-order processes. As results are generated, it may be revealed that an omitted process must be included. Simulation modeling, in Murray's context, instead includes every process that can be modeled, whether or not the process is of first-order importance for the task at hand. Ideally, there is a balance on this axis that can be found by starting at one end and working towards the middle. I choose to begin at an intermediate point on the axis, based on available modeling packages, and add features as needed.

In the context of coupled hydrodynamic and sediment transport models, most packages begin towards the simulation model end of the axis. The main aspects of three-dimensional, free-surface fluid flow are implemented, including buoyancy, turbulence, and bottom-boundary layer parameterization. Observations of hydrodynamics have shown that these processes are important to flow patterns, and must be modeled. In contrast, sediment transport modeling is relatively more primitive: most processes are relatively gross parameterizations, from specification of settling velocity to erosion rate. In fact, the values of those parameters are frequently used as calibration parameters, varied until the best agreement is found between the model and field data. Some researchers have implemented more complex sediment transport modules into practice, such as biological bed stabilization and flocculation. However, adding complexity to a grossly parameterized model may be counterproductive. Alternatively, sensitivity analyses can provide bounds on the uncertainty involved with ignoring complex processes that are poorly understood (such as biological bed stabilization). For example, if a critical shear stress of 0.2 Pa is specified, one may assume that the presence of bio-

stabilizers will increase strength by 50%, to 0.3 Pa. The model is then run with both values, and the difference is an estimate of the uncertainty involved with ignoring bio-stabilization or any other process that affects critical shear stress.

3.4 Calibration, validation, verification, and the multiple-timescale approach

Calibration denotes the tuning of model parameters to match observed data or an analytical solution (Oreskes et al., 1994; Roache, 1997). Validation is the process of proving the calibrated model is capable of accurately simulating another variable that was not calibrated to, or accurately simulating a different temporal period. Verification involves certifying that the right equations are being solved in the correct manner. For example, a hurricane trajectory model can be verified by ensuring that the numerical equations for air-sea interaction are discretized and solved correctly, calibrated by adjusting drag coefficients and frictional factors, and validated by either proving that the hurricane path model is accurate for a different simulation period, or that the simulated hurricane transit time during the calibration period, for example, is accurate. Implicit in this description is the question of degrees and error tolerance: there is no expectation of perfect matching to any data, but matching within a specified range (Roache, 1997), which is standard engineering practice.

Here I am not concerned with verification, which is the domain of the model architects, but only with the appropriate application of calibration and validation steps for the three preliminary modeling exercises (Chapters 6, 7, and 8). In reference to the idea of model autonomy and representation, verification solidifies the link between the model and

theory, calibration solidifies the link between the model and the world, and a verified, calibrated, and validated model is the link between the world and theory.

For the first modeling exercise I address the tidal-timescale mechanics of the model (Table 3.1). Modern data in estuaries can be collected at sub-hourly time steps, so both the calibration and validation data sets will be of a high temporal resolution. I can calibrate the model to tidal water levels at multiple locations, and validate by comparing observed and modeled tidal changes in longitudinal and vertical salinities. The final goal is to compare observed and modeled movement of the estuarine turbidity maximum (ETM): the ETM is the location of near-bed, convergent sediment transport, which usually causes accumulation of sediment (and thereby affects geomorphology). ETM location is sensitive to hydrodynamics and salinity dynamics. Proper representation of the ETM will give confidence in the model's ability to reproduce tidal-timescale phenomena that may affect longer-term processes in the estuary. For example, during a year with very high sustained freshwater flow, the ETM will not persist. Under these conditions, sediment dynamics near the typical ETM location will be altered significantly, leading to an annual-timescale change in deposition or erosion.

Once the tidal-timescale evaluation is complete, the annual-timescale simulations will test the model's ability to represent inter-annual sediment transport features. Here, I will calibrate and validate to five years of tidally averaged sediment flux data, but use a portion of the data for calibration, and the remaining portion for validation (Table 3.1). Calibration and validation data, in this case, are of the same type but different temporal

period. This is in contrast with the tidal-timescale application, where I use data of a different type but same temporal period for validation. Accurate performance for this step will establish the model's success in representing sediment delivery from large flow events, landward transport of sediment due to gravitational circulation, and the effect of wind-waves on the net sediment budget in the estuary. Decadal-scale changes in these patterns will accumulate to determine decadal-scale geomorphology in the estuary. For example, a decade-long drought would greatly reduce sediment delivery to the estuary, and perhaps cause net erosion over that decade.

The final model evaluation step involves the decadal-timescale modeling of estuarine bathymetric change (Table 3.1). Bathymetric data from this period is temporally sparse and spatially dense, but spans periods where system behavior was highly variable (due to rapid changes in sediment supply, land-use, and bathymetry itself). In this case, validation is not an option. There is large uncertainty in the conditions of the system during historical periods. For example, calibration to one set of parameters for the first time period (1867-1887), may be successful, but validating to the next time period, 1887-1922, may fail. This could be attributed entirely to a real change in sediment bed parameters during that time. Therefore it is not fruitful to attempt a standard validation step for this application. Instead, I can conduct a sensitivity analysis, and establish the utility of the "scenarios of change" concept.

Table 3.1 Multi-step calibration procedure for three process timescales. Sediment properties include critical shear stress and settling velocity.

Timescale	Feature of interest	Calibration data	Validation data	Parameters varied
Tidal	ETM	Tidal stage	Salinity dynamics	Bottom roughness
Annual	Sediment fluxes	Sediment fluxes (1997, 2004)	Sediment fluxes (1998, 2002, 2003)	Sediment properties, wave period
Decadal	Bathymetry	Bathymetry	N/A	Sediment properties, wave period

3.5 Scenarios of change

My final goal of simulating geomorphic change in response to future scenarios of climate change, sea-level rise, and decreased sediment supply is bolstered by simulations of tidal, annual, and decadal-timescale sediment transport processes. Despite this robust methodology, I am not attempting absolute predictions of geomorphology into the future, only changes in geomorphology in response to possible changes in future conditions. For example, I will perform four 20 year simulations of geomorphic change, one as a base-case scenario, and three as prescribed future scenarios. The difference between the geomorphic results will be an illustration of how much geomorphology may be affected by future changes, though I am not suggesting that geomorphic prediction in the individual scenarios represents the trajectory of the actual world. This perhaps satisfies critics of quantitative modeling, such as Pilkey and Pilkey-Jarvis (2007), by not claiming to predict the future. There is enough uncertainty in the model parameters that I cannot accurately predict absolute geomorphology. However, I can perform sensitivity analyses on major parameters for both the base-case and one scenario of change. The original bathymetric change results, $\Delta h(\xi)$, are defined as

$$\Delta h(\xi) = \Delta h(\xi)_{\text{base-case}} - \Delta h(\xi)_{\text{future}} \tag{3.1}$$

and the sensitivity analyses results, $\Delta h(\xi + \xi')$, as

$$\Delta h(\xi + \xi') = \Delta h(\xi + \xi')_{\text{base-case}} - \Delta h(\xi + \xi')_{\text{future}} \tag{3.2}$$

where $\Delta h(\xi)_{\text{base-case}}$ is the base-case run with the original parameters, $\Delta h(\xi)_{\text{future}}$ is the future run with the original parameters, $\Delta h(\xi + \xi')_{\text{base-case}}$ is the base-case run with perturbed parameters, and $\Delta h(\xi + \xi')_{\text{future}}$ is the future run with perturbed parameters. Under different parameter perturbations, if I can show that

$$\Delta h(\xi) \sim \Delta h(\xi + \xi') \tag{3.3}$$

then the geomorphic change results are insensitive to parameter specification, and the differences of geomorphic scenarios behave linearly. This relationship will most likely vary depending on the size of the perturbation, but I can use values that span the parameter uncertainty estimated in other studies.

3.6 Sources of uncertainty

Haff (1996) details multiple sources of uncertainty in geomorphic simulations, which are broadly relevant to all modeling endeavors. The sources are 1) model imperfection; 2) omission of processes; 3) lack of initial condition information; 4) sensitivity to initial

conditions; 5) unresolved heterogeneity; 6) inaccurate external forcing; and 7) inapplicability of the safety factor concept (Haff, 1996). Exploring these sources in the context of the present modeling endeavor will both highlight strengths and limitations of the model formulation and approach. Detailing the sources of uncertainty is the first step in mitigating the effects using appropriate methods, such as robust calibration and sensitivity analyses. Because these simulations involve hindcasting back over 100 years, there is clearly some inherent uncertainty that must be addressed, as historical information is limited. This discussion is intended to identify possible sources of uncertainty; this is by no means a comprehensive list, as more sources may arise during development and application.

Model imperfection

Numerical models which solve equations of motion are limited in their capacity to solve and parameterize the important processes. Even for well-understood processes such as fluid flow in an open channel, there are limitations regarding specifying bottom friction, turbulence within the flow, not to mention numerical solution methods. Several processes are parameterized based on field and laboratory measurements, as there are no purely deterministic equations available to solve in some cases.

Within the modeling framework used here, a few notable processes are parameterized. The turbulence model implemented here gives several options for solving the turbulence closure problem; each option varies in performance depending on the system of interest. The necessity for several options highlights the imperfection, in general, of turbulence

closure methods. Another example of a model imperfection is the specification of wind-waves. Due to computational limitations, I cannot use state-of-the-art wave parameterization routines, and instead use a simpler parameterization based on collected wind/wave data, in a very different system (Coastal Engineering Research Center, 1984). Transferring an idealized wave field to the bed, to determine wave-induced bottom stress, is another parameterized process based on a deterministic function (Dean and Dalrymple, 1991). Other examples are the parameterization of particle settling velocity, bed density, critical shear stress, and erosion rate.

Omission of processes

Computational and scientific limitations necessitate the omission of processes that may or may not be critical to the system of interest. There are essentially two axes to be considered when discussing processes: the axis of importance, and the axis of "modelability". For a given modeling endeavor, such as estuarine geomorphic change, a process may be of no importance (e.g. local precipitation), high importance (e.g. wind-wave resuspension), or unknown importance (particle flocculation). Only processes which are important or of unknown importance need to be considered for implementation in the model. The next consideration is the modelability of the process. While the interaction between wind-waves and the sediment bed are straightforward (wave orbital velocity inducing shear stress on an erodible bed), flocculation is a difficult and computationally expensive process to represent, due to the complexity of particle-particle interactions. In these cases, a process such as flocculation must either be parameterized or argued away. However, one can assume that flocculation mainly affects settling velocity

and particle density, therefore a sensitivity analysis of those parameters quantifies a range of error involved in omitting flocculation. Several processes of either unknown or intermediate importance have been neglected here, including bio-stabilization, flocculation, bed consolidation, among others. Ideally, a sensitivity analysis of all major parameters can capture the uncertainty involved with omitting processes.

Lack of initial condition information

For many modeling simulations, it is necessary to initialize the model prior to the time period of interest, to allow the model to spin-up and reach a quasi-equilibrium. Model behavior during the period of interest will be sensitive to the initial conditions, therefore the quality of initial condition data will affect the quality of the simulation. However, not all initial condition data are easily obtained, and in some cases must be estimated.

The historical nature of these simulations highlights the difficulty of specifying initial conditions. Initial conditions are needed for bathymetry, sediment supply (watershed and seaward sources), sediment bed parameters, and estuary configuration. Bathymetry was measured historically, though the quality of these data are not up to modern standards. The remaining parameters are not easily quantifiable, and must be used as calibration parameters, estimated using anecdotal evidence, or some combination of the two. For these simulations, most parameters will be adjusted to match historical bathymetric change data. Because the system was not in any sort of quasi-equilibrium during the 19th century due to hydraulic mining, crude estimation of initial conditions may be appropriate.

Sensitivity to initial conditions

Initialization of the model and the subsequent spin-up are necessary to bring the model into the desired simulation period. However, the slight perturbation of a given parameter at initialization can cascade through the numerical solution, thereby changing the trajectory of the model. Again, a sensitivity analysis can give a range of system trajectories, though it is impossible to test the sensitivity to every parameter.

Regarding simulations of estuarine geomorphic change, Schoellhamer et al. (in press) show that a 10% perturbation in key parameters, for a system in equilibrium, requires over 10 y to establish a new equilibrium. Therefore, shorter term (<10 y) simulations of systems in quasi-equilibrium are sensitive to the specification of initial conditions. The system being modeled here, however, was in severe disequilibrium due to the catastrophic input of sediment during hydraulic mining. While the simulations may be sensitive to some initial parameters, the major forcings are more dominant than small errors in initial conditions. Successful calibration to historical data will imply a relative insensitivity to initial conditions.

Unresolved heterogeneity

Resolving a natural landscape onto a discretized grid requires the averaging of certain parameters over larger areas. For instance, while critical shear stress may vary over a few meters on an intertidal mudflat, it is impractical to resolve an estuarine model at those scales, and the critical shear stress over a 100 x 100 m area must be specified instead. Compounding this problem is the lack of field data on heterogeneity in certain

parameters. There are few parameters that can be measured at typical grid resolution in the field, such as bathymetry (surveying vessels) and surface water clarity (satellite imagery).

Major parameters that are treated as spatially homogeneous here are wind speed and direction, and sediment bed parameters. Sediment bed parameters are varied between two large portions of the domain (Suisun Bay and the Delta). Despite initial unresolved heterogeneity, some characteristics do resolve themselves as the simulation progresses: bed thicknesses and average critical shear stress (mixture of a strong and weak sediment class) will evolve with time, in response to hydrodynamic forcing.

External forcing

The first-order forcing functions within a simulation are prone to uncertainty if episodic or unpredicted events are common, and not specified. In nonlinear systems, episodic forcing can be the dominant mechanism of interest, and must be quantified. For estuarine hydrodynamic modeling, the main external forcings are tides, freshwater flow, and wind. The tides are responsible for inducing oscillatory currents, while freshwater flow provides watershed sediment and a contribution to density-driven flow. Winds are responsible for generating wind-waves that erode sediment in shallow areas.

Fortunately, tides are controlled by astronomical forcing, which is highly predictable using modern tidal harmonic data. There is the possibility that tidal harmonics in the present era may not be optimal for the historical era, due to changes in tidal prism and

basin geometry, but as a first approximation these data are sufficient. Freshwater flow data are not available prior to 1929, but methods have been developed to estimate historical flows (Ganju et al., in review) that still reproduce episodic events. Winds follow a predictable pattern over San Francisco Bay, though there are variations in direction, timing of storm-associated winds, and relative magnitude. Synthetic functions are used here to represent the seasonal, weekly, and diurnal signals of wind strength that are common over San Francisco Bay. There are unknown processes that can present themselves in an abrupt fashion, such as the dramatic invasion of exotic benthic organisms (Carlton et al., 1990).

Inapplicability of the safety factor concept

In engineered systems, one knows the interaction of constructed materials and external forcings, and a factor of safety can be introduced to cover the a range of possible behaviors. In a natural system, the interaction of heterogeneous materials and variable forcing cannot be scaled with a linear factor of safety. A possible solution is application of a worst-case scenario, though the model will be least reliable when applied to an extreme case outside of its calibration space. Between simulation of extreme scenarios and sensitivity analyses, the behavior range of the model should be bracketed in the same sense as a safety factor.

4 Model equations, solution procedures, and infrastructure

The Regional Ocean Modeling System (Shchepetkin and McWilliams, 2005) is a public-domain hydrodynamic model with an optional sediment transport module. There are several important attributes of ROMS: it is 1) free, public-domain software; 2) improved and expanded amongst hundreds of researchers; and 3) part of a community-based sediment transport initiative by the U.S. Geological Survey. The version discussed here is the Rutgers 3.0 version. Other models, such as Delft3D, have been applied to similar problems (e.g. Lesser et al., 2004; Roelvink, 2006).

In the following sections I describe the general equations that are solved by the numerical code, but the full details are beyond the scope of this work. This study is concerned with the development of application procedures for simulating sediment transport processes, not the development of numerical methods. The reader is directed to several primary sources, as well as the open source code itself, for model details. Modeling details specific to each application, such as domain, boundary conditions, and external forcing, are discussed in Chapters 6-9.

4.1 Hydrodynamics and tracers

ROMS, like many hydrodynamic models, solves the Reynolds-averaged Navier-Stokes momentum equations, with a finite-difference approach. Hydrostatic pressure is assumed, as is the Boussinesq approximation. It is a split-mode model: the barotropic, depth-integrated equations are solved on a shorter (fast) time step (due to barotropic propagation speed) while the baroclinic terms are solved at a longer (slow) time step.

In the sigma-coordinate system, depth variable s is defined as:

$$s = \frac{z - \eta}{D} \tag{4.1}$$

where z is the standard vertical coordinate with the origin at the sediment bed, η is the free surface elevation, and D is the total water depth, with $-1<s<0$. Therefore the momentum and continuity equations in the sigma-coordinate system are as follows:

x-direction momentum:

$$\frac{\partial(Hu)}{\partial t} + \frac{\partial(uHu)}{\partial x} + \frac{\partial(vHu)}{\partial y} + \frac{\partial(wHu)}{\partial s} - fHv = -\frac{H}{\rho_0}\frac{\partial p}{\partial x} - Hg\frac{\partial \eta}{\partial x} - \frac{\partial}{\partial s}\left(\overline{u'w'} - \frac{\upsilon}{H}\frac{\partial u}{\partial s}\right) \tag{4.2}$$

y-direction momentum:

$$\frac{\partial(Hv)}{\partial t} + \frac{\partial(uHv)}{\partial x} + \frac{\partial(vHv)}{\partial y} + \frac{\partial(wHv)}{\partial s} + fHu = -\frac{H}{\rho_0}\frac{\partial p}{\partial y} - Hg\frac{\partial \eta}{\partial y} - \frac{\partial}{\partial s}\left(\overline{v'w'} - \frac{\upsilon}{H}\frac{\partial v}{\partial s}\right) \tag{4.3}$$

s-direction momentum:

$$0 = -\frac{1}{\rho_0}\frac{\partial p}{\partial s} - \frac{g}{\rho_0}H\rho \tag{4.4}$$

with continuity as

$$\frac{\partial \eta}{\partial t} + \frac{\partial (Hu)}{\partial x} + \frac{\partial (Hv)}{\partial y} + \frac{\partial (Hw)}{\partial s} = 0 \tag{4.5}$$

where x is the east-west direction, y is the north-south direction, H is layer thickness, u is x-direction velocity, v is y-direction velocity, w is s-direction velocity, f is the Coriolis parameter, ρ_0 is the fluid density, p is pressure, η is the water surface elevation, and υ is the kinematic viscosity.

The Reynolds stresses are parameterized following Boussinesq's analogy as follows:

$$\overline{u'w'} = -K\frac{\partial u}{\partial s} \tag{4.6}$$

$$\overline{v'w'} = -K\frac{\partial v}{\partial s} \tag{4.7}$$

where K is the eddy viscosity. Furthermore,

$$K \propto k^{\frac{1}{2}} l \tag{4.8}$$

where k is the turbulent kinetic energy and l is a length scale. As with most two-equation turbulence models, the differential transport equation for k is the first equation. For the

second transport equation, the generic length scale approach (Umlauf and Burchard, 2003) is available, which allows for specification of a second transported quantity ψ, as follows:

$$\psi = c^p k^m l^n \tag{4.9}$$

where c is a stability coefficient; p, m, and n are coefficients that modulate the second quantity. Length scale l is defined as:

$$l = \frac{c^3 k^{3/2}}{\varepsilon} \tag{4.10}$$

where ε is the dissipation rate. Differential transport equations are then solved for k and ψ. I use the k-ε formulation which is obtained by substituting p=3, m=1.5, and n=-1 into Eqs. 4.9 and 4.10; the model then solves the following differential transport equations for k and ε:

$$\frac{\partial k}{\partial t} + U_i \frac{\partial k}{\partial x_i} = \frac{\partial}{\partial z}\left(\frac{K}{\sigma_k}\frac{\partial k}{\partial z}\right) + P + B - \varepsilon \tag{4.11}$$

$$\frac{\partial \varepsilon}{\partial t} + U_i \frac{\partial \varepsilon}{\partial x_i} = \frac{\partial}{\partial z}\left(\frac{K}{\sigma_\varepsilon}\frac{\partial \varepsilon}{\partial z}\right) + \frac{\varepsilon}{k}(c_{\varepsilon 1}P + c_{\varepsilon 3}B - c_{\varepsilon 2}\varepsilon) \tag{4.12}$$

where σ_k is the Schmidt number for the eddy diffusivity of turbulent kinetic energy, σ_ε is the Schmidt number for the eddy diffusivity of dissipation, P is the production of turbulent kinetic energy by shear:

$$P = -\overline{u'w'}\frac{\partial u}{\partial z} - \overline{v'w'}\frac{\partial v}{\partial z} \tag{4.13}$$

B is the production of turbulent kinetic energy by buoyancy,

$$B = -\overline{\rho'w'}\frac{g}{\rho_0} \tag{4.14}$$

and $c_{\varepsilon 1}$, $c_{\varepsilon 2}$, $c_{\varepsilon 3}$ are constants. Further details of this method, including selection of coefficients and a discussion of the closure performance, can be found in Warner et al. (2005b).

Conservative and non-conservative scalar transport (including salinity) is solved using the advection-diffusion equation, with source and sink terms, as follows:

$$\frac{\partial(HC)}{\partial t} + \frac{\partial(uHC)}{\partial x} + \frac{\partial(vHC)}{\partial y} + \frac{\partial(wHC)}{\partial s} = -\frac{\partial}{\partial s}\left(\overline{C'w'} - \frac{\upsilon_c}{H}\frac{\partial C}{\partial s}\right) + C_{\text{source}} - C_{\text{sink}} \tag{4.15}$$

where

$$\overline{C'w'} = -K_c \frac{\partial C}{\partial s} \tag{4.16}$$

and C is the scalar concentration, υ_c is the kinematic diffusivity of the scalar, C_{source} and C_{sink} are source and sink terms, and K_c is the eddy diffusivity of the scalar. The source and sink terms for suspended-sediment are described in the next section.

4.2 Suspended-sediment transport and bed model

Along with the advection-diffusion equation for suspended-sediment transport, source and sink terms are needed for bed erosion and deposition. ROMS has the capability of simulating multiple size classes; each size class is treated as an independent quantity. The sediment source term, bed erosion, is given by Ariathurai and Arulanandan (1978) as:

$$C_{\text{source}} = \varepsilon_s (1-n)\left(\frac{\tau_w}{\tau_c} - 1\right) \text{ for } \tau_w > \tau_c \tag{4.17}$$

where ε_s is the erosion rate constant, n is the bed porosity, τ_w is the shear stress exerted on the bed, and τ_c is the critical shear stress of the sediment bed.

The sediment sink term, deposition, is given by

$$C_{\text{sink}} = \frac{\partial w_s C}{\partial s} \tag{4.18}$$

where w_s is the bulk settling velocity of the size class.

Multiple bed layers may be specified, with each layer composed of a user-specified mixture of sediment classes. The properties of the mixed class bed, such as critical shear stress, are weighted using the average mass fractions of the classes. The details of the bed layer model are given by Warner et al. (in press).

Bed stresses in bottom-boundary layer can be parameterized using multiple options: linear stress formulation, quadratic stress formulation, logarithmic stress formulation, or options that include wave-current interaction. The first application (Chapter 6) uses the logarithmic stress formulation, while the remaining applications (Chapters 7, 8, and 9) use a wave-current interaction module. Initial simulations were performed ignoring wind-waves, subsequently wind-waves were added due to their importance on geomorphic change. This module is based on Madsen (1994) as implemented by Warner et al. (in press); they detail the bottom-boundary layer module and the other modes available. Two bedload transport formulations, Meyer-Peter Mueller (1948) and Soulsby and Damgaard (2005) are also available (but not implemented for this study).

4.3 Solution schemes

Solving the barotropic and baroclinic terms separately, known as mode-splitting, introduces some difficulty with regards to aliasing and solution methodology. The numerical code of the ROMS model has been optimized to alleviate these problems. The description of the solution methodology can be found in detail in Shchepetkin and McWilliams (2005).

For solution of the momentum equations, the ROMS code provides a 2nd-order centered scheme, a 3rd-order upstream-bias scheme, and a 4th-order centered scheme (in space). A splines vertical advection scheme is provided for shallow, highly resolved applications. Parameterization of horizontal mixing can be specified using either a Laplacian or biharmonic scheme. For solution of the advection-diffusion equation, options are similar to schemes for momentum, with the inclusion of a recursive Multi-dimensional Positive Definite Advection Transport Algorithm (MPDATA).

4.4 Boundary conditions and external forcing

4.4.1 Landward flow and tracer concentrations

At landward boundaries, volumetric water flow (m^3/s) and scalar concentration (C units) can be introduced. The magnitudes can either be specified analytically or using an input forcing file as described in Section 4.5. In either case, the values can be specified for each boundary cell individually, while momentum can be specified as a vertically averaged quantity as well. Options for the boundary condition include 1) clamped, 2) radiation, and 3) gradient. The clamped condition will hold the momentum and/or tracer magnitude at

the specified value at the boundary, though at tidally affected landward boundaries the flood-tide value at the first interior cell will respond to seaward conditions. The radiation condition will clamp values when the landward boundary is not affected by seaward conditions, but allow for the values to respond in cases where flood tide reaches the landward boundary. Finally, the gradient option simply enforces a zero-gradient condition at the boundary.

4.4.2 Seaward velocity, stage, and tracer concentrations

To tidally force the model at seaward boundaries, depth-averaged momentum (uniformly distributed in the lateral) and water level are specified. Scalar concentration can also be introduced; in these applications scalars are distributed uniformly in the lateral and vertical. Again, magnitudes can either be specified analytically or using an input forcing file as described in Section 4.5. Only the depth-averaged momentum is necessary; if desired the three-dimensional momentum can be specified (clamped or radiation) or allowed to respond in a zero-gradient fashion (gradient). The clamped condition will hold the momentum and/or tracer magnitude at the specified value at the boundary, regardless of landward freshwater flow inputs. The radiation condition will clamp values when the seaward boundary is not affected by freshwater point sources (flood tide), but will allow for the values to respond to a net freshwater outflow (or tracer transport) on ebb tide.

4.4.3 Wave-induced orbital velocities

Wave-generated bottom orbital velocities can be specified explicitly, by providing spatially and temporally varying significant wave heights, directions, and periods, or by

using the SWAN model (Booij et al., 1999) to solve for wave generation and propagation within the domain. In the former case, bottom orbital velocities are calculated using the approximation of Dean and Dalrymple (1991), and used within the bottom-boundary layer module (Section 4.2) to calculate bed shear in the presence of wave-current interaction (Madsen, 1994; Styles and Glenn, 2000). Specifying wave heights is performed using the methods of the Shore Protection Manual (CERC, 1984). Simulations in Chapter 6 do not specify any wave forcing; Chapter 7 simulations use a spatially constant wave field (constant water depth of 4 m); and Chapter 8 and 9 simulations calculate wave height as a function of water depth, due to the rapidly changing geomorphic change.

4.5 Infrastructure

4.5.1 Platform and operating system

The ROMS model was installed on a dual-processor Dell Precision 670 computer, running a Linux operating system. The only proprietary software used to compile the model was the Intel Fortran Compiler for Linux (Version 8.0), though MATLAB software was used for pre-and post-processing. All necessary program files are available from the ROMS website (http://www.myroms.org).

4.5.2 Pre- and post-processing

All grid and forcing files must be in Netcdf format, which is a public-domain file format that allows for the generation, reading, and writing of files with multiple variables. The Netcdf libraries must be installed on the computer, and a viewer must be installed to view

and alter the files. The MATLAB Netcdf toolbox, available at http://mexcdf.sourceforge.net, is a public-domain viewer that can create, read, and write Netcdf files. Grids may be generated using the public-domain Seagrid utility for MATLAB (http://woodshole.er.usgs.gov/staffpages/cdenham/public_html/seagrid), or specified analytically.

Output from the model (history) is sent to Netcdf files; the frequency of data writing and the maximum file size can be specified. Multiple files will be written if the output exceeds the maximum file size. A restart file is also generated at a user-specified interval; this file can be used to restart the model at the latest saved time-stamp. The user specifies which variables are written to the history files, while the restart files are automatically filled with the necessary primitive variables needed for a restart run. All post-processing for this study was done with MATLAB software.

5 Site description

5.1 California climate

California's climate follows a Mediterranean pattern: dry, warm summers, and cool, wet winters. The passage of Pacific storms during the winter months brings rain to the Central Valley, and snow to the higher elevations of the Sierra Nevada (Fig. 5.1). Episodic winter storms typically induce high winds and barometric pressure lows. As the spring begins, reliable sea-breezes begin from the Pacific Ocean to the Central Valley. These winds are typically diurnal, with a quasi-weekly signal due to prolonged heating and cooling of the Valley.

Recent studies have suggested that the timing of streamflow in the western United States, including California, is shifting earlier due to changes in the timing of precipitation and air temperature (Aguado et al., 1992). Coupled snowpack/watershed models have been used to quantify the effect of increased temperature on streamflow; slight increases in air temperature will alter the amount of snowpack stored in the Sierra Nevada, and the timing of the snowmelt-derived runoff. This ultimately alters the timing and magnitude of streamflow from the Sierra Nevada watershed (Knowles and Cayan, 2002). Future trends in storm frequency and intensity are unknown, but may also vary with climate change.

5.2 Central Valley and watershed

The Central Valley of California and its surrounding areas form a 154,000 km^2 watershed, with diverse land-use and terrain. The valley is bounded on the east by the Sierra Nevada, and on the west by the Coast Range. Land use is mainly agricultural,

though residential use is increasing as population rises. The terrain ranges from alpine areas and foothills to riparian corridors and freshwater marsh.

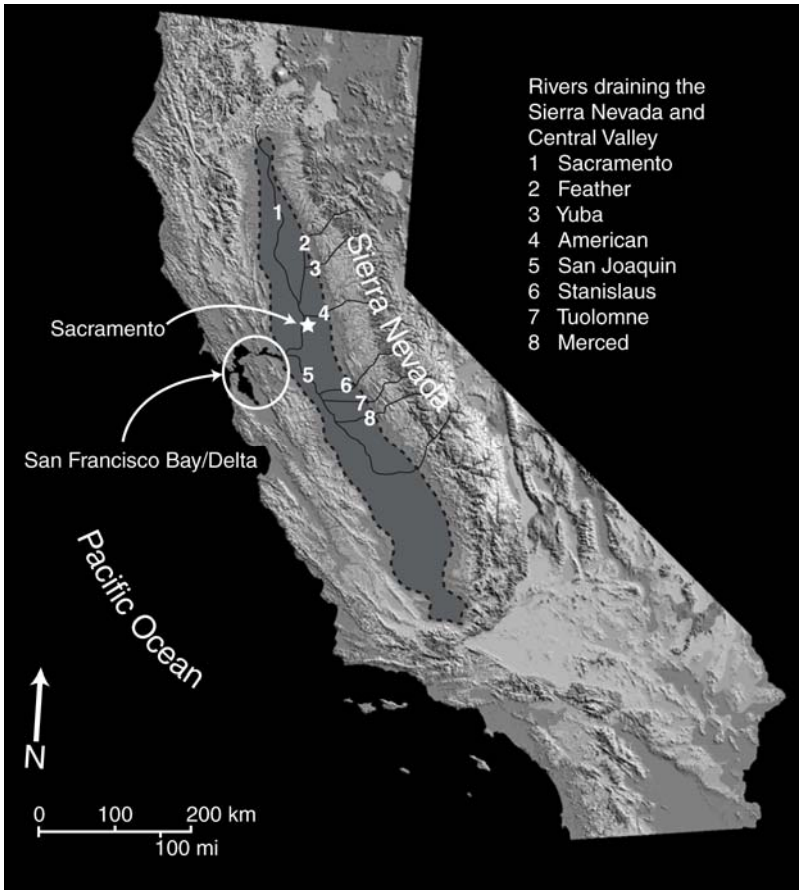

Figure 5.1 California, Central Valley (bounded by dashed line), Sierra Nevada, and major rivers.

The east side of the Central Valley is bordered by the Sierra Nevada mountain range, which is the source of the eight major rivers that run through the valley: the Sacramento, Bear, Yuba, Feather, San Joaquin, Stanislaus, Merced, and Tuolomne Rivers. The Sacramento River, controlled by Shasta Dam, is the largest conduit of freshwater flow. These rivers are all controlled by upstream reservoirs, located in the foothills of the mountains. The main source of water to these reservoirs is snowmelt from the Sierra Nevada snowpack, which peaks in the spring. Reservoir storage began in the 19th century

(Fig. 5.2) and accelerated through the 20th century, leveling off by the end of the 20th century.

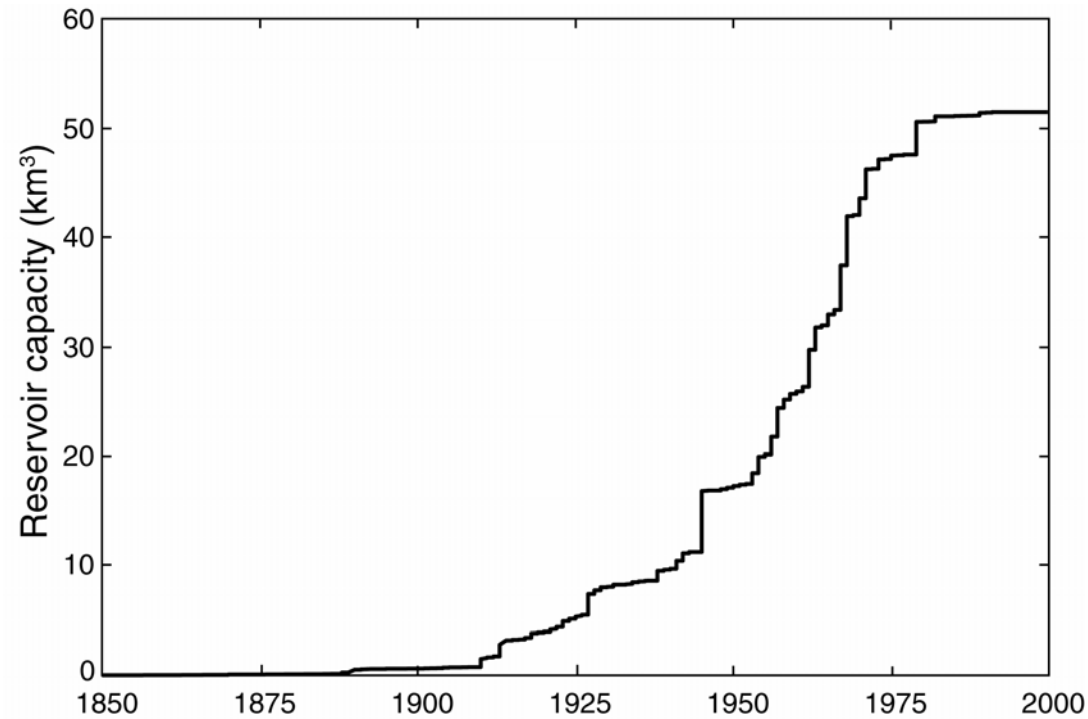

Figure 5.2 Reservoir capacity in California. Increasing capacity signals increasing management of the hydrologic system.

5.3 Sacramento and San Joaquin River Delta

While the reservoirs in California are responsible for water storage, the Sacramento/San Joaquin River Delta is where the water transfer (export) facilities are located. The Delta is a complex network of natural and engineered channels, with control gates, pumps, and levees (Fig. 5.3). Both state and federal water projects export water from the Delta to supply agricultural and residential needs in the southern half of the state. Tidal forcing from the Pacific Ocean propagates into the Delta, and tidally averaged salinity rarely exceeds 2, due to freshwater flow management. Flows are regulated to maintain water quality at the export pumps.

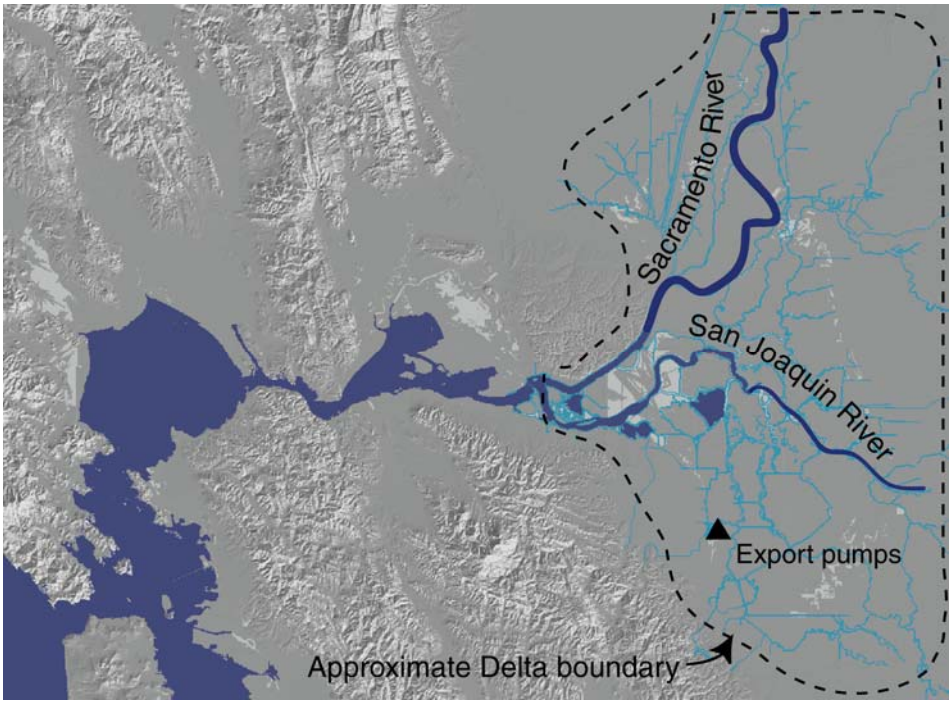

Figure 5.3 Land-water terrain map of San Francisco Bay and the Sacramento/San Joaquin Delta. State and federal programs export water from the southern Delta.

Prior to human modification, the Delta was a large tidal wetland (Thompson, 1957), and there were periods of relatively high salinity during low-flow periods (Means, 1928). Flows are now regulated to maintain water quality in the Delta for drinking water purposes. Starting in the 19th century, the fertile nature of the Delta peat soils encouraged settlers to dike and drain Delta wetlands, for agricultural purposes. The dewatering of these peat soils caused oxidation and subsidence; substantial areas of the Delta are now below sea level and are dependent on levees to stay dry. Some of these subsided "islands" have been flooded and are now open water areas.

The depositional history of the Delta is not straightforward; it can be assumed that prior to human alteration the Delta was a largely depositional marsh. The subsequent release of

mining debris clogged most Delta waterways, but dredging and construction of levees also removed some debris from the waterways. The Sacramento and San Joaquin River channels were maintained at relatively shallow depths (~ 7 and 9 ft, respectively) during these periods, suggesting that deposition was actively occurring. The relative rates of deposition, however, are not easily ascertainable. Depth, configuration, and hydraulic efficiency of the Delta would determine the trapping efficiency, and these data are not readily available for historical periods. Detailed discussion of Delta reclamation can be found in Thompson (1957).

Recent studies on sediment transport in the Delta (Wright and Schoellhamer, 2004; 2005) established a sediment budget for the Delta which demonstrates its current depositional nature. Reduced sediment supply from the watershed, due to a reduction in mining debris and sediment trapping behind dams, will reduce the amount of sediment trapped in the Delta, though trapping efficiency (fraction of input retained) may remain constant. Currently, net yearly trapping efficiency is inversely proportional to net yearly flow volume, i.e. the greater the freshwater flow, the lower the trapping efficiency. Sediment loads from the Delta have been decreasing since the peak of hydraulic mining, and may continue to decrease into the next century.

5.4 Suisun Bay

Suisun Bay is the landward-most subembayment of San Francisco Bay, and spans from the Sacramento/San Joaquin River Delta at the landward end to Carquinez Strait at the seaward end (Figs. 1.1, 1.2). Over one-half of the bay is shallower than 5 m at mean-

lower-low-water (MLLW), though numerous deep-water (> 10 m) channels run longitudinally through the bay. Two large shallow areas, Grizzly and Honker Bays, lie on the northern edge of the main channels. The northern half of the channel continues northeast into the Reserve Fleet channel and terminates in Grizzly Bay, while the southern half of the channel runs east-northeast along the southern edge of the bay. The two channels are separated by a shallow bar, portions of which are exposed at low tide. Carquinez Strait connects Suisun Bay and San Pablo Bay. Maximum depths in Carquinez Strait approach 30 m, while both Suisun and San Pablo Bay are relatively shallow, with deep shipping channels bisecting shallower areas. The landward end of Carquinez Strait immediately bifurcates at the western boundary of Suisun Bay, near the I-680 Bridge.

Previous studies in Carquinez Strait have identified gravitational circulation within Carquinez Strait, especially when the longitudinal salinity gradient is at a maximum. This helps sustain an ETM that forms at the eastern (landward) end of the strait, due to a sharp bathymetric change. This “sill”, which decreases the depth from 18 m to 11 m, forms a landward control on the gravitational circulation and therefore the ETM (Jay and Musiak, 1994; Schoellhamer, 2001). Deposition in Carquinez Strait may be greatest during neap tides when vertical mixing is minimized and the water column may become stratified. The following spring tides are then able to resuspend the erodible bed sediment and mix the water column. The presence of a bend within channels typically induces secondary circulation patterns. The combination of secondary circulation, density gradients, and bathymetric effects endow Carquinez Strait with a complex cross-sectional pattern of

SSC and water velocity (Ganju and Schoellhamer, 2006). Measurements of cross-sectional SSC are presented in the following chapter.

Suspended-sediment transport within Suisun Bay follows a seasonal cycle: the majority of suspended sediment is delivered through the Delta during the large, winter freshwater flows; a portion deposits in the Delta, while the remaining sediment is exported through Suisun Bay, to San Pablo Bay. During the following summer months reliable onshore winds generate wind-waves, resuspending bed sediments in both Suisun and San Pablo Bays. Due to the greater portion of shallows in San Pablo Bay, there is a gradient of SSC from west to east (between San Pablo and Suisun Bays), and with landward near-bed flows, these combine to transport sediment landward to Suisun Bay. As the summer progresses, the finer fraction of the erodible bed sediment pool is reduced. In the fall, when neither wind nor freshwater flow is significant, SSC is at its lowest. As the wet season commences during winter, the cycle repeats itself (Krone, 1979; Ganju and Schoellhamer, 2006).

Recent work has identified hydrodynamic and sediment transport features within Suisun Bay: Warner et al. (2004) detailed the presence of flood-tide pulses during low tides, which promote landward flux of sediment into Grizzly Bay. Ruhl and Schoellhamer (2004) demonstrated the importance of wind-wave resuspension and freshwater pulses on sediment concentrations in Grizzly and Honker Bays. These off-channel areas act as sediment storage after flow pulses, but are then more susceptible to wind-wave resuspension later in the spring.

6 Objective B: Calibration and application to tidal-timescale processes

6.1 Introduction

In this chapter, I detail the first step in the multiple-timescale calibration approach (Table 3.1): simulation of tidal-timescale features such as tidal stage, salinity, and estuarine turbidity dynamics. The model is calibrated to tidal stage, and validated to salinity dynamics within Suisun Bay. Bottom roughness will be varied to gain the best agreement. I then simulate the formation and lateral movement of the estuarine turbidity maximum, comparing the model results with field observations over several weeks. Much of this chapter first appeared in Ganju and Schoellhamer (in press(a)). In this section I do not calibrate the model to SSC, which is a typical calibration parameter for most tidal-timescale simulations (McDonald and Cheng, 1997; Lumborg and Pejrup, 2005). Calibration to SSC does not necessarily give confidence for simulating processes such as the ETM or gravitational circulation. Simulating the ETM and gravitational circulation are critical to simulating seasonal transport patterns, which can accumulate to modulate annual and decadal sediment transport patterns.

The estuarine turbidity maximum (ETM) is a feature common to many estuaries, where sediments of marine and/or terrestrial origin converge to locally increase turbidity. The importance of the ETM arises from its role in sedimentary and biological processes: local deposition is enhanced near the ETM (e.g. Grabemann et al., 1997; Woodruff et al., 2001; Ganju et al., 2004), while biological activity may be focused near the ETM as well (e.g. Kimmerer et al., 1998; Islam et al., 2005). The erosional/depositional nature of the local

sediment bed is known to affect benthic community composition (Aller and Stupakoff, 1996), therefore lateral gradients of deposition may create gradients in the benthos.

The mechanism of ETM formation varies depending on the geometry, tidal dynamics, and freshwater flow of an estuary. Some studies cite topographical effects (Jay and Musiak, 1994; Schoellhamer, 2001), tidal asymmetry (Sanford et al., 2001), and cyclical resuspension of temporarily deposited sediment (Grabemann et al., 1997; Ganju et al., 2004), to name a few. One notable study of lateral variability of the ETM was presented by Geyer et al. (1998), where frontal convergence of ebb waters over an asymmetric channel is an important mechanism; a pool of erodible material is preferentially deposited on one side of the estuary, resulting in ETM creation near that location.

The ETM can be thought of as a zone of locally increased turbidity, which has a distinct center of mass, longitudinally, laterally, and vertically. If one assumes that the ETM is longitudinally fixed, then the lateral and vertical variability in a cross-section can be evaluated by monitoring SSC at several points in the cross-section. The lateral and vertical location of this center over differing timescales provides insight into ETM formation and maintenance, and may potentially link with studies of biological activity, benthic community structure, and deposition patterns.

This study aims to calibrate the numerical model to tidal stage data, and validate with salinity data. Once the model is shown to suitably model hydrodynamic and salt transport processes, I will investigate the sediment transport features present in the model results.

If the model reproduces key features of the ETM, it is suitable for simulating tidal-timescale sediment transport processes. This is a first step towards then simulating annual and decadal timescale processes.

6.2 Field observations

6.2.1 Methods

6.2.1.1 Continuous monitoring

The U.S. Geological Survey established a continuous monitoring site on the north side of Carquinez Strait, on the I-680 Bridge in 1997 (site NBen; Fig. 6.1). This site consists of two conductivity, temperature, depth, and optical sensor multiprobes, at a near-bottom (lower) and a mid-depth (upper) elevation. For this study, a second site was established and maintained from March 24, 2004 to July 9, 2004 on the south side (site SBen), also on the I-680 Bridge. Optical sensors were deployed at the same vertical locations as the multiprobes at site NBen. The horizontal distance between sites NBen and SBen is 650 m, while the vertical distance between the upper and lower sensors is 15 m at both sites. Total width of the strait is 1200 m at this location. Fouling and debris interference can reduce data yield from optical sensors, therefore all sensors were cleaned and checked with known turbidity standards during site visits (typically once every three weeks). Water samples were collected to calibrate the optical sensor output to suspended-sediment concentration (SSC) (Buchanan and Ganju, 2005).

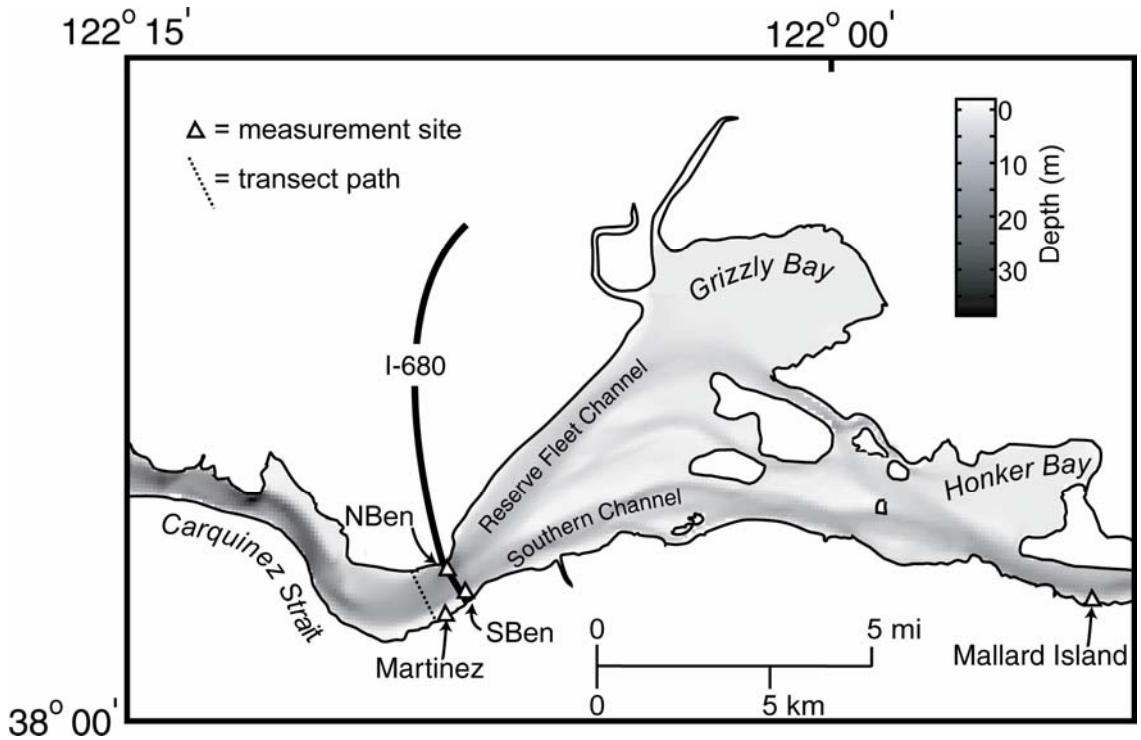

Figure 6.1 Suisun Bay, and locations of measurement sites.

Water velocity measurements were collected using upward-looking acoustic Doppler current profilers (ADCPs, 600 kHz broadband, RD Instruments), deployed on the bed 300 m seaward of the I-680 Bridge, from March 28, 2004 to July 7, 2004. Two units were deployed: one on the north side, and one on the south side. The units were programmed to sample at 10 min intervals, in 0.5 m vertical bins. Due to highly variable bathymetry seaward of the I-680 Bridge, the cross-section monitored by the ADCPs and the cross-section at the bridge are not identical, which hampers comparison of the two sets of data.

The four optical sensors deployed at the I-680 Bridge each conceptually occupy a quarter of the area between them, in the cross-section (Fig. 6.2). This ignores the variability within a quadrant or outside the area bounded by the four sensors, but the general trends in SSC should be reflected by these four sensors. After these assumptions, one can

compute a center of mass for the ETM by balancing the total mass laterally and vertically. It should be noted that the aspect ratio of Fig. 6.2 suggests that sensor SL occupies an isolated hole; when the cross-section is expanded to its actual proportions, it is clear that the use of sensor SL to represent that portion of the channel is justified.

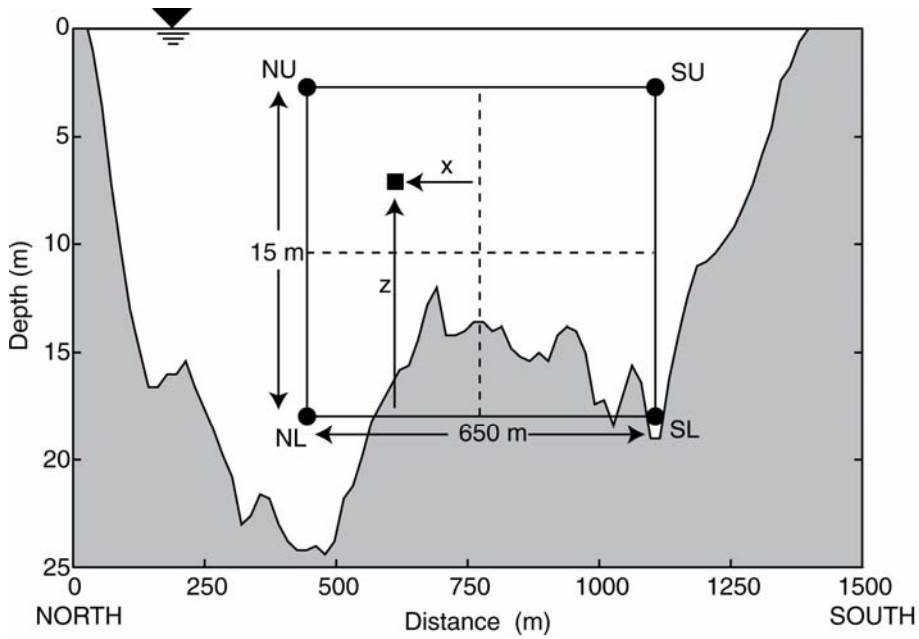

Figure 6.2 Cross-section of Carquinez Strait at I-680 Bridge. Four optical sensors were situated within the cross-section; upper and lower water column at site NBen (NU and NL respectively) and upper and lower water column at site SBen (SU and SL respectively). Square indicates an example of ETM center of mass, with x and y coordinate origins defined as shown. Depth is referenced to mean lower low water.

6.2.1.2 Tidal-cycle monitoring

Detailed measurements of SSC were undertaken to find the ETM center of mass. Cross-sectional measurements over one tidal cycle on July 7, 2004 coincided with a spring tide. Velocities were measured using a boat-mounted ADCP that traversed the 1200-m wide channel (1000 m seaward of the I-680 Bridge) every 10-15 min for 12 h. Conductivity, temperature, depth, and turbidity were measured using a Seabird SBE19plus profiling

package, deployed from a second vessel. The second vessel crossed Carquinez Strait every 30-45 min, profiling at 12 nodes in the cross-section. The package was lowered and raised at 1 m s^{-1}, sampling at 4 Hz. Therefore vertical sampling density was approximately 0.25 m. Water samples were collected with a Van Dorn sampler from the second vessel and analyzed for SSC. The corresponding turbidity output from the profiler at the nearest vertical location was related to the time of the water sample to generate a turbidity-SSC calibration curve. Turbidity output was then converted to SSC.

All profiling data were linearly interpolated spatially and temporally to the same transect path, vertical bins, and times of the ADCP measurements. Final interpolated grids were cross-checked with the original Seabird profiles to ensure that errors were not generated in the interpolation process. The center of mass in the cross-section for a given time was determined from the cross-sectional distribution of SSC.

6.2.2 Results

6.2.2.1 Continuous monitoring

Point SSC in the four quadrants was successfully measured for 28 days (Fig. 6.3). Inspection of the time-series reveals substantial lateral and vertical variability in SSC. At both sites, mean SSC at the lower sensor was over twice that of the upper sensor. On a tidal timescale, the water column was relatively well-mixed on strong tides, and vertical stratification was evident during neap tides. Laterally, SSC at site SBen peaked at the start of flood tide, while site NBen experienced peak SSC at the end of ebb tide (Fig. 6.4). Velocity data at site NBen was obtained for the entirety of the record, while the

instrument at site SBen was tipped over on May 30, 2004, leading to a loss of the data for the remainder of the deployment. Velocity data at both sites show increased gravitational circulation during neap tides.

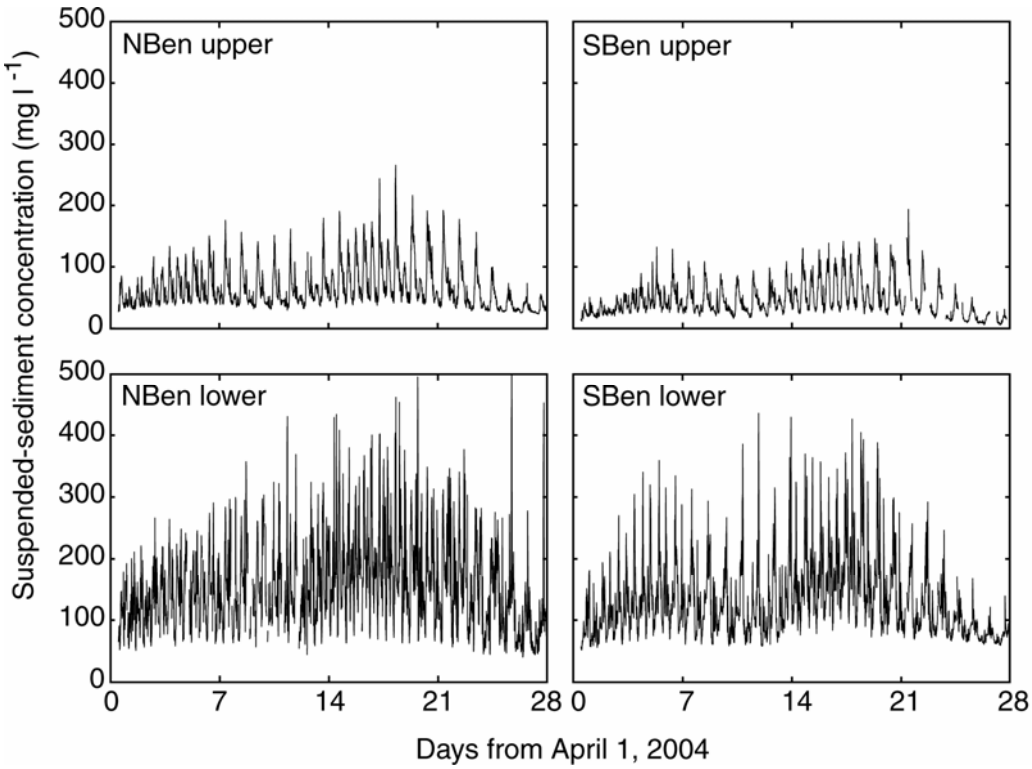

Figure 6.3 Time-series of SSC from four optical sensors at cross-section in Carquinez Strait: upper sensor at site NBen; lower sensor at site SBen; upper sensor at site SBen; and lower sensor at site SBen.

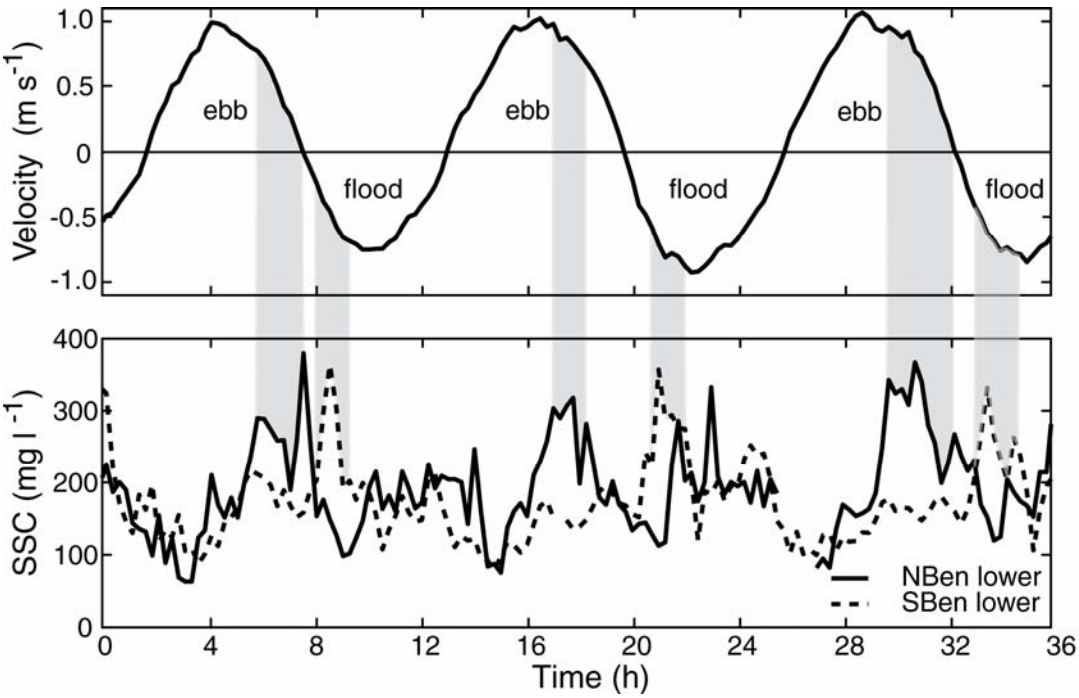

Figure 6.4 Time-series of mean velocity in Carquinez Strait and SSC from lower sensors at sites NBen (solid) and SBen (dashed). SSC at SBen is typically maximum at the start of flood, while SSC at NBen is maximized at the end of ebb.

Results from the center of mass calculations demonstrate large variability in lateral and vertical position on the tidal timescale (Fig. 6.5). The center of mass calculation results in a northerly position when SSC is greatest on the north side, and vice-versa. The northern-most position on the tidal timescale was 125 m north of center, while the southern-most position was 100 m south of center. On a tidally averaged basis, these fluctuations are reduced to 40 m north of center (northern-most) and 8 m north of center (southern-most). The maximum tidally averaged north position occurs during a neap tide, while the maximum southern position occurs during a spring tide. Vertically, the maximum and minimum instantaneous vertical positions were 7 and 4 m above the lower sensors, respectively, while the tidally averaged maximum and minimum positions were 5.5 and 4.75 m respectively.

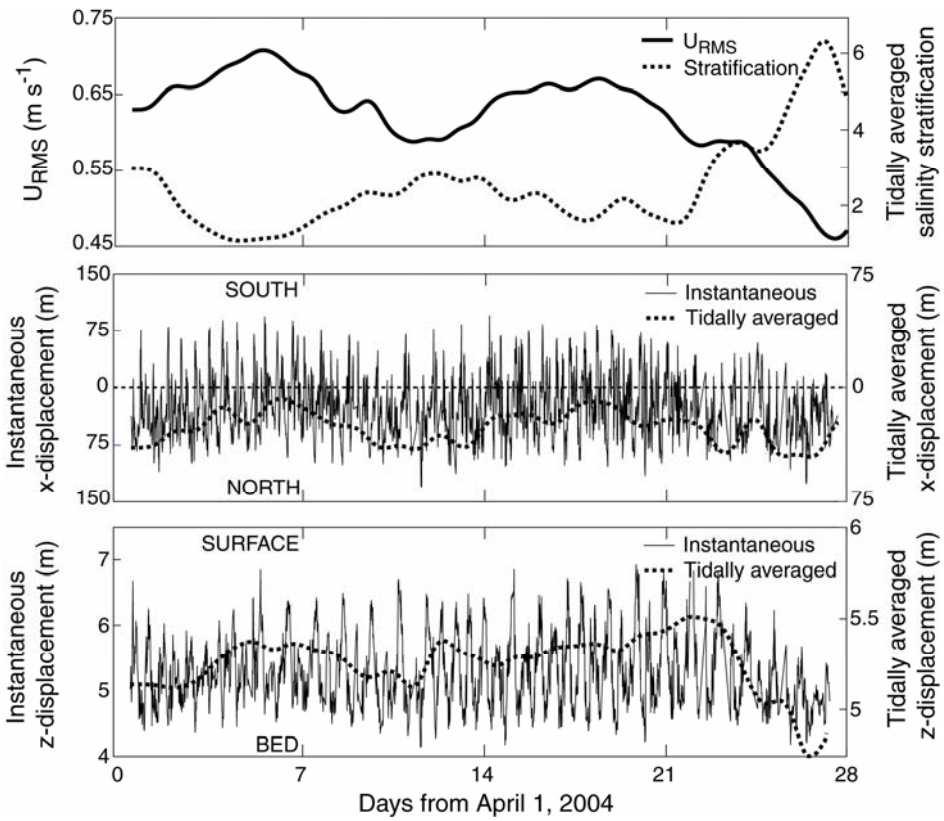

Figure 6.5 Time-series of U_{rms} (measure of tidal energy) and tidally averaged stratification in Carquinez Strait; x-displacement of the ETM center of mass; and z-displacement of the ETM center of mass. Center of mass favors the north side and lower water column on neap tides during periods of reduced tidal energy, and migrates toward the south side and upper water column on spring tides during periods of increased tidal energy.

6.2.2.2 Tidal-cycle monitoring

The tidal-cycle, cross-sectional measurements validate the large lateral and vertical variability observed in the time-series of point SSC. On early ebb tide, velocity in the northern half of the channel led by 30 min over the southern half, which was still slightly flooding. As the entire channel turned to ebb, SSC was greatest on the north side of the channel (SSC>300 mg l^{-1}), leading to a northerly ETM center of mass (Fig. 6.6, circles 1,2,3). The transition from ebb to flood was characterized by greater SSC on the south side and in the lower water column (SSC >1000 mg l^{-1}), leading to a center of mass that

moved southward (Fig. 6.6, circles 4, 5). As flood tide progressed, the center of mass moved towards the center of the channel, but back southward at maximum flood tide (Fig. 6.6, circle 7). Over this 12 h period, the center of mass varied 250 m laterally and 5 m vertically. Maximum northern position occurred on maximum ebb tide, while maximum southern position occurred at slack after ebb. The minimum vertical position occurred on slack tides due to deposition, while maximum vertical position occurred during maximum velocities.

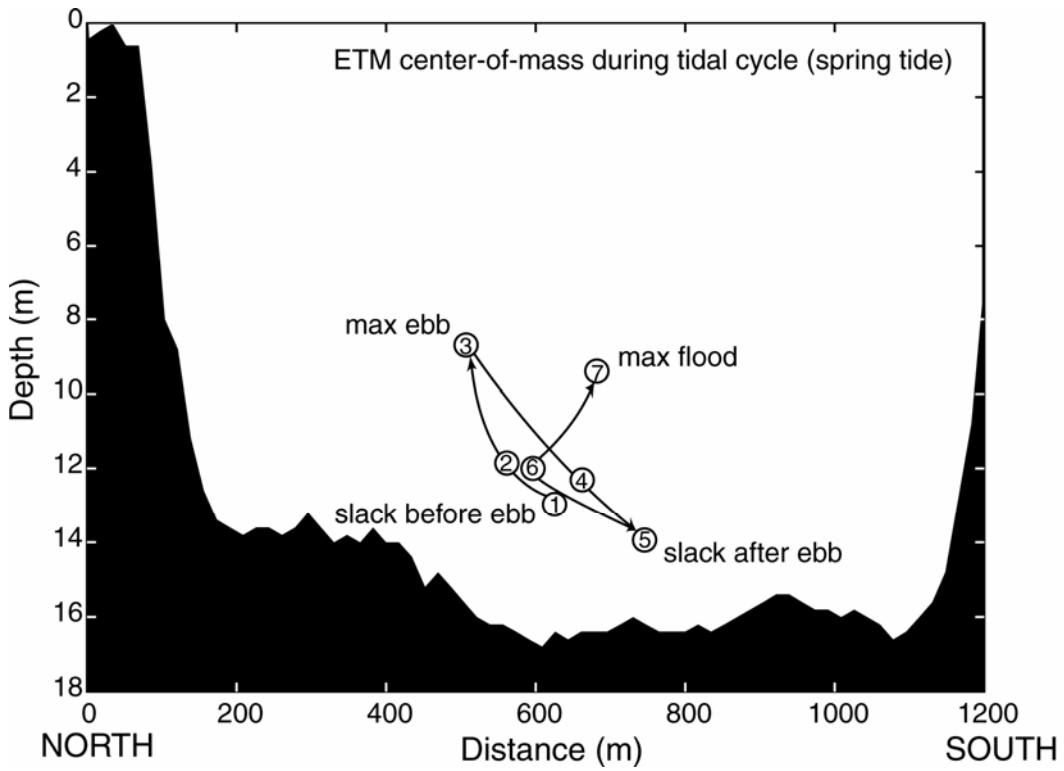

Figure 6.6 Movement of ETM center of mass between slack before ebb to max flood, obtained by water column profiling of SSC in the transect seaward of the I-680 Bridge. Center of mass begins at circle marked 1 at slack before ebb, migrates to 3 at maximum ebb, 5 at slack after ebb, and 7 at maximum flood tide. Depth is referenced to mean lower low water.

The highly variable bathymetry of the Strait seaward of the I-680 Bridge precludes direct comparison of the data from the three cross-sections (i.e. the I-680 Bridge, the ADCP-

occupied cross-section, and the tidal-cycle profiling transect). The I-680 Bridge cross-section (Fig. 6.2) shows the north side as the deeper side, whereas the tidal-cycle monitoring cross-section (Fig. 6.6) shows the south side as the deeper side. The deeper section runs across the Strait in this fashion, and therefore it is difficult to articulate the dynamics between the three cross-sections.

6.3 Modeling simulations

While the mechanism of vertical ETM displacement is increased tidal energy (which leads to enhanced vertical mixing), the mechanism for lateral ETM displacement is not obvious from the observations. Lateral displacement is linked with tidal energy, and this may be due to secondary circulation, vertical dynamics, or local variations in bed storage of sediment. Deciphering the dominant mechanisms may be accomplished with a three-dimensional hydrodynamic/sediment transport model. These data also provide an opportunity to calibrate and validate the 3D model to tidal-timescale processes. Final model parameters, some of which were used for calibration, are given in Table 6.1. Initial values were based on previous modeling work in San Francisco Bay (McDonald and Cheng, 1997; FAA, 2003).

Table 6.1 Model parameters and values for tidal-timescale simulations. Values with an asterisk were used as calibration parameters.

Model parameter	Value
# of x-direction cells, size range	160, 72 – 394 m
# of y-direction cells, size range	87, 102 – 593 m
# of z-direction cells	8
bottom roughness*	0.004 m
baroclinic time step	40 s
barotropic time step	2 s
simulation steps	65700
settling velocity	0.10 mm s^{-1}
erosion rate	$2x10^{-5}$ kg m^{-2} s^{-1}
critical stresses	0.05 N m^{-2}
porosity	0.90
bed density	1000 kg m^{-3}
bed thickness	1.0 m
tidal boundary velocity, stage	Flather (radiation)
river boundary velocity, stage	Flather (radiation)
tidal boundary tracers	clamped
river boundary tracers	clamped

6.3.1 Methods

6.3.1.1 Modeling domain

The modeling domain of Suisun Bay is constrained between Carquinez Strait on the west and the Delta on the east (Fig. 6.7). The domain was discretized into a 160 x 87 x 8 cell domain (in the west-east, north-south, and vertical directions respectively). The geometric complexity of the Delta presents a modeling challenge: the sinuous network of channels and flooded islands requires substantial computational effort and bathymetric data. Simplification was accomplished by representing the Delta as a uniform channel. This “pseudo-Delta” was extended 80 km, which is the greater than the length of the tidal Sacramento River. The area of the pseudo-Delta is equal to the open water area of the actual Delta. This idealization not only reduces computational effort, but it allows for simplified landward boundary conditions. While this may introduce unrealistic conditions

within the Delta, the goal is to represent conditions within Suisun Bay (and Carquinez Strait) adequately. If hydrodynamic and salinity conditions in Suisun Bay are modeled adequately, then the sediment dynamics should be unaffected by the simplification of the Delta.

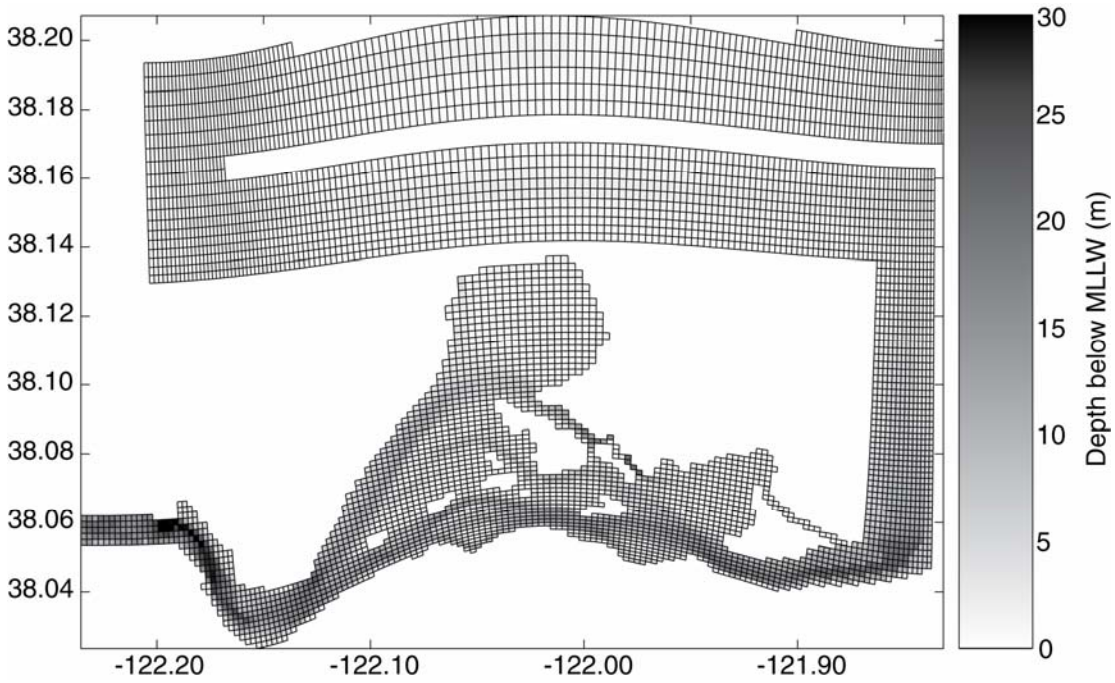

Figure 6.7 Computational grid of Suisun Bay, in ROMS orthogonal, curvilinear format. Depth is referenced to mean lower low water. Masked land cells are not shown.

6.3.1.2 Boundary conditions

6.3.1.2.1 Landward boundary conditions: freshwater flow, salinity, SSC

Extending the pseudo-Delta to Freeport allows for the application of a unidirectional transport boundary condition. The net transport, in the seaward direction, was obtained from Dayflow model output (California Department of Water Resources, 2005). Dayflow is an idealized representation of freshwater flow out of the Delta, that accounts for water exports and diversions within the Delta. I apply the net outflow at Mallard Island to the landward end of the domain. The boundary condition imposed on the landward end

allows for the tide to freely propagate out of the domain, yet maintains a prescribed freshwater transport. Salinity is zero on the eastern boundary as salt intrusion has not been observed at Freeport in the modern era of controlled flows.

Daily SSC data are available at Freeport from the U.S. Geological Survey. SSC in the San Joaquin River are assumed to be equivalent to the Sacramento River. Flow magnitude in the San Joaquin River is typically 20% of the Sacramento River flow magnitude, so this simplification is relatively minor.

6.3.1.2.2 Seaward boundary conditions: tidal flow, salinity, SSC

Tide levels from the California Department of Water Resources Martinez station (Fig. 6.1) were used at the seaward boundary, by shifting and amplifying using tidal predictions by the National Ocean Service (0.5 hours earlier for tidal elevation, amplified by a factor of 1.1). This is preferred to using predictions for the area near the western boundary alone; the record from the Martinez station retains sub-tidal fluctuations in water level due to atmospheric forcing (e.g. wind, pressure). As an option, ROMS calculates tidal velocities based on the tidal stage time-series. For salinity, the method of Warner et al. (2005a) can be used. This is an analytical function based on near-bottom longitudinal salinity profiles as follows:

$$S(X) = \frac{S_0}{2}\left[1 + \tanh\left(\alpha - \frac{X}{\beta}\right)\right] \tag{6.1}$$

where S is the salinity, X is the longitudinal coordinate with origin at the mouth of the estuary, S_0 is the seaward boundary value of salinity (held at 30, due to tidal variability), and α, β are empirical parameters. Parameter α is held constant as 2 following Warner et al. (2005a). The parameter β is related to freshwater flow (Q); for a given estuary this relationship can be established and used in the analytic expression. Data from 358 longitudinal cruises of the *R/V Polaris* (http://sfbay.wr.usgs.gov/access/wqdata) were processed to determine this relationship as follows

$$\beta = \exp[4.25 - 0.22 \log Q] \tag{6.2}$$

The model then uses the derivative of Eq. 6.1 to determine the local salinity gradient. The salinity at the open boundary is computed with the local salinity gradient value and the first interior salinity value. The model was initialized with a longitudinal salinity distribution based on observations to accelerate convergence. The initial vertical salinity distribution is uniform.

The western SSC condition was specified as the velocity-weighted SSC at the I-680 Bridge. This value was computed and estimated using SSC measured at the four sensors mounted on the I-680 Bridge (Ganju and Schoellhamer, 2006). The model code for this simulation was modified to compute the flood-tide velocity at the boundary, distribute the flood-tide SSC in a Rouse profile (Rouse, 1937), and ensure that the final velocity and SSC product matches the value estimated at I-680 Bridge (see Section 7.2.2.2). This assumes negligible erosion and deposition within Carquinez Strait.

6.3.1.3 Calibration and validation

Calibrating to stage at the western and eastern ends of Suisun Bay (Martinez and Mallard Island, respectively, Fig. 2) was deemed a sufficient calibration goal for these simulations. The bottom roughness was varied to achieve the optimum agreement between observations of tidal stage and model simulations. Observations of stage were available from the California Department of Water Resources for gages situated at Martinez and Mallard Island, though data were sparse between April 1 and April 28, 2004. Calibration results are extended to May 4, 2004, to yield an adequate comparison. Calibration to sediment data are not necessary, as I wish to qualitatively identify the ETM movement mechanisms, which should be independent of sediment concentration.

Validation will be evaluated with regards to vertical and longitudinal salinity gradients. The dynamics of salinity are known to be critical for sediment transport within Suisun Bay and Carquinez Strait. Both longitudinal and vertical salinity gradients can alter the sediment transport direction and magnitude. The longitudinal gradient is defined as the difference in near-bottom salinity between site NBen and Mallard Island, while the vertical stratification is defined as the difference between near-bottom and mid-depth salinity at site NBen.

6.3.1.4 Center of mass calculation

ROMS uses a stretched vertical and curvilinear horizontal coordinate, therefore the mass of sediment in each cell was computed and applied at the center of each cell. The center of mass was then determined.

6.3.2 Results

6.3.2.1 Calibration and validation

Calibration to stage was accomplished with an r^2 above 0.99 at both Mallard Island and Martinez (Fig. 6.8), by modifying the bottom roughness in the log-drag stress formulation to z_o=0.004 m (Warner et al., in press). The time-series of vertical salinity structure (Fig. 6.9) showed a satisfactory pattern of greater stratification on neap tides, and increased mixing on spring tides, though the model results deviate from observations. Similarly, the tidal variability and relative amplitude of the longitudinal salinity gradient are in agreement with observations, but the absolute values are not modeled well (Fig. 6.9). The instantaneous time-series of salinity dynamics are not as well-matched to observations as water level; this is most likely due to the salinity boundary condition which is solved as a function of freshwater flow. The use of this function is justified, however, due to limited salinity data at the western boundary; in addition, later modeling efforts will require historical boundary conditions (when flow data were available but salinity data were not).

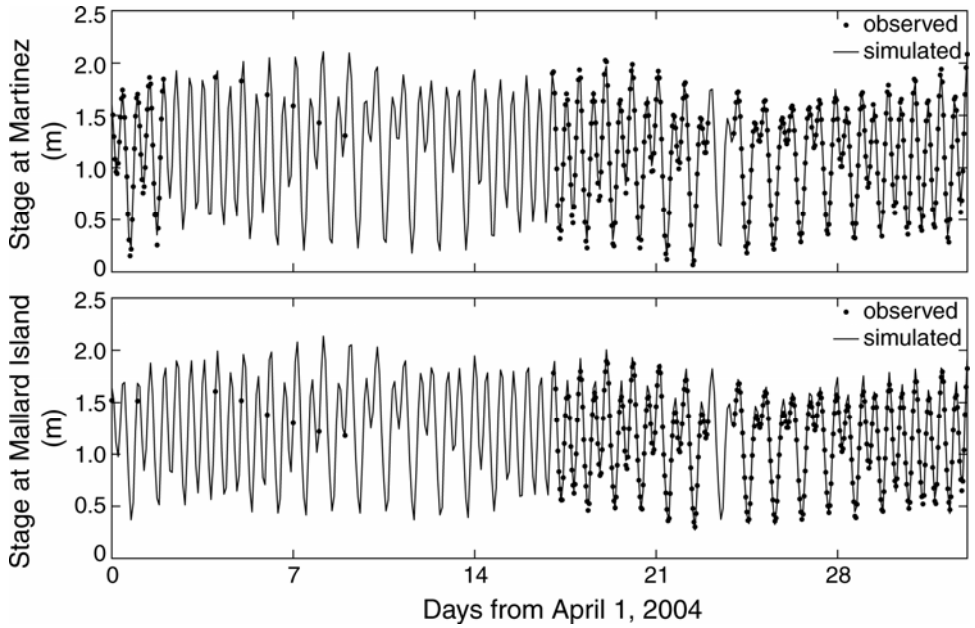

Figure 6.8 Model calibration to stage at Martinez and Mallard Island. The two sites represent the seaward (Martinez) and landward (Mallard Island) ends of Suisun Bay. Stage is referenced to mean lower low water.

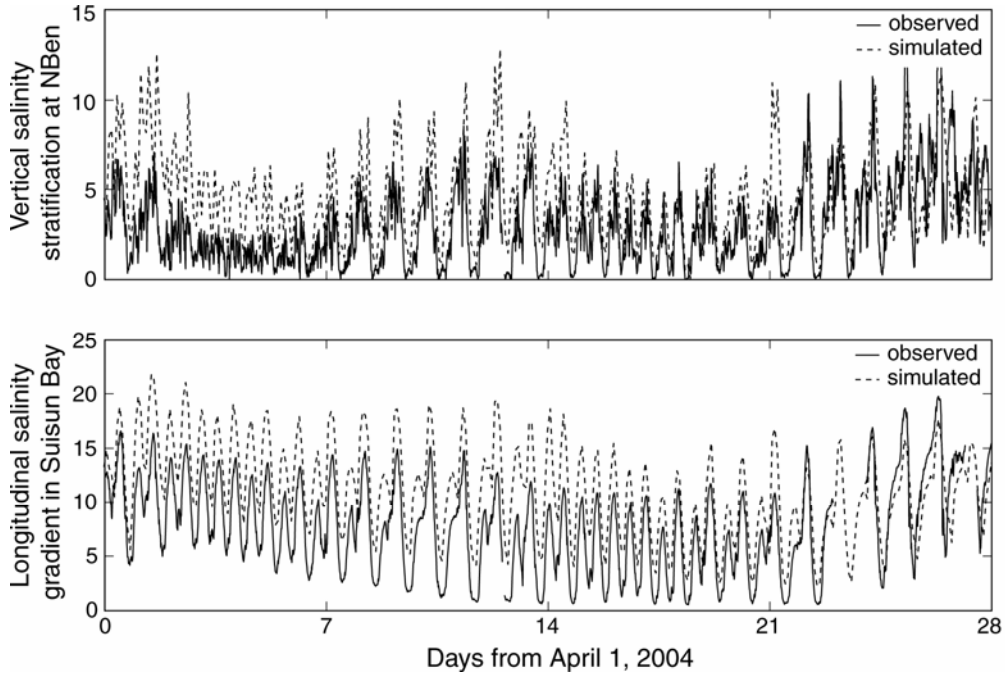

Figure 6.9 Model validation to vertical salinity stratification at site NBen and longitudinal salinity gradient between site NBen and Mallard Island.

6.3.2.2 Center of mass calculation

The model recreated a local ETM, due to near-bed convergence of flow near the topographical control. The center of mass of the entire ETM varied in response to tidal energy and vertical stratification in the same manner as the observations (Fig. 6.10). Reduced tidal energy led to increased vertical stratification, and a northerly ETM position (Fig. 6.10). Increased energy and reduced stratification displaced the ETM position to the south. Instantaneous displacements were as large as 200 m in the lateral and 4 m in the vertical, while tidally averaged displacements ranged from 50 m to 1 m in the lateral and vertical, respectively. These displacements are in agreement with the observed displacements, despite the limitations of the four sensor method (i.e. incomplete representation of entire cross-section). I do not compare the absolute values of the field and modeling observations, as the coordinate system origins and domains are not congruent.

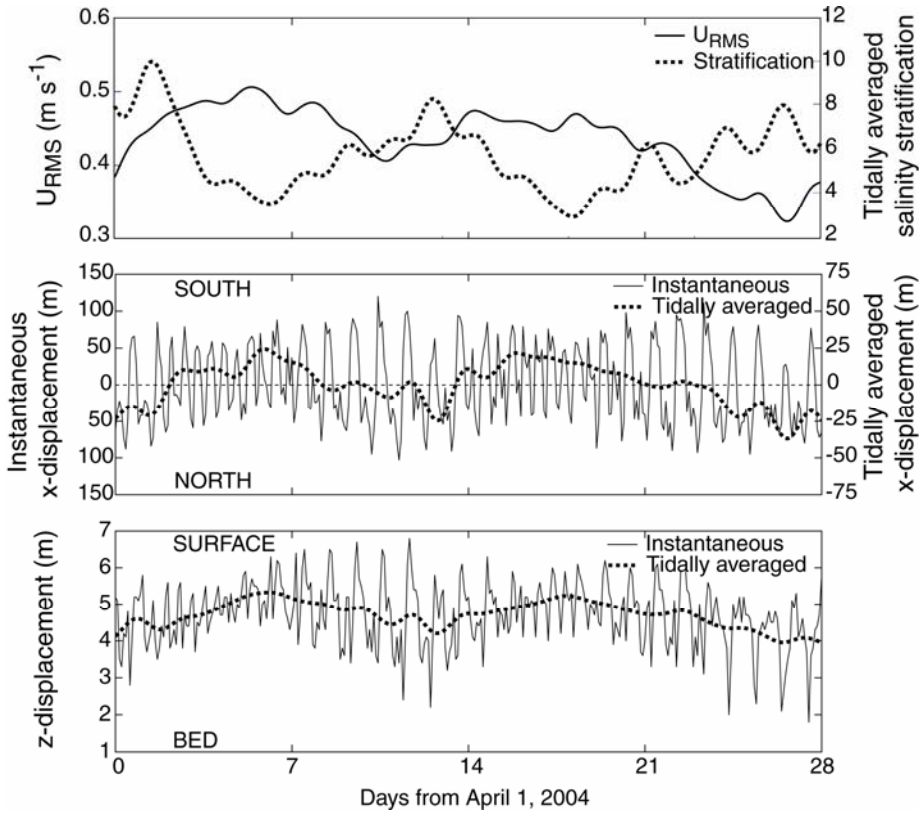

Figure 6.10 Model results of U_{rms} and tidally averaged stratification; x-displacement of the ETM center of mass; and z-displacement of the ETM center of mass. In agreement with field observations, center of mass favors the north side and lower water column on neap tides during periods of reduced tidal energy, and the south side and upper water column on spring tides during periods of increased tidal energy.

6.4 Discussion

6.4.1 Laterally averaged conceptual models of ETMs

The existing conceptual model of the ETM in Carquinez Strait (Schoellhamer and Burau, 1998) stresses the importance of topography in controlling gravitational circulation. A topographical control that restricts gravitational circulation allows for the trapping of particles near the bed. During neap tides, persistent stratification inhibits vertical mixing, and the vertical gradient of SSC is maximized.

In a 2D laterally averaged sense, two conceptual models are applicable to Carquinez Strait. The north side, with an abrupt bathymetric change from 18 m to 11 m, follows the Schoellhamer and Burau (1998) conceptual model for ETM formation. When the south side is considered, it is clear that the lack of a topographical control does not promote local particle trapping. Therefore the cross-section behaves as a combination of two separate 2D conceptual models: one with a topographical control, one without. The transition between spring and neap tides leads to an analogous transition for ETM position. Gravitational circulation, stratification, and particle trapping are enhanced on the north side during neap tides, displacing the ETM to the north, while a reduction in the strength of these mechanisms during spring tides displaces the ETM towards the south.

6.4.2 Simulation and comparison with conceptual models

The simulation results reflect this conceptual model in a 2D vertically averaged sense. The product of mean surface (u_s) and near-bottom (u_b) residual currents yields an estimate of gravitational circulation strength (Fig. 6.11). When the product is large and negative, this indicates strengthened gravitational circulation; a near-zero or positive product indicates a lack of gravitational circulation. On neap tides the strength is increased west of the topographical control, yet abruptly decreases eastward on the north side while gradually decreasing eastward on the south side. This indicates the trapping mechanism on the north side, seaward of the topographical control. The change in gravitational circulation strength from spring to neap (Fig. 6.11) shows a greater increase in strength (more negative) in the north as opposed to the south (at the I-680 Bridge

transect). On the south side, strength is increased landward and seaward of the I-680 Bridge, therefore particles are not trapped in this region.

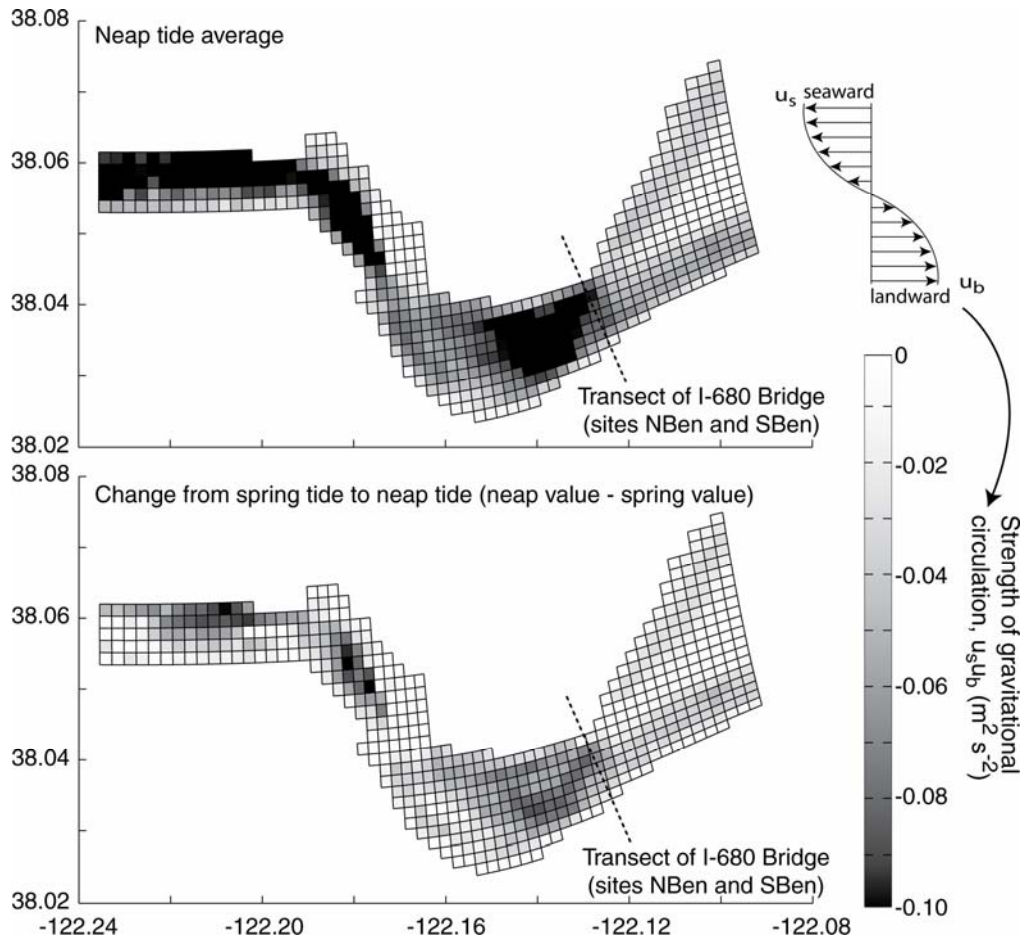

Figure 6.11 Model surface plot of strength of gravitational circulation on neap tide and change in strength from spring tide to neap tide. Increasingly negative values indicate larger negative product of surface and bottom velocities, and therefore stronger gravitational circulation.

Secondary currents in Carquinez Strait are evident in ADCP data from both the boat and bottom-mounted units. The configuration of Carquinez Strait, with a prominent bend and variable topography, promotes secondary circulation on both spring and neap tides. Simulation results (Fig. 6.12) show strengthening of this circulation during spring tides,

due to higher tidal velocities. A prominent counter-clockwise gyre between sites NBen and SBen is active on spring tides and weakened on neap tides. This gyre delivers near-bed water from the northwest to the southeast, and a complementary transferal of surface waters from southeast to northwest. Particle trapping on the north side during neap tides is suggested by previous work (Schoellhamer and Burau, 1998) and the work presented here. Therefore there is a temporary storage of sediment on the bed of the north side, during neap tides. The ensuing spring tide transports sediment from this temporary deposit and secondary circulation tends to deflect sediment-rich, near-bed water to the southeast, displacing the ETM center of mass southward.

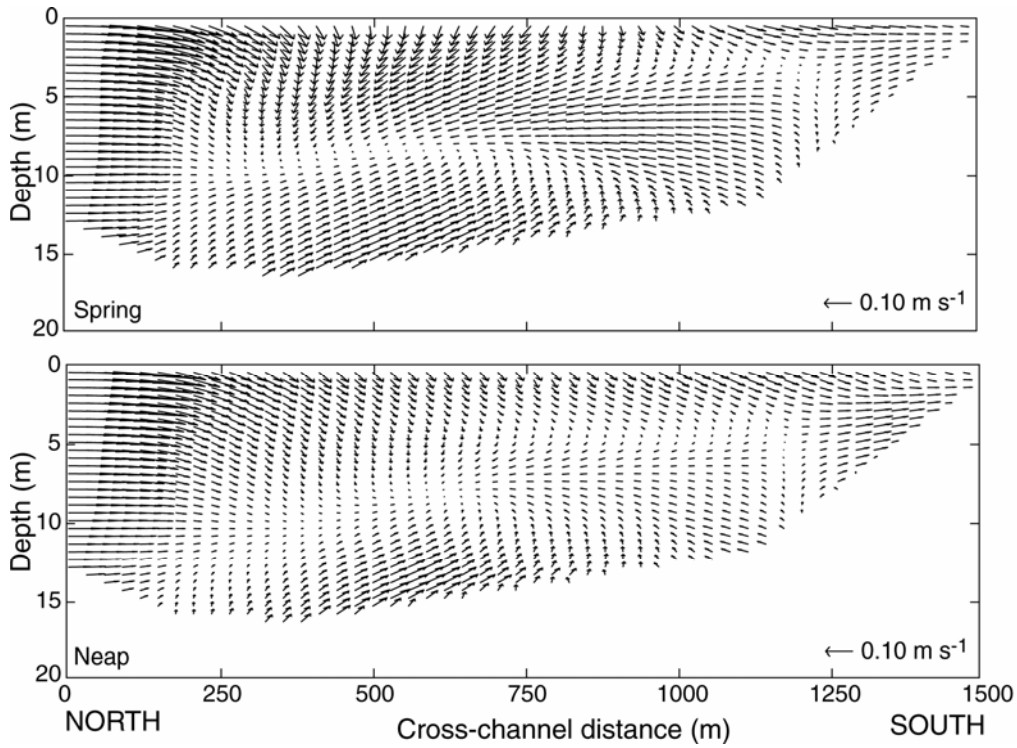

Figure 6.12 Modeled cross-channel and vertical velocity vectors on spring tide and neap tide. Lateral and vertical circulation are enhanced on spring tide, with near-bed velocities on the north side directed southward. Depth is referenced to mean lower low water.

6.5 Conclusions

Simulating tidal-timescale sediment transport in estuaries usually focuses on SSC alone, with little focus on critical transport features. For the ultimate goal of simulating decadal-timescale processes, I need confidence in the sediment transport features produced by the model, at all timescales. Calibration to tidal stage, and validation to tidal salinity dynamics is accomplished by adjusting the bottom roughness. Once this step is completed, I investigated the dynamics of the estuarine turbidity maximum. This key feature in Suisun Bay is reproduced by the model: particle trapping at the topographical control is modeled, as is the lateral movement of the ETM center of mass.

The center of mass moves coherently in response to tidal energy, stratification, and gravitational circulation. Field and modeling observations indicate that the lateral position can change by as much as 250 m in a 1200 m channel on the tidal timescale (20% of width), and 50 m on a tidally averaged basis. Vertical position expectedly responds to vertical mixing, with position varying by 5 m on the tidal timescale (17% of depth) and 1 m on the tidally averaged timescale. Gravitational circulation and bathymetry clearly affect the movement and trapping of particles, modulating the center of mass of the ETM. Secondary circulation in the channel distributes sediment on energetic tides, also displacing the center of mass. When combined, these mechanisms are all responsible for the lateral movement of the ETM, in a relatively narrow and energetic tidal strait.

The ROMS model, developed and applied for this simulation, successfully captures the tidal-timescale features responsible for ETM formation. Confidence in the tidal-timescale representation of the model is provided because of this application. The next step is applying the model to annual-timescale processes.

7 Objective C: Calibration and application to annual-timescale processes

7.1 Introduction

Simulation of annual-timescale processes requires data over extensive periods; Ganju and Schoellhamer (2006) provide a set of sediment flux data at the seaward end of Suisun Bay, which can be combined with the data of McKee et al. (2006), at the landward end, to obtain a sediment budget for Suisun Bay. Here, I use a subset of that data for calibration and a subset for validation. Major parameters varied will be sediment characteristics, wave period, and Delta configuration. It is important to note that the last chapter did not use wind-wave forcing; this feature is implemented here due to its importance on the annual-timescale. The final product will be a model suitable for estimating annual-timescale sediment supply, under modern conditions, to Suisun Bay.

Sediment supply to a subembayment of an estuary is determined by watershed sediment input and the sediment exchange with adjacent embayments. Sediment supply is a critical variable for investigations of habitat stability, restoration potential, and contaminant fate/transport. Suspended sediment is needed to create and sustain valuable estuarine habitats such as tidal wetlands (Pont et al., 2002; Reed, 2002; Temmerman et al., 2003; Zedler and Callaway, 2001), though sediment-associated contaminants can also accumulate wherever sediment preferentially deposits (Arzayus et al., 2002; Hornberger et al., 1999; Taylor et al., 2004). In addition, nutrients and biota accumulate near estuarine turbidity maxima (ETM), where high suspended-sediment and contaminant concentrations are found (Peterson et al., 1975; Jassby and Powell, 1994). Enhanced

biological activity in these areas may increase contaminant uptake by the food web (Kimmerer et al., 1998).

These issues converge in Suisun Bay, California (Figs. 1.1, 1.2, 6.1). Over 90% of marsh area has been lost in San Francisco Bay since the 19th century, and current management goals in Suisun Bay include marsh restoration. Deposited sediment in Suisun Bay is thought to be high in mercury concentrations due to 19th century gold mining in the watershed (Hornberger et al., 1999), leading to concerns about resuspension of these deposits over long timescales (>10 y). Jaffe et al. (1998) show net erosion in Suisun Bay since the first bathymetric surveys in the 19th century. The net sediment budget of Suisun Bay in the current era may shed light on the viability of habitat restoration as well as the magnitude of mercury introduction to the water column. In order to quantify this sediment budget, sediment flux at the landward and seaward boundaries of the subembayment must be determined.

Estimating sediment flux in estuaries can be complicated by the large range of tidal and riverine forcing. Spring and neap tides combined with periods of varying freshwater flow can introduce lateral and vertical variability of suspended-sediment concentrations (SSC) and water velocity. The variations can be induced by salinity gradients, bathymetric forcing, and secondary circulation (Ridd et al., 1998; Blanton et al., 2003). Suisun Bay, as the landward-most subembayment of San Francisco Bay, is subject to variable freshwater flow as well as semi-diurnal tides.

Proper estimation of suspended-sediment flux through Carquinez Strait must account for the entire cross-section. While monitoring a large cross-section is both physically and financially impossible over the necessary timeframes, it may be possible to identify surrogate data that can be continuously monitored. In this study I occupied portions of the channel with autonomous equipment for three months, and calibrated those data to tidal-cycle cross-sectional measurements. The results from the three-month deployment were extrapolated to quantify fluxes over water years 1997, 1998, 2002, 2003, and 2004. These data, combined with the landward boundary fluxes of McKee et al. (2006), provide unique annual-timescale data for model calibration.

Modeling estuarine sediment transport with a tidal-timescale model typically involves calibrating to the following hierarchy of data: tidal stage, velocity, salinity, suspended-sediment concentration (e.g., McDonald and Cheng, 1997; Lumborg and Pejrup, 2005). Prior efforts in geomorphic (or boundary flux) modeling of estuaries have used these tidal-timescale models calibrated to tidal heights, velocities, and suspended-sediment concentration to model bed evolution. Lumborg and Pejrup (2005) predict net fluxes over one year using a 20 d time-series of SSC as the validation parameter. Schoellhamer et al. (in press), however, show that calibration to these parameters does not guarantee accuracy in terms of modeling geomorphic evolution. Uncertainty in input parameters can cause bed evolution to adjust in response to these erroneous parameters; this adjustment will not recognized as a “spin-up” effect, and the simulation of geomorphic evolution will be compromised. For example, Schoellhamer et al. (in press) show that a

10% error in tidal velocity can cause a bed adjustment that requires 10 years to equilibrate.

Some recent efforts to predict morphological development have used more robust approaches: Douillet et al. (2001) adjusted parameters in order to obtain best qualitative agreement between observations of percent mud on the seabed and simulated deposition; Ouillon et al. (2004) further calibrated the Douillet model using satellite-derived estimates of SSC. This two-step approach provides greater confidence than a single-step approach. Hibma et al. (2003) developed an approach for long-term geomorphic modeling, evaluating the results by comparing the development of morphological features within the model to measured morphological features from two estuaries. The lesson from prior and current efforts is clear: a model must be calibrated and validated to the type of data that will be the final product of the modeling effort.

Two types of data provide the most robust calibration information: frequent bathymetric surveys, and continuous cross-sectional sediment flux data. The former gives a snapshot of bathymetric change between survey dates, though the expense and difficulty of these surveys results in large temporal spacing between surveys (~ 10 y). This temporal spacing is adequate for decadal-scale geomorphic modeling, but the actual seasonal and year-to-year mechanics of the sediment transport cannot be verified. In this regard, continuous cross-sectional sediment flux data satisfies multiple goals. The net sediment budget will be correct if the fluxes are modeled correctly: inputs and outputs must balance with the change in sediment storage, and the tidal and subtidal timescales of

sediment transport can be modeled and evaluated. However, the spatial variability of erosion and deposition cannot be evaluated. Data of these types are necessary to ensure that parameter specification is not causing bathymetric spin-up errors.

The two aforementioned data types are available for Suisun Bay, California, though the temporal coverage does not overlap. Five bathymetric surveys were performed in Suisun Bay, spanning from 1867 to 1990 (Cappiella et al., 1999; Fig. 1.3). These data show the influence of hydraulic mining on sediment deposition (1867-1887), while the subsequent reduction of mining debris and reduced freshwater flows (1922-1942) results in net erosion. It would be possible to calibrate a model to these data alone, though the seasonal and year-to-year sediment transport mechanics could not be evaluated. An additional data set of cross-sectional sediment flux data, however, are available at the landward and seaward boundaries of Suisun Bay, Mallard Island and Carquinez Strait, respectively. These data are available for water years 1997-1998, and 2002-2004. McKee et al. (2006) estimated advective and dispersive loads between the Sacramento/San Joaquin Delta and Suisun Bay at Mallard Island, using continuous suspended-sediment concentration (SSC) data and freshwater flow measurements. Ganju and Schoellhamer (2006) developed estimates of advective, dispersive, and Stokes drift flux between Suisun Bay and Carquinez Strait, based on surrogate measurements of SSC, longitudinal salinity gradient, and freshwater flow. The data for both boundaries overlap for five water years which span extremes of freshwater flow and sediment load.

These data are used to calibrate and validate the geomorphic model, while the bathymetric data can be used for subsequent hindcasting simulations. In Chapter 6, I established some basic parameters for a successful simulation of tidal-timescale sediment transport; here I adjust those parameters as needed to simulate annual sediment fluxes.

7.2 Field observations

7.2.1 Methods

7.2.1.1 Spring monitoring period

Details of the continuous monitoring during this period are given in Section 6.2.1.1.

7.2.1.2 Tidal-cycle cross-sectional measurements

Ideally, the true velocity-weighted SSC can be represented by some combination of the SSC values in the four quadrants. Velocity-weighted SSC in a cross-section is calculated as

$$SSC_u = \frac{\int uC\,dA}{\int u\,dA} \tag{7.1}$$

where A is channel area, u and C are velocity and suspended-sediment concentration, respectively, and

$$u = [u] + u' \tag{7.2}$$

$$C = [C] + C' \tag{7.3}$$

Brackets indicate a spatial average value and the prime indicates the spatially fluctuating portion. Equations 7.2 and 7.3 refer to spatial measurements in the cross-section. If only the spatial average SSC was used (without velocity weighting), the result would ignore the contribution of the non-zero product of $u'C'$ (spatial correlation between velocity and concentration fluctuations). The product of SSC_u and total water discharge (denominator of Eq. 7.1) gives total instantaneous sediment flux. Conceptually, if the SSC was not velocity-weighted, then the flux contribution of stagnant water parcels with high SSC would be overestimated, while swift-moving parcels with low SSC would be underestimated.

Weights for each of the four quadrants are required because the relative contribution of each quadrant to SSC_u is unknown. Calibration of weights can be accomplished by performing cross-sectional surveys of velocity and SSC. SSC_u can be regressed against the quadrant SSC values, to infer the proper weights for each quadrant. Because these data are time and labor-intensive, they can usually be obtained over short time-frames (< 30 h). It was determined that tidal-cycle surveys during a spring and neap tide would be sufficient to characterize variability.

Detailed measurements of velocity and SSC were undertaken to estimate SSC_u as described in Section 6.2.1.2. Each velocity measurement has a corresponding interpolated SSC value, and SSC_u may be calculated using Eq. 7.1.

7.2.1.3 Total channel discharge

Total channel discharge for the spring monitoring period was computed via the index-velocity method (Simpson and Bland, 2000). This requires a continuous surrogate for channel-average velocity, namely the index velocity. The bottom-mounted north channel ADCP provided the index velocity (depth-averaged velocity). Ideally, both bottom-mounted ADCPs would be considered, but the south channel ADCP data were corrupted and unusable after the unit was tipped over (May 30, 2004). The index-velocity is calibrated to the channel-average velocity obtained during the tidal-cycle measurements, to provide a rating curve. This curve is then applied to the continuous index velocity measurements, generating a full time-series of channel-average velocity. Cross-sectional area is computed using the geometry of the cross-section (provided by ADCP measurements), and a stage-area relationship. Continuous stage was measured by the California Department of Water Resources at Martinez. Continuous, instantaneous discharge is calculated as the product of channel-average velocity (obtained for the index-velocity rating) and cross-sectional area (via the stage-area relationship).

7.2.1.4 Residual suspended-sediment flux calculation

The decomposition of the total constituent flux is given by Dyer (1974). Lateral and vertical variations of SSC in the channel can be ignored because SSC_u is assumed to account for cross-sectional variability. Thus, the flux equation reduces to:

$$[F] = [U][A][SSC_u] + U'[A][SSC_u] + [U]A'[SSC_u] + U'\,A'[SSC_u] + [U][A]SSC_u'$$

$$+ U'[A]SSC_u' + [U]A'\,SSC_u' + U'\,A'\,SSC_u' \qquad (7.4)$$

where $[F]$ is the total discharge weighted residual suspended sediment flux, U is the channel-average velocity, A is the channel area, and SSC_u is the velocity-weighted SSC. Brackets denote a tidally averaged value, while the prime indicates the temporal deviation of the instantaneous value from the tidally averaged value (Eqs. 7.2, 7.3). Tidal averaging was performed using a low-pass Butterworth filter with a cutoff frequency of 1/30 h^{-1}. The filter was applied in the forward and reverse directions to minimize anomalies at the endpoints of the record.

Typically, the advective and dispersive flux terms (Eq. 7.4, terms 1 and 6 respectively) dominate total flux, while Stokes drift (Eq. 7.4, term 4) contributes a minor portion. Advective flux quantifies the contribution of mean discharge and mean concentration (i.e. river flow), while dispersive flux represents the correlation between velocity and concentration fluctuations. Stokes drift accounts for the correlation of velocity and area, which is landward for a progressive tidal wave. The remaining terms are either zero by definition (terms 2, 3, and 5) or negligible (terms 7, 8).

7.2.1.5 Annual sediment flux estimation

Predicting fluxes in Carquinez Strait over a year or more requires the use of surrogate measurements that are simpler to obtain than the labor-intensive measurements detailed

above. The readily available surrogates that are continuously measured are QWEST (combined discharge from four sites within the Delta; Oltmann, 1998), and lower SSC at site NBen (Buchanan and Ganju, 2005). Upper SSC was not used due to a lower data return. Lower SSC at site NBen is not available between 1999-2001, due to bridge construction. An additional surrogate that delineates the high-flow from the low-flow regime is the longitudinal salinity gradient (LSG) between Carquinez Strait and Mallard Island, which can have a strong influence on local hydrodynamics and sediment transport (Monismith et al., 1996). The quantities that must be predicted are advective ($[U][A][SSC_u]$), dispersive (U' $[A]$ SSC_u'), and Stokes drift flux ($U'A'$ $[SSC_u]$). The relationship between calculated fluxes and the surrogate variables will be investigated.

7.2.1.6 Yearly sediment budgets for Suisun Bay

Once the predictive capabilities outlined above are developed, they provide an estimate of net suspended-sediment flux through the seaward boundary of Suisun Bay. Flux estimates for the landward boundary of Suisun Bay are provided by the methods of McKee et al. (2006). Combining the estimates from the boundaries yields a sediment budget for Suisun Bay. Bedload transport and minor tributary sediment fluxes are considered negligible (Porterfield, 1980). This sediment budget does not include changes in storage caused by dredging and sand mining.

7.2.2 Results

7.2.2.1 Spring monitoring period

Point SSC in the four quadrants was successfully measured for the duration of the spring monitoring period, though fouling and debris decreased the percentage of valid data (Fig. 7.1). At site NBen, SSC data yield was 79% and 94% for the upper and lower sensors, respectively. Data yield at site SBen was 64% and 91% for the upper and lower sensors, respectively. SSC was elevated at all sites near the beginning of the record, due to episodic freshwater flow and sediment supply, overlapping with a spring tide. Inspection of the time-series data (Fig. 7.1) reveals substantial lateral and vertical variability in SSC as described in Section 6.2.2.1.

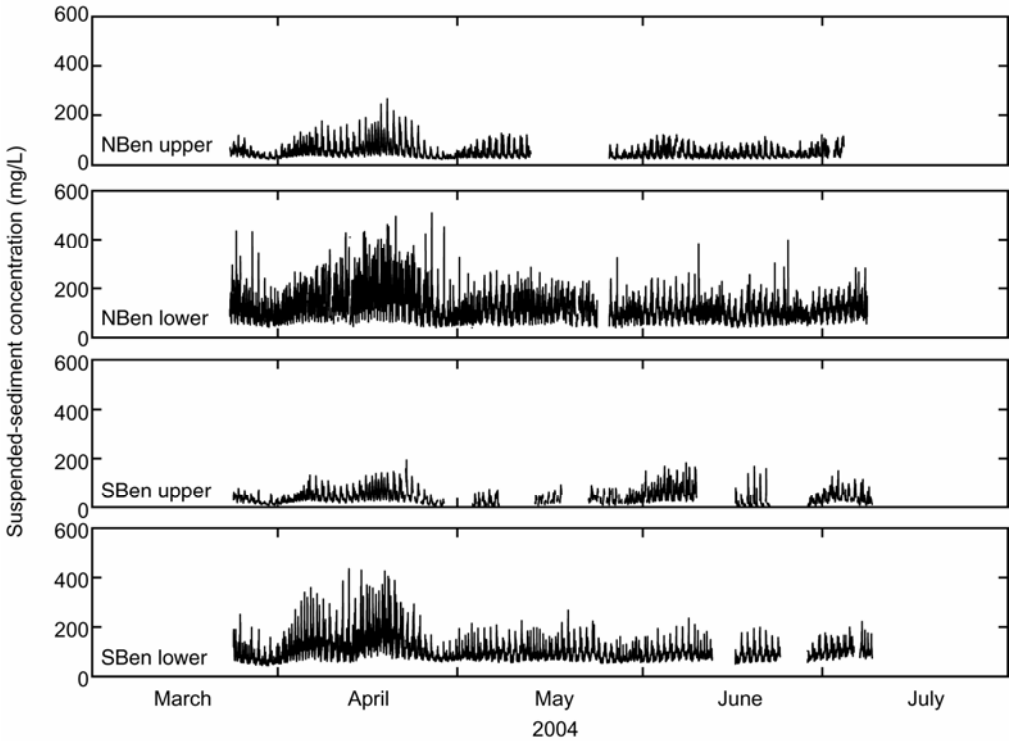

Figure 7.1 Suspended-sediment concentration (SSC) time-series from sites upper sensor at site NBen; lower sensor at site NBen; upper sensor at site SBen; and lower sensor at site SBen. Note higher data return from lower sensors. SSC was typically greater at lower sensors.

7.2.2.2 Tidal-cycle cross-sectional measurements

The tidal-cycle, cross-sectional measurements corroborate the large lateral and vertical variability observed in the time-series of point SSC. On early ebb tide, velocity in the northern half of the channel led the southern half, which was still slightly flooding. As the entire channel turned to ebb, SSC was greatest on the northern edge of the channel (Fig. 7.2). The transition from ebb to flood was characterized by increasing landward velocity in the lower water column in the south channel, while water in the north channel continued to ebb. This led to a core of high velocity near the bottom of the south channel, and SSC was also at a maximum in this region. As flood tide progressed, the velocity core began to spread laterally and vertically. Maximum SSC was still found near the bottom in the south channel, but SSC began to increase near the bottom in the north channel as well (Fig. 7.2).

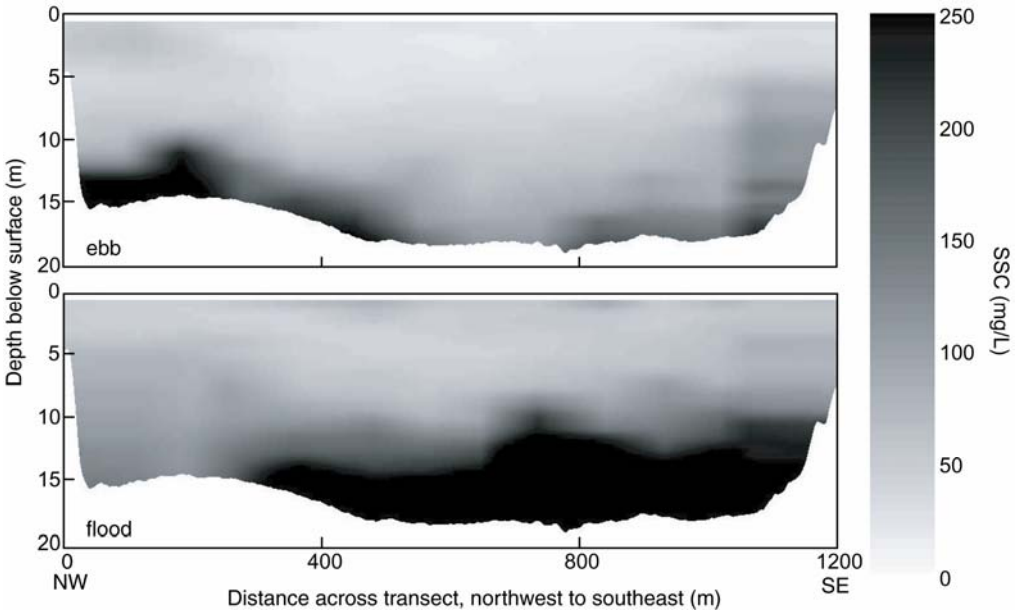

Figure 7.2 Interpolated profiles of suspended-sediment concentration. Early ebb profile shows higher concentrations in the ebb-dominant north channel, while SSC is maximized in the south channel at the beginning of flood. Maximum SSC in each profile is 320 and 1000 mg/L, respectively.

SSC_u ranged from 65 to 187 mg/L, at slack before ebb and early flood tide, respectively. SSC data were interpolated to the same location of velocity data, in order to calculate SSC_u in the cross-section (Eq. 7.1). Multiple linear regression was used for separate flood and ebb calibrations (Fig. 7.3), because of the flood/ebb variability in SSC (Fig. 7.2). Lower sensor SSC at sites NBen and SBen are the independent variables, and SSC_u is the dependent variable. The continuous time-series of SSC_u (Fig. 7.4) was created by applying the flood and ebb regressions to the individual sensor data. The SSC_u time-series retains the features from both sensors, which capture the lateral variation in SSC between flood and ebb tide.

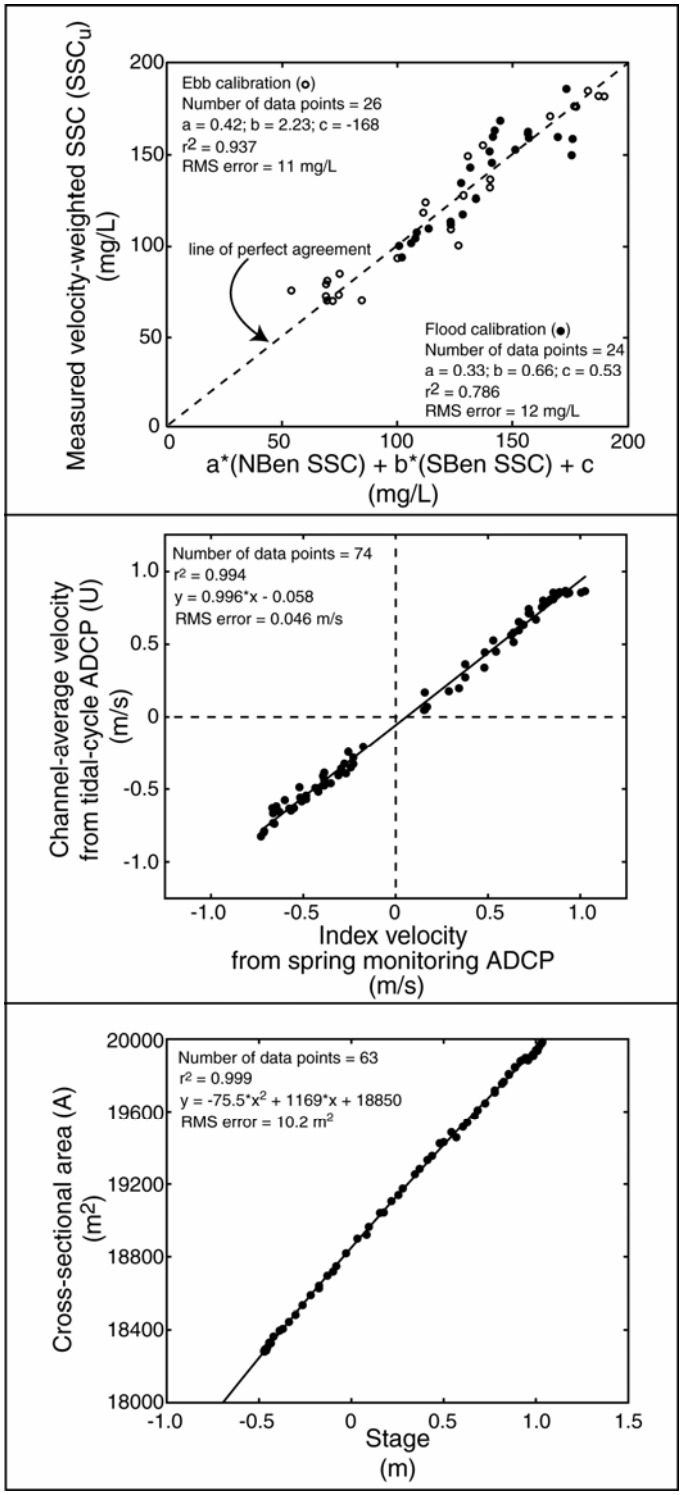

Figure 7.3 Calibration of site NBen and SBen SSC to velocity-weighted SSC (SSC_u); index velocity to channel-average velocity (U); and stage to cross-sectional area (A). Tidal-cycle measurements were used to obtain relationships that can be extended over spring monitoring period, yielding advective ($[U][A][SSC_u]$), dispersive ($U'[A][SSC_u']$), and Stokes drift ($U'A'$ $[SSC_u]$) fluxes over the spring monitoring period.

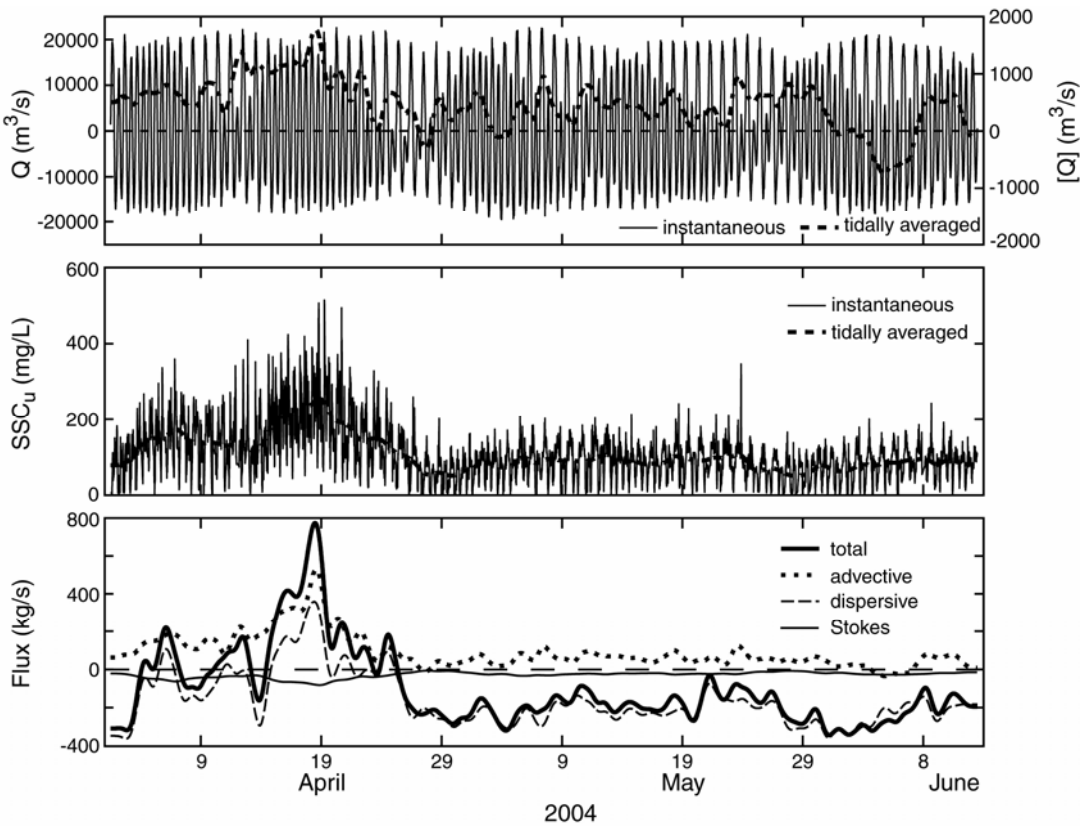

Figure 7.4 Instantaneous and tidally averaged discharge in Carquinez Strait (shifted, see Fig. 7.5), *Q* and [*Q*], respectively; velocity-weighted suspended-sediment concentration, *SSC*; and total, advective, dispersive, and Stokes drift flux components. Positive values indicate seaward (ebb) transport, negative values indicate landward (flood) transport.

7.2.2.3 Total channel discharge

The index-velocity method (Fig. 7.3) provides continuous channel-average velocity and channel cross-sectional area, and therefore continuous discharge (Fig. 7.4). The accuracy of the discharge record was evaluated in comparison with QWEST and Dayflow (California Department of Water Resources, 2005), which suggested that the estimated discharge had a slight flood bias ($Q_{original}$, Fig. 7.5). Dayflow is an idealized, unidirectional flow value that is the net water balance of all freshwater inputs and outputs to the Sacramento/San Joaquin River Delta. Due to the large cross-sectional area at the measurement site, a 1 cm/s flood bias in velocity is enough to negate a freshwater flow of

180 m^3/s, which is 50% of the mean Dayflow magnitude during the spring monitoring period. Therefore, QWEST and Dayflow were used as bounds to apply a 1 cm/s (22% of RMS error; Fig. 7.3) ebb-directed shift of the velocity data to represent freshwater flow adequately. This shift is within the error of ADCP measurement (Simpson and Bland, 2000). Other possible sources and sinks of water were investigated, including groundwater seepage and evaporation. Aquifer exchange in San Francisco Bay can be both upward and downward, but maximum downward seepage rates are 0.55 m/yr (Spinelli et al., 2002). Assuming this maximum seepage rate over the entire area of Suisun Bay (169 million m^2) yields a water volume loss of 3 m^3/s, which is negligible. Maximum evapotranspiration rates in the area were 0.007 m/d; the product of this vertical water loss and the area of Suisun Bay yields a total volume loss of 14 m^3/s, which is not enough to account for discrepancy. While the measurement of instantaneous discharge is difficult in large cross-sections, a bias in flow measurement at high flows is negligible, and at low flows the advective water flux is minimal nonetheless. The bias has no effect on dispersive fluxes, because the tidally averaged trend in water discharge is subtracted when calculating that quantity.

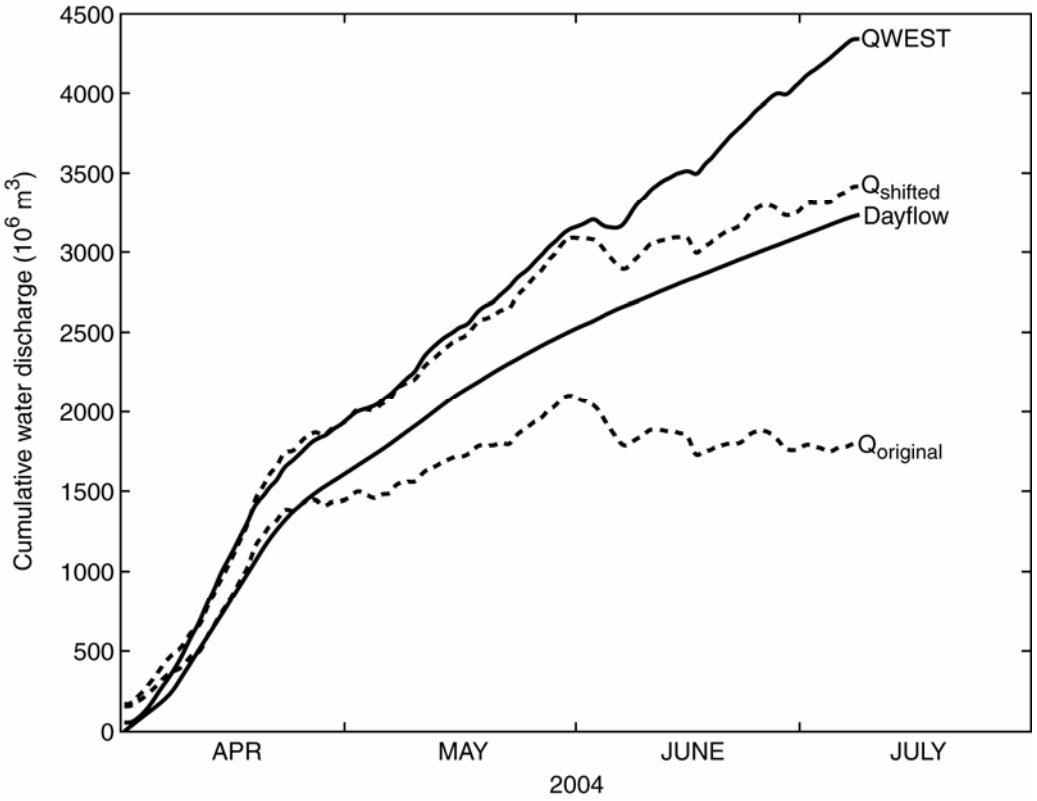

Figure 7.5 Cumulative water discharge calculated from Delta measurement sites (QWEST), Dayflow, discharge measured in Carquinez Strait ($Q_{original}$), and $Q_{original}$ with 1 cm/s ebb-directed shift ($Q_{shifted}$).

The time-series of instantaneous (Q) and tidally averaged ([Q]) discharge (Fig. 7.4) demonstrate the tidal and subtidal variability of discharge through Carquinez Strait. The mostly positive (ebb-directed) magnitude of tidally averaged discharge represents the net freshwater flow delivered through the Delta. During low freshwater flow periods (Fig. 7.4, post-April 29, 2004), residual discharge is more influenced by the spring/neap cycle, and meteorological effects such as wind and barometric pressure (Tobin et al., 1995), though it is still ebb-dominated due to continuous reservoir releases. The direction of the residual discharge can turn landward (Fig. 7.4, June 3-7, 2004) during periods of sustained onshore winds, though tidal forcing can also have a similar effect.

7.2.2.4 Flux calculation

Advective, dispersive, and Stokes drift flux components accounted for 98% of the total flux. Advective flux of sediment was predominantly in the seaward direction, while dispersive flux was mainly directed landward (as was Stokes drift). Exceptions did occur however: dispersive flux turned seaward during a period of sustained freshwater flow (April 9-19, 2004; Fig. 7.4), and advective flux was directed landward during a period of increased westerly winds (June 3-7, 2004). After freshwater flow returned to typical summer conditions (post-April 29, 2004), advective flux was minimal, while dispersive flux dominated transport.

Advective flux by definition follows the residual water flux, and increasing river flows usually correspond with increasing advective flux. The Stokes drift flux is a direct function of tidally averaged SSC_u, and therefore was maximized when tidally averaged SSC_u was a maximum. The dispersive flux measures the correlation between tidal velocity fluctuations and SSC_u, and the landward direction during low-flow can be attributed to the coincident profiles of velocity and SSC. Over the spring monitoring period, the direction of residual near-bed velocity (from the upward-looking ADCPs) was typically landward, while the direction was seaward near the top of the water column; this is commonly known as gravitational circulation and has been previously identified in Carquinez Strait. Combining landward residual near-bed velocity with high near-bed SSC (as compared to low near-surface SSC) results in a net landward flux of suspended-sediment in the Strait during low freshwater flow.

7.2.2.5 Annual sediment flux estimation

The first term of Equation 7.4 is the advective flux, which is composed of the product of $[U][A]$ and $[SSC_u]$. Estimating $[U][A]$ (advective water discharge) requires a surrogate measurement, and I use the continuously monitored, tidally averaged discharge through the Delta (QWEST). Water losses between the Delta and Carquinez Strait are assumed to be negligible, as evaporation, groundwater input/output, and surface water withdrawals are minimal. $[SSC_u]$ is replaced with the tidally averaged lower SSC from site NBen, which is measured continuously. While the intratidal dynamics of SSC at site NBen are different than the southern half of the channel (site SBen), using the tidally averaged value avoids this discrepancy. The product of QWEST and BenSSC yields a surrogate for advective flux, which is regressed against the directly calculated value to provide a calibration curve (Fig. 7.6) and predictions for the spring monitoring period (Fig. 7.7).

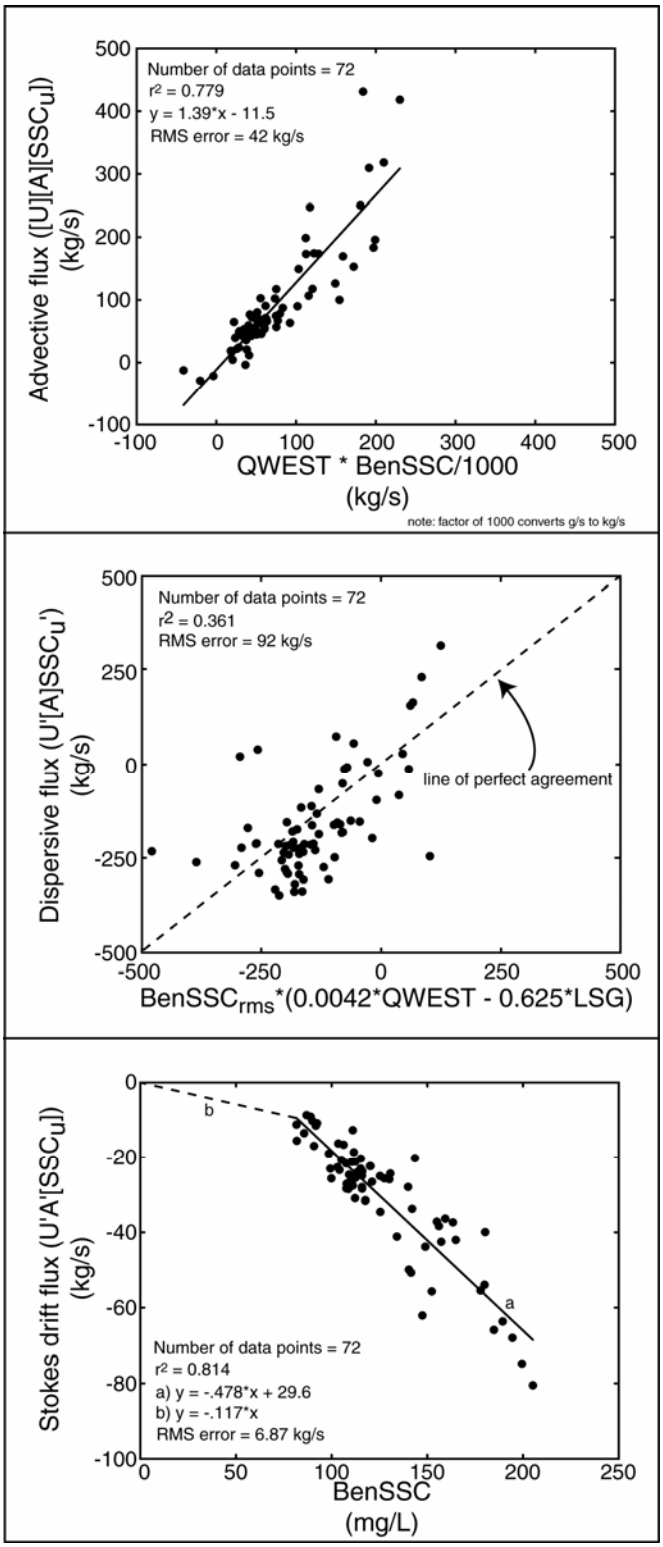

Figure 7.6 Linear regression of QWEST and lower SSC at site NBen (BenSSC) product to advective flux; multiple linear regression of RMS value of lower SSC at site NBen ($BenSSC_{rms}$), QWEST, and longitudinal salinity gradient (LSG) versus dispersive flux; and lower SSC at site NBen (BenSSC) to Stokes drift flux.

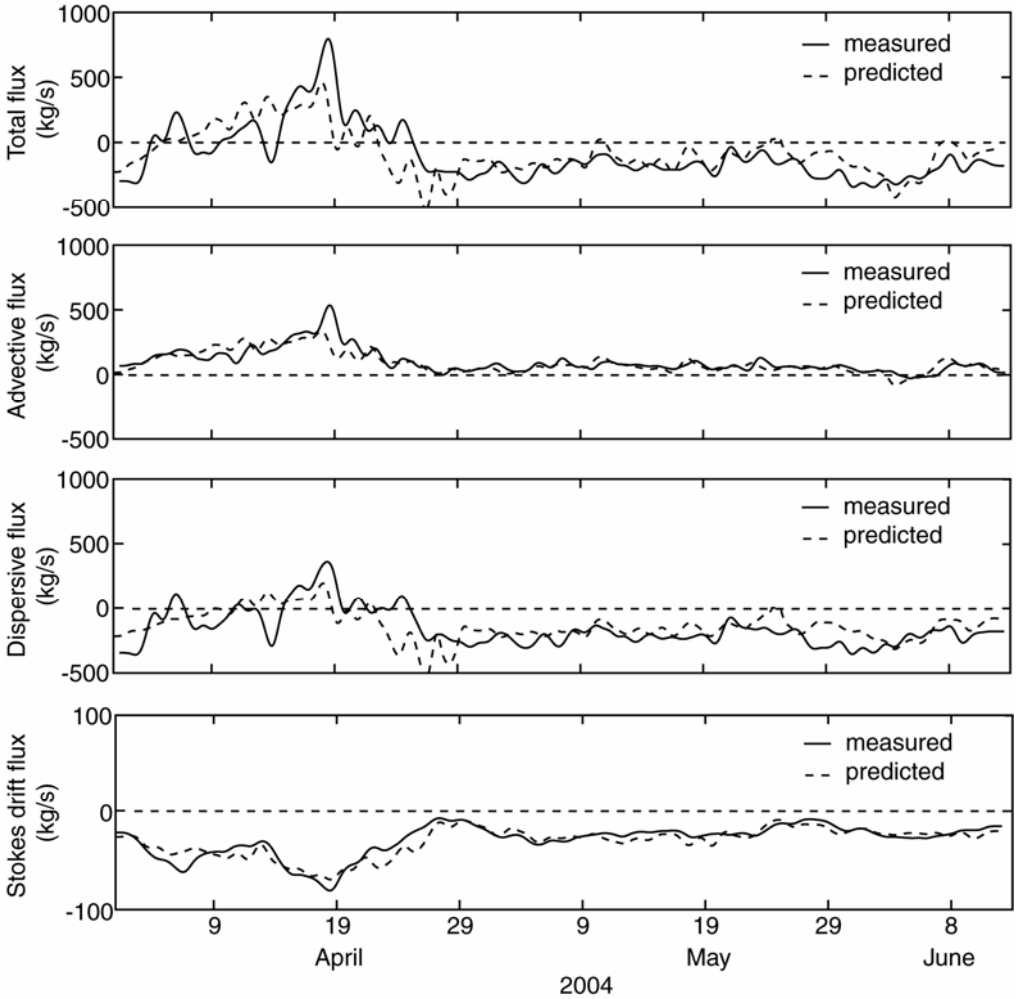

Figure 7.7 Spring monitoring period measured and predicted fluxes; total flux (sum of advective, Stokes drift, and dispersive flux); advective flux; dispersive flux; and Stokes drift flux. Positive values indicate seaward (ebb) transport, negative values indicate landward (flood) transport.

Estimating dispersive flux requires accounting for wet and dry season dynamics. From the spring monitoring results, dispersive flux was seaward during periods of high seaward advective flux, but turned landward as freshwater flow and seaward advective flux decreased. This transition occurred in concert with the return of salinity to Suisun Bay. As one regression variable I use the product of longitudinal salinity gradient (salinity

difference between Carquinez Strait and Mallard Island) in Suisun Bay and an estimate of the fluctuating suspended sediment concentration, $BenSSC_{rms}$, defined as:

$$BenSSC_{rms} = \sqrt{[(BenSSC')^2]} \tag{7.5}$$

A multiple linear regression using the product (LSG)($BenSSC_{rms}$) and the product (QWEST)($BenSSC_{rms}$) as independent variables is suitable for predicting dispersive flux (Figs. 7.6, 7.7). Seaward dispersive flux is maximized during high seaward advective flux and low salinity gradient periods, while landward dispersive flux is maximized during periods of low seaward (or significant landward) advective flux, high salinity gradient, and high $BenSSC_{rms}$.

The use of $BenSSC_{rms}$ is preferred over BenSSC because large flow events may raise BenSSC while the fluctuations are minimal. In water year 2004, for example, a 4500 m^3/s freshwater flow event (February 20, 2004) raised BenSSC, but $BenSSC_{rms}$ was minimal. Therefore, dispersive flux should be minimized at that time. Conversely, a 1700 m^3/s flow event (April 9, 2004) that coincided with a spring tide induced large BenSSC, and large $BenSSC_{rms}$. Increases in SSC due to wind-wave resuspension in San Pablo Bay (which has extensive shallow regions) are also accounted for by using $BenSSC_{rms}$.

Improved predictions of dispersive flux ($r^2 = 0.70$) were achieved by allowing for an intercept or by decoupling $BenSSC_{rms}$ from LSG, but the functionality of those relations erroneously allow for large landward dispersive fluxes when LSG is high and $BenSSC_{rms}$

is at a minimum. Therefore goodness-of-fit is sacrificed for improved conceptual functionality. Stokes drift flux is adequately predicted using BenSSC alone as a surrogate (Figs. 7.6, 7.7).

7.2.2.6 Yearly sediment budgets for Suisun Bay

Yearly predictions of sediment fluxes through Suisun Bay demonstrate large variability, though the years considered are extreme in terms of freshwater flow (Table 7.1). The data suggest that extremely wet years promote sediment export, while dry years restrict seaward advective transport, and large landward dispersive flux dominates. The only year with seaward dispersive flux is 1998, which had persistent freshwater flow and low salinity gradient through most of the summer months. The prolonged freshwater flow season possibly decreased the strength of gravitational circulation between San Pablo Bay and Suisun Bay. High SSC through the summer combined with substantial freshwater flow lead to the large export flux. The error of the dispersive flux prediction is larger than advective and Stokes drift flux predictions (Fig. 7.6), therefore differences in total dispersive flux between water years may not be significant. However the net direction of these fluxes are clearly modulated by residual flow and sediment concentrations, as an extreme year such as 1998 demonstrates.

Table 7.1. Water year, cumulative flow, sediment flux at Mallard Island, sediment flux at Carquinez Strait, net sediment budget, and advective, dispersive, and Stokes drift flux components. Positive values indicate seaward transport.

Water year	Cumulative water flow (m^3)	Sediment flux: Mallard Island (Mt)	Sediment flux: Carquinez Strait (Mt)	Net sediment budget (Mt)	Advective flux (Mt)	Dispersive flux (Mt)	Stokes drift flux (Mt)
1997	42.3×10^9	2.24	5.07	2.83 (export)	9.13	-3.15	-0.92
1998	53.6×10^9	2.42	20.93	18.51 (export)	13.00	8.94	-1.01
2002	11.3×10^9	0.309	-2.803	3.11 (import)	1.02	-3.51	-0.32
2003	17.3×10^9	0.546	0.167	0.379 (import)	2.30	-1.68	-0.45
2004	17.9×10^9	0.619	0.612	0.006 (import)	2.70	-1.56	-0.53

7.3 Modeling simulations

Most modeling parameters for this application are held constant from the last application (tidal-timescale), though sediment characteristics and wave period are modified as calibration parameters (Table 7.2).

7.3.1 Methods

7.3.1.1 Modeling domain

Though Mallard Island is the geographic landward boundary of Suisun Bay, specifying boundary conditions at this location for simulations is difficult, due to tidal variation in stage, salinity, and SSC. Bidirectional flow is observed more than 50 km landward of Mallard Island. Prescribing stage, salinity, and SSC at the Mallard Island boundary is possible for simulating recent periods, but data do not exist for periods prior to the late 20th century. Therefore extending the boundary to the bidirectional flow limit simplifies specification of boundary conditions for the hindcasting efforts. For instance,

unidirectional freshwater flow measurements exist from 1929 onwards, and prior flows can be estimated using various proxies. Salinity can be specified as zero, and sediment loads can be estimated with rating curves for the Sacramento and San Joaquin Rivers.

Table 7.2 Modeling parameters for annual-timescale simulations. Values with an asterisk were varied as calibration parameters. Sediment parameters are given for two sediment classes.

Model parameter	Value
# of x-direction cells, size range	160, 72 – 394 m
# of y-direction cells, size range	87, 102 – 593 m
# of z-direction cells	8
baroclinic time step	40 s
barotropic time step	2 s
simulation steps	788400
settling velocity*	0.10/0.25 mm s^{-1}
erosion rate*	$2x10^{-5}$ kg m^{-2} s^{-1}
critical stresses*	0.10/1.0 N m^{-2}
porosity	0.90
bed density	1000 kg m^{-3}
bed thickness	2.0 m
wave period*	1.6 s
wave fetch	20 km
water depth (for wave model)	4 m
tidal boundary velocity, stage	Flather (radiation)
river boundary velocity, stage	Flather (radiation)
tidal boundary tracers	clamped
river boundary tracers	clamped

However, the Sacramento/San Joaquin Delta represents a complex domain with multiple channels, open-water areas, flow gates, and export pumps. Including the Delta would more than double the modeling domain, and require further parameterization for in-Delta hydrodynamic processes. Due to the constraints mentioned above, I simplify the Delta in this study, as a single, continuous channel (Fig. 7.8). The channel has the same water surface area as the Delta (and therefore tidal prism), and length equivalent to the distance from Mallard Island to Freeport (on the Sacramento River), where sediment load

measurements are available. Calibration of stage and salinity within the domain of Suisun Bay is unaffected by this idealization (see Chapter 6), though sediment transport processes through the Delta to Suisun Bay must be independently verified in this chapter, by correctly modeling fluxes at the Mallard Island boundary.

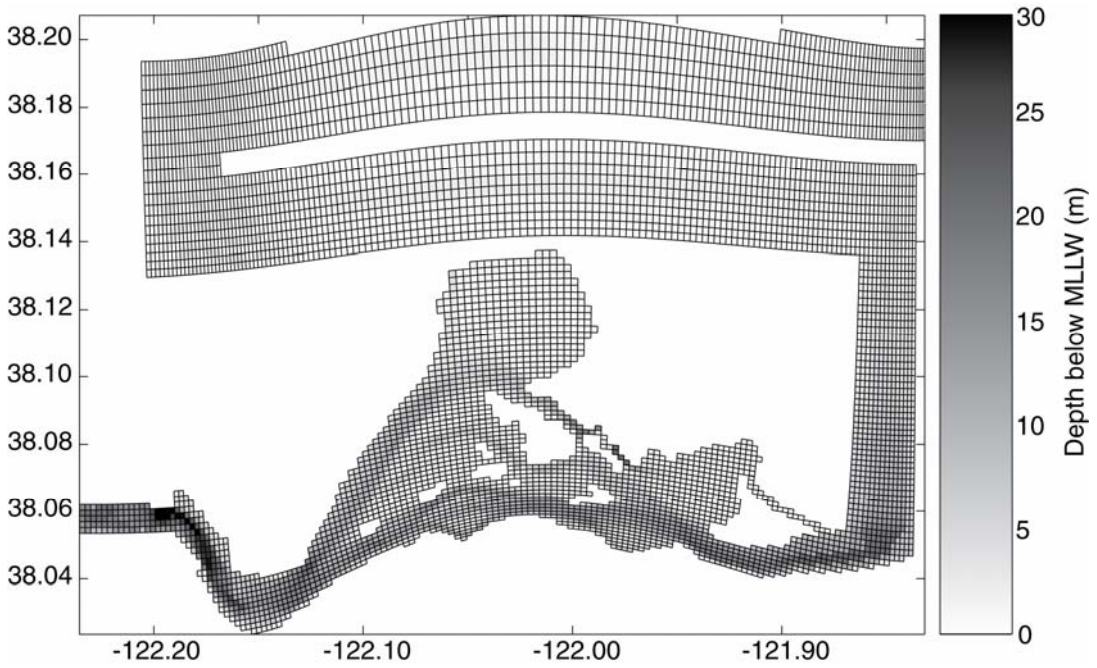

Figure 7.8 Computational grid of Suisun Bay, in ROMS orthogonal, curvilinear format. Depth is referenced to mean lower low water.

Carquinez Strait, immediately landward of the Napa River, was chosen as the seaward boundary of the domain. Eastern Carquinez Strait is subject to complex circulation dynamics due to geometry of the Strait as well as baroclinic effects. Suspended-sediment dynamics near the I-680 Bridge are sensitive to the formation of an estuarine turbidity maximum on the north side of the Strait (Schoellhamer and Burau, 1998). Inclusion of the Napa River (Fig. 1.1) was ruled out due to a lack of long-term sediment load data; therefore the logical seaward boundary was landward of the Napa River but seaward of the I-680 Bridge.

7.3.1.2 Idealization of boundary conditions

7.3.1.2.1 Landward boundary conditions: freshwater flow, salinity, SSC

Net freshwater flow into Suisun Bay is a combination of flows through the Sacramento River, San Joaquin River, the ephemeral Yolo Bypass, minor tributaries, and exports by the federal and state water projects. Because these separate inputs and outputs are not explicitly modeled, the net flow is the parameter of interest. The DAYFLOW program (California Department of Water Resources, 2006) balances these inputs and outputs, to yield a daily value of flow past Mallard Island. This value is imposed at the landward boundary of the domain. Conceptually, this ignores the within-Delta transfer of water (and therefore sediment). However, the model will be calibrated to sediment fluxes at the Mallard Island cross-section, so actual sediment retention within the Delta system will be accurately represented (though possible sediment exports by the water projects are not directly simulated). Salinity at the landward boundary is specified as zero.

Daily sediment loads past Freeport on the Sacramento River and Vernalis on the San Joaquin River were obtained from the U.S. Geological Survey. For modeling purposes, the suspended-sediment concentration is specified as a boundary condition, therefore the loads are divided by the DAYFLOW value to yield the appropriate landward boundary SSC. A single, finer sediment class was selected to represent incoming suspended-sediment. While this ignores the grain size distribution observed in riverine flows, the simplification is necessary due to limited historical data. All boundary conditions (flow, SSC, salinity, temperature) are spread equally across the cells on the landward boundary, both vertically and laterally.

7.3.1.2.2 Seaward boundary conditions: tidal flow, salinity, SSC

Because the final geomorphic model will be used for simulations spanning the 19th, 20th, and 21st centuries, idealizations are necessary for tidal height, velocity, salinity, and SSC. Tidal harmonics provide an appropriate initial estimate of historic tidal elevations and velocities. A tidal harmonic predictor was developed through instrument deployments for locations throughout San Francisco Bay (Gartner and Cheng, 1982). The predictor provides tidal elevations and velocities at the west end of Carquinez Strait, which is the seaward boundary of the modeled domain. Meteorological forcings such as wind and barometric pressure are not represented in the tidal record. The tidal elevation and depth-averaged velocity are applied uniformly in a lateral sense at the seaward boundary.

For salinity, the method of Warner et al. (2005a) can be used, which utilizes a deterministic function based on near-bottom longitudinal salinity profiles (Eqs. 6.1, 6.2). The determination of this function is detailed in Section 6.3.1.2.2.

Sediment boundary conditions are substantially more difficult, as SSC at the seaward boundary responds to watershed sediment supply, tidal energy, and wind-wave resuspension in San Pablo Bay. Because flood-tide SSC is the parameter of interest, the measured flood-tide SSC at Carquinez Bridge (Buchanan and Ganju, 2005) was averaged on a daily basis. SSC for water years 1998-2003 showed a similar pattern: seasonal signals related to freshwater flow and wind-wave resuspension were superimposed on a spring-neap pattern that had greatest variability during spring tide periods and the least variability at the beginning and end of the water year (when sediment input is at a

minimum). Therefore three signals were superimposed to recreate a synthetic time-series of SSC: a flow signal that peaks in the early spring, a seasonal wind-wave signal that peaks in the summer, and a spring-neap signal that is a function of tidal energy (obtained from tidal harmonics). The time-series is then modulated by a mean yearly SSC which is linearly related to total sediment input from the Delta during the water year. The time-series is formulated as:

$$SSC_f = \frac{SSC_{CAR}}{2}\left[1 + \cos\left(\frac{2\pi(t)}{365}\right)\right] \tag{7.6}$$

$$SSC_w = 100 + 50\left(\cos\frac{2\pi(t+200)}{365}\right) \tag{7.7}$$

$$SSC_{sn} = a_1\sqrt{SSC_f + SSC_w}\,(u_{rms} - a_2)^{a_3} \tag{7.8}$$

$$SSC_{comb} = SSC_f + SSC_w + SSC_{sn} \tag{7.9}$$

$$SSC = SSC_{comb} + 0.1(rand(0,1))SSC_{comb} \tag{7.10}$$

where SSC_f, SSC_w, SSC_{sn}, SSC_{comb}, and SSC are the flow, wind, spring-neap, combined, and final SSC signals in mg/L; a_1, a_2, and a_3 were varied to yield the best agreement with measured data (final values were 300, 0.5, and 2.6 respectively); and t is the time in days. Tidal energy, u_{rms}, is the root-mean-square value of velocity, obtained from the tidal predictions. SSC_{CAR} is the yearly mean SSC at Carquinez Bridge (Buchanan and Ganju,

2005), and was regressed to against total sediment load from the Delta (for water years 1998-2004), yielding:

$$SSC_{CAR} = 69.9Q_s\text{-}16 \tag{7.11}$$

where Q_s is the total sediment load from the Sacramento and San Joaquin Rivers in millions of tons (Mt). A random fluctuation of 10% of the SSC value is also included to represent noise. The final time-series essentially represents a tidally averaged SSC signal, which peaks during periods of high wave and tidal energy (Fig. 7.9). The SSC value was assigned equally to two sediment classes: a weaker fraction and a stronger fraction, with the same properties as assigned to the bed fractions in Suisun Bay and the Delta (discussed below).

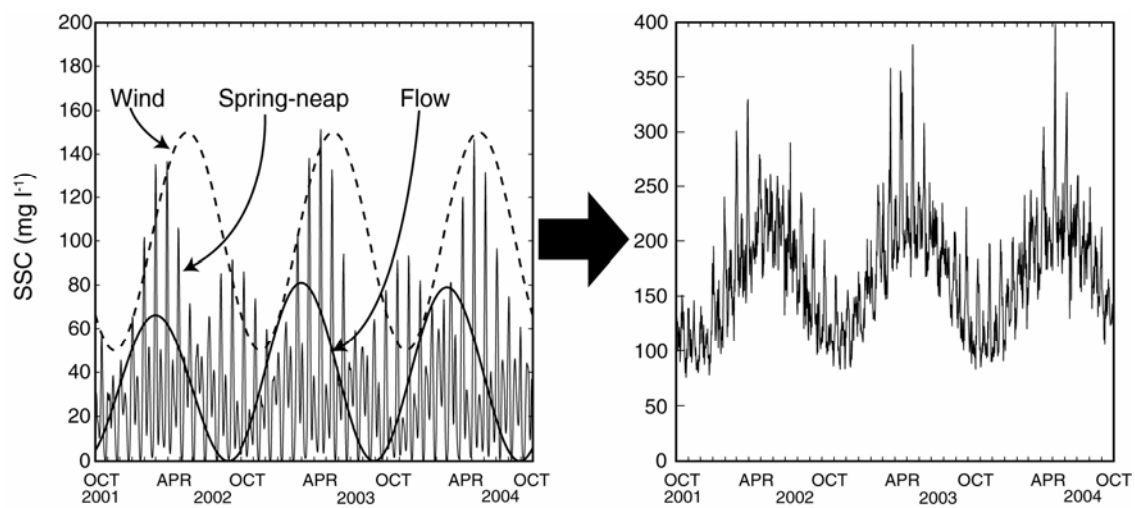

Figure 7.9 Formulation of idealized seaward SSC boundary condition for three water years, as the sum of a wind, spring-neap, and flow signal, plus a noise component (not shown).

7.3.1.2.3 Sediment bed parameters

The major modification to the sediment transport model is the inclusion of two fine sediment classes, with varying fractions in the bed, based on location. Wright and Schoellhamer (2005) demonstrate that the Delta is a net depositional environment during high flow events, while Ganju and Schoellhamer (2006) show that Suisun Bay was net erosional during high flow events. Therefore, it is necessary to "armor" the Delta and allow for a net depositional environment, while Suisun Bay should be relatively weak and erosional during high flow events. This parameterization is congruent with observed bed characteristics (Regional Monitoring Program, 2006): channels of the Delta are sand-dominated (80% sand in lower Sacramento River), while most of the Suisun Bay bed is dominated by clays and silts (90% clay/silt in Honker and Grizzly Bays). The inclusion of two sediment classes (one weak, one strong) with varying bed fractions based on geographic location will allow for proper representation of the depositional and erosional nature of the Delta and Suisun Bay. I initialize the Delta (areas landward of Mallard Island) with a 12%/88% fine/coarse distribution, while Suisun Bay is initialized with a 40%/60% distribution. The sediment parameters are given in Table 7.2. The fractions are initialized at the beginning of the simulation and allowed to evolve at each time step.

7.3.1.2.4 Atmospheric forcing

The effect of wind-waves on sediment resuspension in San Francisco Bay can be substantial during episodic winter storms and diurnal winds during the summer. Wind data from Suisun Bay were used to calculate wave height and period using the Shore Protection Manual equation for fetch and depth-limited waves, using a constant depth of

4 m (Coastal Engineering Research Center, 1984). Though fetch within Suisun Bay depends on wind direction and location, a uniform fetch of 20 km was assumed. Major wind events in Suisun Bay tend from a westerly direction, so wave direction was held constant at 270 degrees. A constant wave period is specified for simplicity, and will be varied as a calibration parameter. Though there are modern data available for implementing wind-waves in the model, there is still a need to construct a generic wind-wave time-series for historical simulations where data are not available.

7.3.1.3 Selection of calibration/validation years and calibration/validation goals

Because there are five water years of sediment flux data available, it is possible to calibrate and validate with subsets of these data. I have chosen 1997 and 2004 for calibration years for several reasons: 1) 2004 data were used to generate the regressions that led to the sediment flux predictions at the I-680 Bridge cross-section (Ganju and Schoellhamer, 2006), therefore these are the most reliable data; 2) net freshwater flow in 2004 is the closest of the five years to the average flow condition over the modern (1930-2004) period; 3) 1997 is the second-most extreme year in terms of peak freshwater flow during the modern period; and 4) 1997 represents the only wet year with significant landward dispersive fluxes during the summer (1998 had seaward dispersive fluxes during the unusually high-flow summer). The remaining water years represent years with the largest estimated sediment export (1998) and the largest estimated sediment import (2002). Theses extremes provide a validation of the model formulation and setup.

The goals in this modeling effort are, in order of decreasing importance: 1) represent the seasonal variability of cross-sectional sediment fluxes (modeled export during observed export, modeled import during observed import), 2) model relative year-to-year variability (i.e. more export in 1998 than 1997, more import in 2002 than 2003 and 2004), 3) model the net sediment budgets within the error of the estimates, and 4) model the magnitude of episodic and seasonal events within the error of the estimates. Parameters varied (Table 7.2) include wave period, critical shear stress, and settling velocity.

7.3.1.4 Sensitivity analysis

The sensitivity of the calibrated model to several of the parameterizations and idealizations is explored to ensure that net fluxes are not significantly affected by parameter specification. In order of impact on sediment transport, these parameters include, but are not limited to: 1) critical shear stress, 2) settling velocity, 3) erosion rate, 4) seaward boundary SSC, 5) landward boundary SSC, 6) tidal velocity, 7) freshwater flow magnitude, and 8) wave period. Parameters will be adjusted by 10% to favor deposition: an increase in critical shear stress, settling velocity, seaward and landward boundary SSC, and a decrease in erosion rate, tidal velocity, freshwater flow magnitude, and wave period. The initial result and the perturbed result will demonstrate the sensitivity of the model for each parameter, without the need of a third simulation favoring erosion. Each parameter will be varied separately while the remaining parameters are held at the initial calibration value. The effect on landward and seaward boundary fluxes will be observed for each of these 8 perturbations, using 2004 as the

modeled water year. This year is selected as it represents the water year with a net sediment budget closest to zero, which suggests the morphology is in equilibrium for that water year.

7.3.2 Results

7.3.2.1 Calibration and validation

Model performance was varied in regards to the four goals (Table 7.3). For the calibration years, 1997 and 2004, all goals were met, except for goal 4 in 1997 (matching of peak events). For the validation years, goals 1 and 2 were met, while goal 3 was only met for 2003. Goal 4 was met for 2002 and 2003, but not for 1998.

Table 7.3 Annual-timescale modeling performance in regards to four goals.

Year	Calibration/ validation	Goal 1: Seasonal patterns	Goal 2: Annual variability	Goal 3: Net sediment import/export	Goal 4: Event magnitudes
1997	calibration	Yes	Yes	Yes	No
1998	validation	Yes	Yes	No	No
2002	validation	Yes	Yes	No	Yes
2003	validation	Yes	Yes	Yes	Yes
2004	calibration	Yes	Yes	Yes	Yes

With respect to Goal 1, the model simulates seasonal variability well: high freshwater flows consistently result in net export from Suisun Bay, while sediment is imported from Carquinez Strait to Suisun Bay and the Delta during low freshwater flow periods (Fig. 7.10). Goal 2 is also met, as the model predicts greater erosion in 1998 than 1997, and more deposition in 2002 than 2003 and 2004 (Fig. 7.10). Goal 3 is met for 3 out of 5 years (Fig. 7.11), though the relative performance varies from year-to-year. Goal 4 is met for water years 2002, 2003, and 2004, while the episodic events in 1997 and 1998 are

overestimated at Mallard Island and underestimated at Carquinez Strait. Nonetheless, they are close to the upper and lower bounds of the estimates. The net magnitude of the seasonal landward fluxes observed in the summer is modeled well, though spring-neap variability will not match due to the use of tidal harmonics and synthetic SSC as seaward boundary conditions. Overall, poor agreement is observed during low-flow periods at Mallard Island, and during episodic events in 1997 and 1998. The discrepancies are discussed in detail (see Discussion).

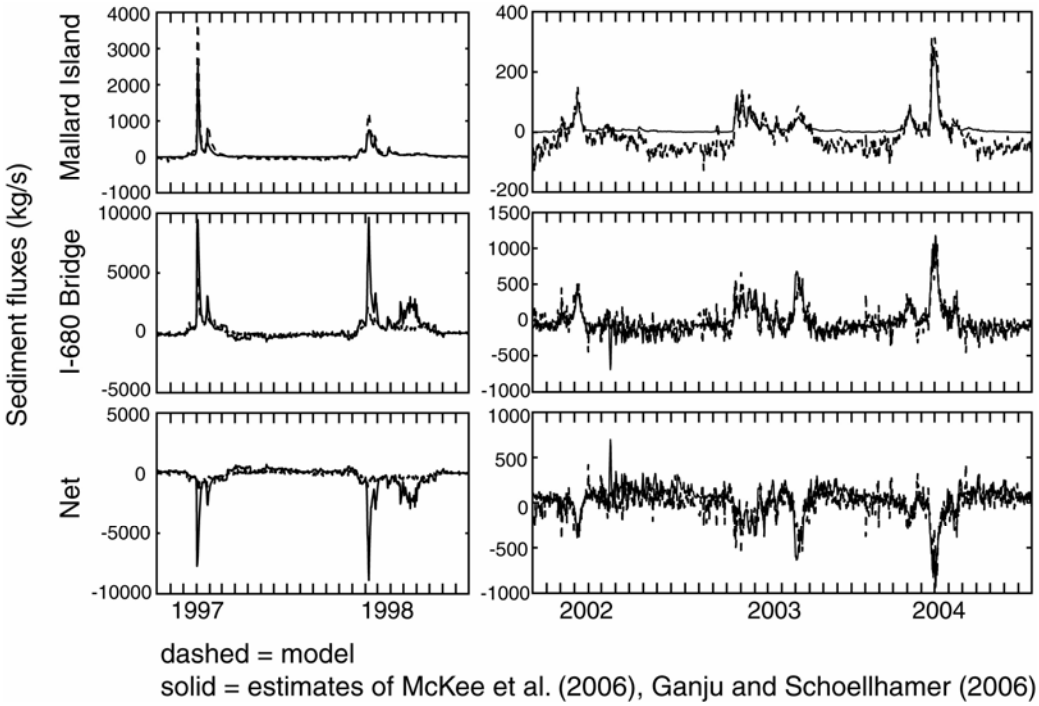

Figure 7.10 Time-series of sediment fluxes at Mallard Island, I-680 Bridge, and the net budget for Suisun Bay. Dashed lines indicate model results, solid line are estimates of McKee et al. (2006) and Ganju and Schoellhamer (2006).

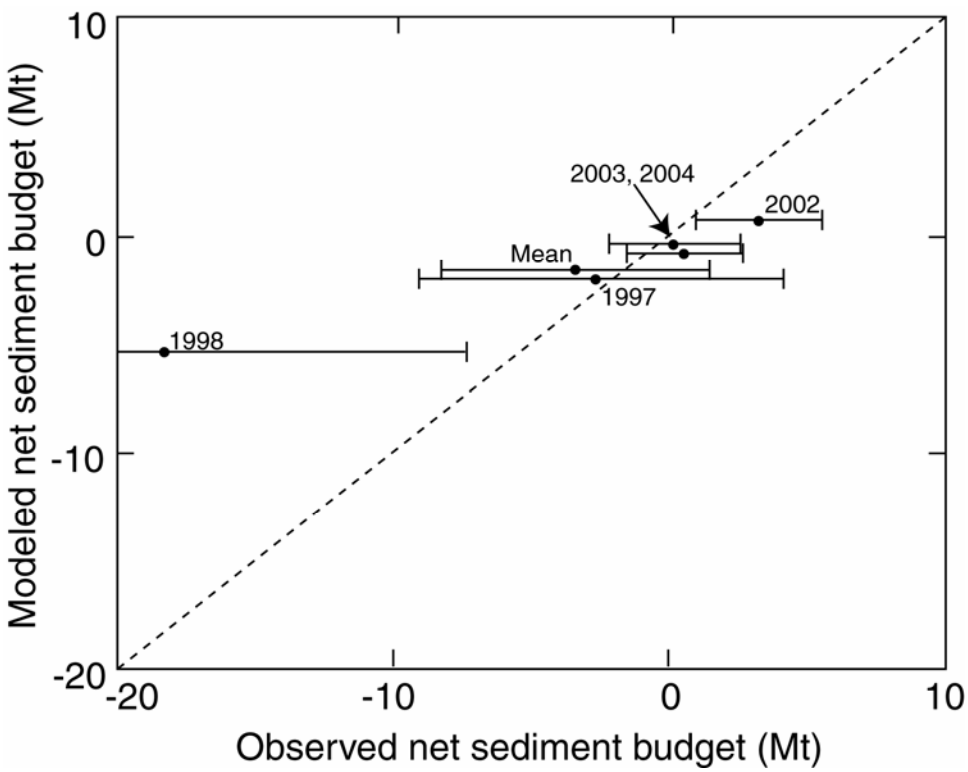

Figure 7.11 Net observed and modeled sediment budgets for five water years. Poor agreement in 1998 is due to error in the extrapolation of dry season relations (see Section 7.4.2.1).

7.3.2.2 Sensitivity analysis

Model sensitivity of sediment fluxes to model parameters (Table 7.4) varies. Perturbations of the sediment characteristics (critical shear stress, settling velocity, erosion rate, seaward SSC), favoring deposition, led to expected increases in deposition. The least sensitive parameter is SSC at the landward boundary. Despite a 10% increase in sediment load at the landward boundary, net fluxes at Mallard Island remained constant (peak loads were increased slightly). Decreases in tidal velocity led to increased deposition, due to reduced shear stresses in Suisun Bay. A decrease in freshwater flow resulted in increased Delta trapping and reduced fluxes into Suisun Bay. The most sensitive parameter was wave period. This arises from the highly non-linear relationship

between wave period and shear stress, and suggests that correct parameterization of waves is necessary for accurate simulations. All of the deviations are within the error bounds of the sediment flux measurements.

Table 7.4 Sensitivity analysis results; positive fluxes indicate seaward fluxes, negative values are landward fluxes.

Parameter	Initial value	Perturbed value	Sediment flux at Benicia (Mt)	Sediment flux at Mallard Island (Mt)	Net sediment storage (Mt)
Base simulation	--	--	0.13 (out)	-0.22 (out)	-0.35
Critical shear stress (Pa)	0.10/1.0	0.11/1.1	-0.27 (in)	-0.22 (out)	0.05
Settling velocity (mm/s)	0.10/0.25	0.11/0.275	-0.37 (in)	-0.25 (out)	0.12
Erosion rate ($kg/m^2/s$)	2×10^{-5}	1.8×10^{-5}	-0.26 (in)	-0.22 (out)	0.04
Seaward SSC (kg/m^3)	variable	Increased by 10%	-0.35 (in)	-0.22 (out)	0.13
Landward SSC (kg/m^3)	variable	Increased by 10%	0.13 (out)	-0.22 (out)	0.00
Tidal velocity (m/s)	variable	Decreased by 10%*	-0.28 (in)	-0.15 (out)	0.12
Freshwater flow (m^3/s)	variable	Decreased by 10%*	-0.31 (in)	-0.38 (out)	-0.07
Wave period (s)	1.6	1.44	-0.96 (in)	-0.09 (out)	0.87

*Note: SSC was increased for these cases to keep sediment load constant.

7.4 Discussion

7.4.1 Annual sediment flux estimates

7.4.1.1 Accuracy of long-term prediction

The extrapolation of relations developed during the transition between wet and dry season introduces errors of an unknown magnitude, but this does not change the seasonal pattern of suspended-sediment transport. The most intensive measurement period was

conducted during tidal cycles in June and July, 2004, when freshwater flow was minimized and salinity gradient was at a maximum. Those efforts resulted in relations for channel-average velocity, channel cross-sectional area, and velocity-weighted SSC (tidal-cycle measurements) as a function of index velocity, stage, and point SSC values (Fig. 7.3; spring monitoring measurements). Errors in this procedure include the error of the index-velocity method (Simpson and Bland, 2000), and the error of the velocity-weighted SSC calibration. Potential error arose from a flood-biased velocity in the index-velocity calibration, however a shift of the velocity data (22% of RMS error) was applied based on two independent measurements of freshwater flow.

From this a continuous record of fluxes was developed for the spring monitoring period, and those calculated fluxes were then related to three surrogate variables (Fig. 7.6): lower sensor SSC at site NBen, longitudinal salinity gradient, and QWEST. The regression errors indicated can only be estimated for the period of calibration, and extrapolation of these relations over higher freshwater flow events may introduce further error. RMS error for the respective flux components was 44% of mean advective flux, 48% of mean dispersive flux, and 22% of mean Stokes drift flux. Errors in the dispersive flux prediction are larger in magnitude than the other flux components, but goodness-of-fit is sacrificed for conceptual quality. Despite the limitations of these procedures, the predictive methods here can be refined by additional cross-sectional surveys of velocity and SSC during periods of major and minor freshwater flow. Because the surrogates (site NBen SSC, QWEST, and longitudinal salinity gradient) are continuously measured,

periodic surveys can check the validity of the relationships developed here, and extend relations into other regimes.

7.4.1.2 Dispersive flux prediction

The results of the spring monitoring period suggested that dispersive flux was maximized in the seaward direction during high flow (with the caveat that $BenSSC_{rms}$ is high), while landward dispersive flux is maximized when salinity gradient is maximized. The basis for this analysis is the gravitational circulation mechanism: when flow is large, the longitudinal salinity gradient is compressed in Carquinez Strait, and landward flux due to gravitational circulation is restricted. When flows are reduced, the salinity gradient expands and landward flux commences. This simplistic treatment ignores the underlying complexity of the interaction between flow, salinity gradient, and gravitational circulation. For instance, the local salinity gradient may be very different than the basin-scale salinity gradient. Measurements during the spring monitoring period show that salinity gradient is compressed in Carquinez Strait during high flows, and small within Suisun Bay. Conversely, during low flows the salinity gradient is small in Carquinez Strait, and large in Suisun Bay. I have chosen the basin-scale measurement here (salinity gradient from site Mal to site NBen) because I am estimating sediment fluxes through Carquinez Strait and into Suisun Bay. If I was aspiring to understand the local sediment flux within Carquinez Strait itself, the local salinity gradient would be of more interest. There still remains uncertainty in utilizing point values to calculate salinity gradients, as complex bathymetries and channel configurations create complex vertical and horizontal structure to the salinity field. Nonetheless, for the bulk predictions made here, the salinity

gradient between two boundary points should provide adequate representation of the average salinity dynamics.

7.4.1.3 Seasonal pattern of erosion and deposition

Previous researchers have speculated that winter freshwater flows replenish the erodible sediment pool on the bed of Suisun Bay, while the wind-dominated summer periods allow for erosion and reduction of this sediment pool. My measurements suggest the opposite pattern, at least under present watershed sediment yield conditions. For the water years considered here, the largest freshwater flood brought relatively little sediment past the Mallard Island boundary as compared to historic conditions (McKee et al., 2006). This creates a reduced sediment supply condition, and combined with the relatively high residual SSC in the water column, this results in a net export of sediment from Suisun Bay during the wet season.

Once freshwater flow subsides to typical dry season conditions, wind-wave resuspension begins to mobilize sediment throughout San Francisco Bay. Wind-wave resuspension is a major factor increasing SSC in both Suisun and San Pablo Bay; however 224 million m^2 of San Pablo Bay are shallower than 5 m, while only 97 million m^2 of Suisun Bay fit this criterion (Jaffe et al., 1998; Cappiella et al., 1999). Therefore, wind-wave resuspension has a greater effect in San Pablo Bay, creating a gradient in SSC from west to east. The landward dispersive flux leads to net deposition in Suisun Bay during the dry season, as flood tide carries relatively higher SSC than ebb tide. The two-layer flow which has been observed in Carquinez Strait also promotes landward sediment flux, since near-bottom

residual currents directed landward would coincide with higher near-bottom SSC, and seaward residual surface currents coincide with lower surface SSC. The exception to this pattern is water year 1998, which had persistent freshwater flow during the summer.

Water years with different hydrographs (Table 7.1) suggest different patterns: water year 1997 witnessed a large net seaward advective flux and large net landward dispersive flux, with a pattern similar to water year 2004. However in water year 1998, net dispersive flux was large and seaward. Despite the similar cumulative flow between water years 1997 and 1998, the increased residual flows throughout the summer in water year 1998 (due to reservoir releases) led to a low salinity gradient and persistent seaward advective flux through the normally "dry" season. The traditional wind-wave resuspension pattern during the summer, combined with increased residual flow, results in persistent export during the summer. In both years, Suisun Bay exported suspended sediment, despite large watershed sediment fluxes (McKee et al., 2006). The five water years considered here are extreme conditions (mean = 28.5 x 10^9 m^3, standard deviation = 18.4 x 10^9 m^3) and represent years when a reasonable percentage of data were available. Further data collection during several water years will assist interpretation.

7.4.1.4 Ramifications of sediment flux patterns

The suspended sediment budget of Suisun Bay has major ramifications for marsh vertical dynamics and sustainability. The fringing marshes of Suisun Bay depend on surface deposition during high water when suspended sediment is introduced in the overlying water, and deposited due to low horizontal velocities within the marsh canopy. The rate

of sediment supply to Suisun Bay, whether from the watershed (via the Delta) or seaward embayments (San Pablo Bay), is a critical factor for marsh sustainability, especially in light of sea-level rise. These results suggest sediment transport at the boundaries of Suisun Bay is highly variable on a yearly basis, though redistribution within Suisun Bay cannot be quantified by this study.

The exchange of sediment between San Pablo Bay and Suisun Bay shows that nutrients and contaminants can be introduced to Suisun Bay from San Pablo Bay. In addition, there is clearly a seasonal pattern. High concentrations of contaminants (e.g. mercury, polycyclic aromatic hydrocarbons) have been measured in the sediments of San Pablo Bay and Suisun Bay, and exchange between them shows that toxic sources in a seaward embayment can impact the water quality in a landward embayment. Contaminant and nutrient uptake rates among various species are frequently dependent on the season (e.g. Linville et al., 2002), and the seasonal exchange pattern adds another seasonal signal to the calculation of uptake.

In terms of the sediment budget for Suisun Bay, it is clear that San Pablo Bay must be an important source of sediment. Jaffe et al. (1998) show that San Pablo Bay was net depositional between 1856 and 1951, until the last measurement period (1951-1983) which showed net erosion. By comparison, Suisun Bay had a peak erosional period between 1922 and 1942, and during the last measurement period (1942-1990) that erosion rate had reduced. This may reflect a redistribution of sediment between the two subembayments, as they are still responding to the perturbation of hydraulic mining in the

mid-1800's. If San Pablo Bay has an excess of bed sediment (i.e. out of balance with the erosional force supplied by wind waves and currents), and Suisun Bay has a corresponding deficit, there should be a transfer of sediment from San Pablo Bay, either seaward or landward. Assuming that some portion of that excess can be transferred landward during low freshwater flow periods, Suisun Bay would be the recipient.

Major floods export large quantities of sediment and cause net erosion within the basin, while dry periods allow for sediment import from seaward embayments, and resulting deposition. Frequency and magnitude of floods may determine whether Suisun Bay is erosional or depositional of decadal time scales. In light of global climate change affecting regional temperatures (and therefore snowpack in the watershed), the timing and magnitude of freshwater flows to Suisun Bay may change significantly in this century (Knowles and Cayan, 2002). Larger flow events earlier in the season may greatly alter temporal erosion and deposition patterns, as the summer phase of landward delivery of sediment is further separated from the sediment export phase in the spring.

7.4.2 Model response to forcings

7.4.2.1 Watershed delivery

The delivery of suspended sediment from the Central Valley to the Delta and Suisun Bay occurs during freshwater flow pulses in the winter and spring. The Delta's depositional capacity is an important feature which must be captured to adequately simulate loads between the Delta and Suisun Bay. The use of an idealized Delta is validated by correct simulation of the episodic sediment delivery phase past Mallard Island, though modeled

sediment load past Mallard Island is biased high for the two wetter years (1997, 1998) presented here. This discrepancy may be caused by a few factors: 1) greater hydraulic efficiency of the idealized Delta, as opposed to the real Delta; 2) misrepresentation of coarse sediment as fine sediment, during peak flows; and/or 3) neglect of effects caused by sediment transport through the Yolo Bypass. A relative lack of data precludes the inclusion of a second riverine sediment class (two bed sediment classes are specified) or the Yolo Bypass within the model. It should be noted that the peak flow event of 1997 is extreme, having been exceed only once in the modern era (1930-present).

During these same periods, the modeled sediment fluxes past the I-680 Bridge cross-section are underestimated. The relationships developed in this chapter (and published by Ganju and Schoellhamer, 2006) are based on data collected during spring 2004, when freshwater flows never exceeded 1000 m^3/s. It is possible that the relationships, based on freshwater flow, salinity gradient, and point SSC, are erroneous when extrapolated to periods with higher freshwater flow, such as 1997 and 1998. To test this hypothesis, I use the simulated flow, salinity gradient, and point SSC to calculate sediment fluxes for all five water years, and compare those predictions to the actual modeled sediment fluxes. The residual error increases with flow (Fig. 7.12), suggesting that the relationships are more appropriate for low-flow periods.

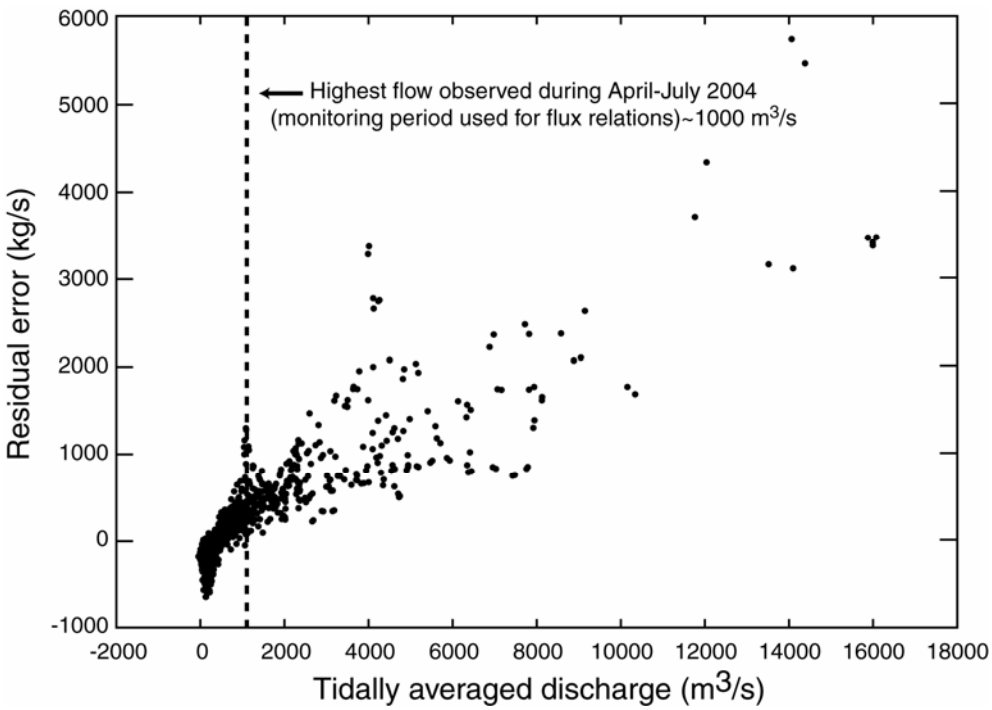

Figure 7.12 Residual error generated by extrapolating dry period empirical relationships of Ganju and Schoellhamer (2006) to wetter periods.

7.4.2.2 Wind-wave resuspension

The application of idealized wind-waves to the domain results in enhanced erosion in the shallower portions of the bay, which is consistent with previous field observations (Ruhl and Schoellhamer, 2004). The effect is minimal in deeper channels, where the shear stress induced by waves is minimized. Increased wave height results in increased erosion and sediment export from Suisun Bay, mainly during episodic wind events and the summer period. During the spring and summer, however, this is countered by increased sediment concentrations in San Pablo Bay, which is shallower and more susceptible to wind-wave resuspension (Ganju and Schoellhamer, 2006). The sediment supply from San Pablo Bay (represented by the wind signal in the synthetic SSC condition) is available to Suisun Bay through Carquinez Strait, which is a zone of increased gravitational

circulation. In order to counter sediment export from Suisun Bay due to wind-wave resuspension, sediment import due to gravitational circulation must be properly represented as well.

7.4.2.3 Gravitational circulation

Landward sediment transport due to gravitational circulation is common in partially mixed estuaries (Geyer et al., 2001), and several prior studies have identified strong gravitational circulation (Burau et al. 1993, Schoellhamer and Burau, 1998) and net landward sediment transport over prolonged periods in Carquinez Strait (Ch. 7; Ganju and Schoellhamer, 2006). The mechanism is well-represented in the model, as net landward transport is observed through the summer months, with larger magnitudes near the bed, where greater SSC coincides with residual landward flow. The magnitude of the landward transport is dependent on the synthetic SSC and residual flow; while the synthetic SSC is known *a priori*, the residual flow follows the expected pattern of seaward flows during high freshwater flow, and landward flows near the bed during low freshwater flow. This summertime sediment import to Suisun Bay counteracts erosion due to wind-waves within the shallower portions, resulting in net import during the summer periods for all water years except 1998 (when freshwater flow was elevated through the summer).

7.4.2.4 Landward sediment flux at Mallard Island

The flux estimates at the Mallard Island cross-section (McKee et al., 2006) estimate daily advective flux, and use an adjustment to correct for possible landward dispersive flux.

The adjustment was based on the ratio of point dispersive to advective fluxes, at the southern end of the channel. The ratio was found to be mostly negative, i.e. dispersive fluxes were consistently in the landward direction; however this formulation may underestimate landward dispersive flux. McKee et al. (2006) calculate landward dispersive flux to be 20% of the seaward advective flux over the nine-year study period. The modeling work here shows the percentage to be representative of high-flow years (e.g., 1997), but landward flux can account for as much as 80% of the total flux during the driest year modeled (2002). Averaging the modeled sediment flux in the cross-section over the entire year (2002) shows net seaward flux in the upper water column, and net landward flux in the lower water column (Fig. 7.13).

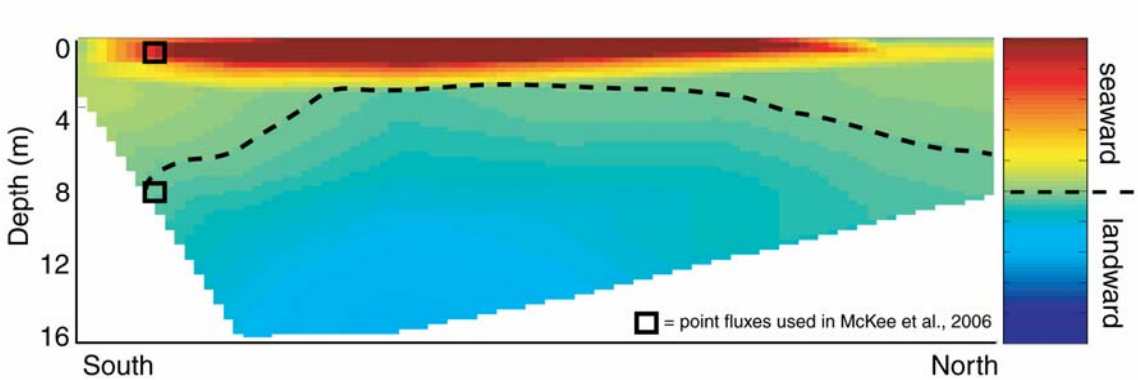

Figure 7.13 Model results for net sediment flux at the Mallard Island cross-section for water year 2002.

The point measurements used for the McKee et al. (2006) relationships were collected at depths which the model identifies as neutral to seaward flux locations. Therefore the modeled landward fluxes are realistic, and represent the landward redistribution of Suisun Bay sediments during low-flow periods.

7.4.2.5 Model calibration and validation performance

With adjustment of sediment characteristics and wave period, the model was able to recreate the timing and magnitude of critical sediment transport processes in Suisun Bay: watershed delivery of sediment, gravitational circulation, and wind-wave resuspension. Limitations in data preclude further modification of the model to estimate extreme episodic events at both Mallard Island and Benicia (Sec. 7.4.2.1), but the model does perform well in more typical conditions (water years 2002-2004). Model parameters fall within typical values within the literature, and can now be extended to the historical simulations of Chapter 8.

7.5 Conclusions

In this chapter, I calibrate the model to two years of sediment flux data by adjusting sediment characteristics and wave period and validate with three remaining years of sediment flux data. The idealized model successfully captures seasonal and yearly sediment transport cycles, and simulates the net sediment budget correctly for 3 of 5 water years. This robust test of the model gives further confidence for hindcasting simulations of bathymetric change (Chapter 8), and future simulations of geomorphic evolution in response to climate change, sea-level rise, and decreased sediment supply (Chapter 9).

Despite the highly variable nature of velocity, salinity, and SSC in estuarine cross-sections, reasonable measurements of suspended-sediment flux can be made over limited periods. Ideally, these measurements can be related to continuously monitored surrogates.

Such a procedure was performed for Carquinez Strait, California, the seaward boundary of Suisun Bay. The calculated fluxes show a clear pattern of seasonality to the advective and dispersive fluxes; these patterns suggest that down-estuary subembayments are major sources of sediment to lower-energy landward embayments, especially when watershed sediment fluxes to the landward embayment are negligible. Predictions for several water years indicate that Suisun Bay exports sediment during the wet season, and imports sediment from San Pablo Bay, the seaward embayment, during the dry season. The exception to this is water year 1998, when persistent freshwater flows were observed during the summer. The seasonal sediment flux pattern may be due to a trend of sediment redistribution from San Pablo Bay (which was depositional between 1856 and 1951, but erosional between 1951 and 1983) to Suisun Bay (where erosion rate has been decreasing since 1942). Net sediment transport to and from Suisun Bay has major implications for marsh restoration and nutrient/contaminant transport in the entire San Francisco Bay. Exchanges of sediment-associated contaminants and nutrients are clearly important between embayments, and are not simply one-way processes from watershed to ocean.

Developing an estuarine geomorphic model requires appropriate calibration data beyond tidal stage, currents, salinity, and SSC. Optimally, frequent bathymetric surveys can be used for evaluating the capabilities of a model. However, the time and cost-intensive nature of these surveys dictates typical intervals of at least a decade. This is sufficient to evaluate the performance of a geomorphic model; however decades of sediment transport must be modeled up-front. An accompanying data set of continuous sediment fluxes at the domain boundaries provides another metric by which to evaluate the model. The

performance of the model can be evaluated relatively quickly, by simulating seasonal and yearly transport cycles. Bathymetric change data ensure correct evaluation of spatial patterns of erosion and deposition, while sediment flux data ensure that the net sediment budget is correctly modeled.

8 Objective D: Calibration to decadal-timescale processes

8.1 Introduction

The previous two chapters have demonstrated the capability of the developed model to simulate tidal and annual-timescale sediment transport processes in Suisun Bay. These processes are responsible for the decadal-timescale evolution of an estuary, and therefore must be modeled correctly before attempting decadal simulations. In this chapter I apply the model to decadal simulations, attempting to recreate historical bathymetric change data. Parameters from the previous simulations may be altered due to the use of a more advanced wave-current interaction module, and the use of innovative time-stepping techniques.

Geomorphic evolution of estuarine habitats and landscapes over decadal timescales (>10 years) is sensitive to sediment supply from the watershed and seaward embayments, local erosion, and estuarine hydrodynamics. Both sediment supply and hydrodynamics can be modified by anthropogenic activities and climate change. In Suisun Bay, hydraulic mining during the 1800's accelerated deposition, and perturbed the system well into the future. Using these data as calibration for the geomorphic model will bolster the future scenarios modeling.

Modeling of decadal-scale geomorphic evolution has recently become a topic of great interest, especially in light of continued sea-level rise. Hibma et al. (2003) model the evolution of an idealized estuary over 100 y, recreating patterns of channel-shoal interaction, while Roelvink (2006) focused on the implementation of the routines and

their effect on the evolution of an idealized tidal inlet. Sutherland et al. (2004) provide a basis for evaluating model performance with regard to geomorphic evolution. Lesser et al. (2004) review the development, validation, and testing of a three-dimensional geomorphic model, including a comparison of model performance with bathymetric data near a modified harbor. These prior efforts have colored my approach, especially in regards to simplifying inputs and boundary conditions (e.g. Latteux, 1995). A variant of selective bathymetric updating implemented by Lesser et al. (2004) is also used for efficiency and accuracy, along with a morphological acceleration factor. The availability of bathymetric data for Suisun Bay (Cappiella et al., 1999) makes this effort possible.

Modeling the future evolution of an estuary cannot be done with confidence if proper calibration data do not exist. Prior efforts have relied on calibration to modern data such as tidal stage, salinity, or suspended-sediment concentration (SSC). While these data may be appropriate for tidal-timescale analyses, decadal scale modeling is subject to large errors due to incorrect parameter specification (Schoellhamer et al., in press). Spin-up errors, where the bathymetry adjusts to the incorrect parameters, can be a major source of error. These errors are avoided when calibration data such as boundary sediment fluxes and bathymetric surveys are available. In Chapter 7, I calibrated and validated the sediment transport model using five years of cross-sectional sediment flux data; this calibration step ensures that the seasonal sediment transport mechanics of the model are correct, and that modeled yearly sediment import/export is accurate. However, these data do not give information on the accuracy of the spatial patterns of erosion and deposition within the model. This can only be verified with bathymetry data over several time

periods. Therefore I use the model to hindcast bathymetric change data (Cappiella et al., 1999) for Suisun Bay.

8.2 Field observations

Cappiella et al. (1999) compiled bathymetry soundings from five surveys in Suisun Bay, performed in 1867, 1887, 1922, 1942, and 1990. The digitized data were interpolated to a 25 m grid, and changes in erosion and deposition were computed (Fig. 8.1). During the 1867-1887 period, increased sediment supply from hydraulic mining caused an average of 0.03 m/y deposition in Suisun Bay and Carquinez Strait. In Suisun Bay alone, average deposition was 0.02 m/y. Notably, the 1867-1887 bathymetric change grid is the only one which contains Grizzly Bay, the largest off-channel shoal area in Suisun Bay (Grizzly Bay was not surveyed in 1922 and 1942).

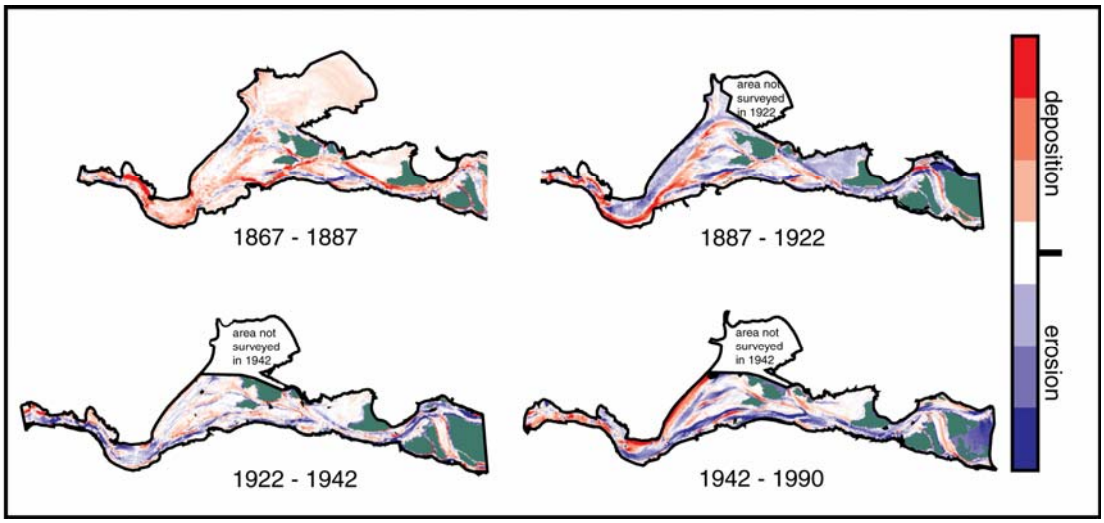

Figure 8.1 Bathymetric change maps of Cappiella et al. (1999). Increased deposition between 1867-1887 resulted from seaward transport of hydraulic mining debris.

8.3 Modeling simulations

8.3.1 Methods

Model parameters for these simulations are varied to obtain the best agreement with the bathymetric change data of Cappiella et al. (1999); the use of a more advanced wave model led to a re-calibration of the constant wave period, while in-Delta sediment storage must be calibrated to match historical data. This is achieved by modifying sediment characteristics and spatial distribution of the two size classes.

Table 8.1 Model parameters for decadal-timescale simulations. Values marked with an asterisk were varied for calibration.

Model parameter	Value
# of x-direction cells, size range	160, 72 – 394 m
# of y-direction cells, size range	87, 102 – 593 m
# of z-direction cells	4
baroclinic time step	40 s
barotropic time step	2 s
simulation steps	788400
settling velocity	0.10/0.25 mm s^{-1}
erosion rate	$2x10^{-5}$ kg m^{-2} s^{-1}
critical stresses*	0.15/1.05 N m^{-2}
porosity	0.60
bed density*	2000 kg m^{-3}
initial bed thickness	2.0 m
wave period*	1.425 s
wave fetch	20 km
water depth (for wave model)	evolving bathymetry
tidal boundary velocity, stage	Flather (radiation)
river boundary velocity, stage	Flather (radiation)
tidal boundary tracers	clamped
river boundary tracers	clamped
morphological acceleration factor	20

8.3.1.1 Modeling domain

The Suisun Bay bathymetric grids of Cappiella et al. (1999) are interpolated to a curvilinear, orthogonal grid of the same resolution as was used in the previous modeling

efforts (Fig. 8.2). The extensive shoal at the northeastern end of Grizzly Bay (Fig. 8.1) is ignored here due to interference with the idealized Delta in the computational grid, and also because the area was diked and filled in the late 19th century. The idealized Delta utilized in tidal and annual-timescale modeling is used again for this study. The shape, depths, and trapping efficiency of the actual Delta have varied over the last 150 years (Thompson, 1957), though there are no detailed data of use for this step. Instead, I will ensure that the amount of sediment delivered through the Delta roughly matches the estimates of Gilbert (1917).

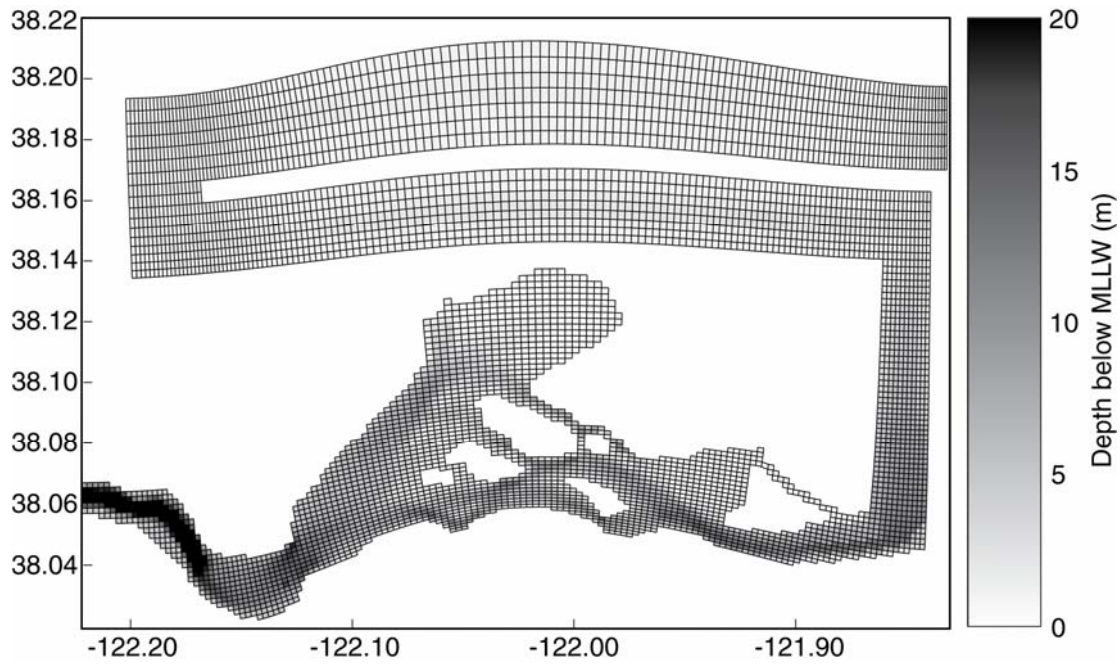

Figure 8.2 Model domain for hindcasting simulations. Configuration of 1867 has greater extent of shallows and islands, and generally wider channels.

8.3.1.2 Idealization of boundary conditions

8.3.1.2.1 Landward boundary conditions: freshwater flow, salinity, SSC

Daily flow and sediment load data to the Sacramento/San Joaquin River Delta are available after 1930 and 1959, respectively, but hindcasting simulations prior to this

require a method to generate daily sediment load estimates into the Delta. I use two historical proxies, monthly rainfall and unimpaired flow magnitudes, to generate monthly unimpaired flows to the Sacramento/San Joaquin Delta for the 1851-1929 period. These historical monthly flows are compared to unimpaired monthly flows from the modern era (1967-1987), and a least-squares metric selects a modern year analogue for each historical year. The daily hydrograph for the modern analogue is then assigned to the historical year and scaled to match the flow volume estimated by dendrochronology methods (Meko et al., 2001; 2002). I apply a sediment rating curve to this time-series of daily flows, to generate daily sediment loads for 1851-1958. The rating curve is calibrated with the bulk historical load estimates of Gilbert (1917) and Porterfield (1980). Extensive details of this procedure can be found in Ganju et al. (in review).

8.3.1.2.2 Seaward boundary conditions: tidal flow, salinity, SSC

As in Section 7.3.1.2.2, tidal harmonics provide an appropriate initial estimate of historic tidal elevations and velocities. A tidal harmonic predictor was developed through instrument deployments (Gartner and Cheng, 1982), for locations throughout San Francisco Bay. The predictor provides tidal elevations and velocities at the west end of Carquinez Strait, which is the seaward boundary of the modeled domain. Meteorological forcings such as wind and barometric pressure are not represented in the tidal record. The tidal elevation and depth-averaged velocity are applied uniformly in a lateral sense at the seaward boundary.

For salinity, the method of Warner et al. (2005a) is used again, with the same functions and coefficients. Use of the same coefficients implies that the relationship between the tidally averaged salinity field and freshwater flow is unchanged since 1867. This may not be a valid assumption, as tidal prism and basin shape have changed, but data is not available to refute the assumption. The determination of this function is detailed in Section 6.3.1.2.2.

The same synthetic SSC formulation from Section 7.3.1.2.2 is used for the historical simulations. It is important to note that the response of San Pablo Bay (seaward embayment) to the hydraulic mining pulse may change the SSC boundary condition. However it was not necessary to modify the synthetic SSC condition for these simulations.

8.3.1.2.3 Sediment bed parameters

As in Section 7.3.1.2.3, the sediment bed parameters such as critical shear stress must be used as calibration parameters. There are no data concerning historical sediment bed composition, but I can begin with reasonable values given the current state of knowledge. I will begin with the same values used in Section 7.3.1.2.3, and modify as necessary. The sensitivity analysis will quantify the range of uncertainty associated with these and other parameters. Preliminary model runs showed systemic erosion in deeper channels, this is attributed to initially large fine fraction in the channels, which is not consistent with recent field data (Regional Monitoring Program, 2006). Therefore, I increase the fraction

of the coarse size class in all areas deeper than 7 m. The fraction is varied to gain best agreement in deeper channels.

8.3.1.2.4 Atmospheric forcing

Spectral analysis of hourly winds in Suisun Bay shows three predominant wind frequencies: yearly, weekly, and daily. The yearly signal is attributed to the steady onshore winds during the summer, which peak between June and August. Winter winds are usually associated with episodic Pacific storms. During the summer months, a multi-day and diurnal wind signal results from the solar warming and cooling of the Central Valley air mass, leading to periods of strengthened landward winds. A synthetic time-series was developed using the following three signals (Fig. 8.3):

$$U_s = a_w\left(1+\cos\frac{2\pi(t+182)}{365}\right) \tag{8.1}$$

$$U_w = b_w\left(\frac{U_s}{3}+\cos\frac{2\pi(t)}{8}\right) \tag{8.2}$$

$$U_d = c_w \cos(2\pi(t+0.5)) \tag{8.3}$$

$$U_f = U_s + U_w + U_d - 1 \tag{8.4}$$

where U_s, U_w, U_d, and U_f are the seasonal, weekly, daily, and final wind time-series, and $a_w = 2.75$, $b_w=2$, and $c_w=2$. The final signal compares well with measured winds (Fig. 8.4). This signal ignores episodic winds associated with the passage of storms, but

preliminary simulations with measured winds indicated that ignoring episodic winds does not introduce significant error. The wind speed is provided to the model, which then calculates the fetch-limited wave height as described in Section 7.3.1.2.4. Due to the complexity of wind and wave propagation within an irregular basin, fetch is held constant at 20 km, and wave period is also held constant (but will be varied as a calibration parameter). For simplicity, wave direction is held constant at 270°, which is the predominant wind direction. This will ultimately affect wave-current interaction. Water depth is utilized in this computation, using the evolving bathymetry and water surface elevation. This model improvement was made due to the need for feedback between geomorphic evolution and wave-induced bottom stress.

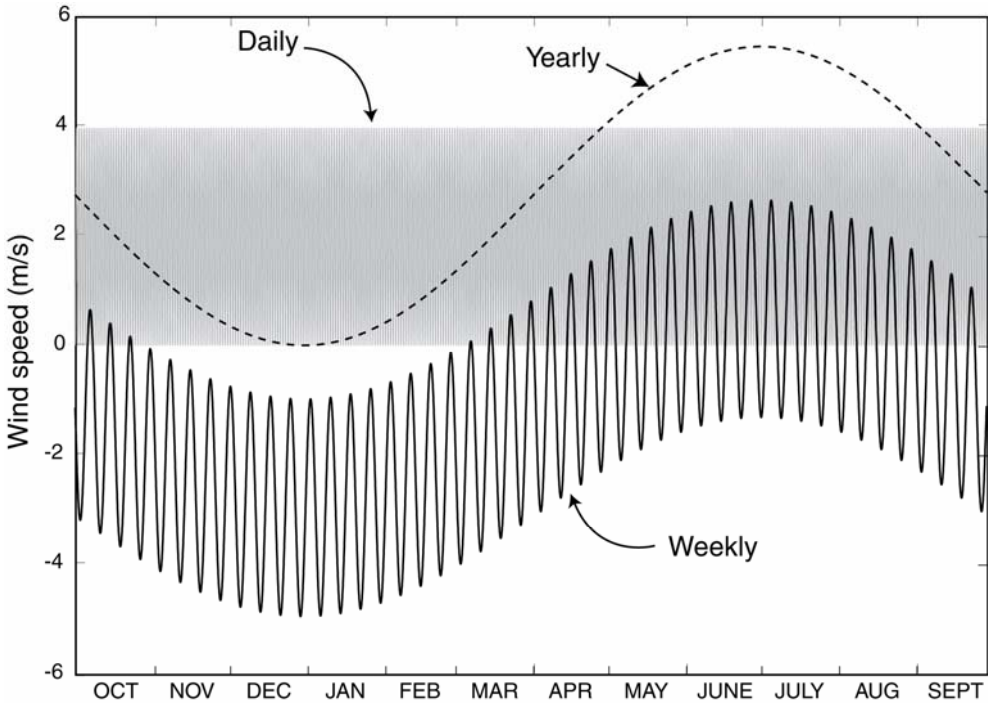

Figure 8.3 Three synthetic signals used to generate wind speed time-series for hindcasting simulations. Final time-series is clipped so as to contain no values less than zero.

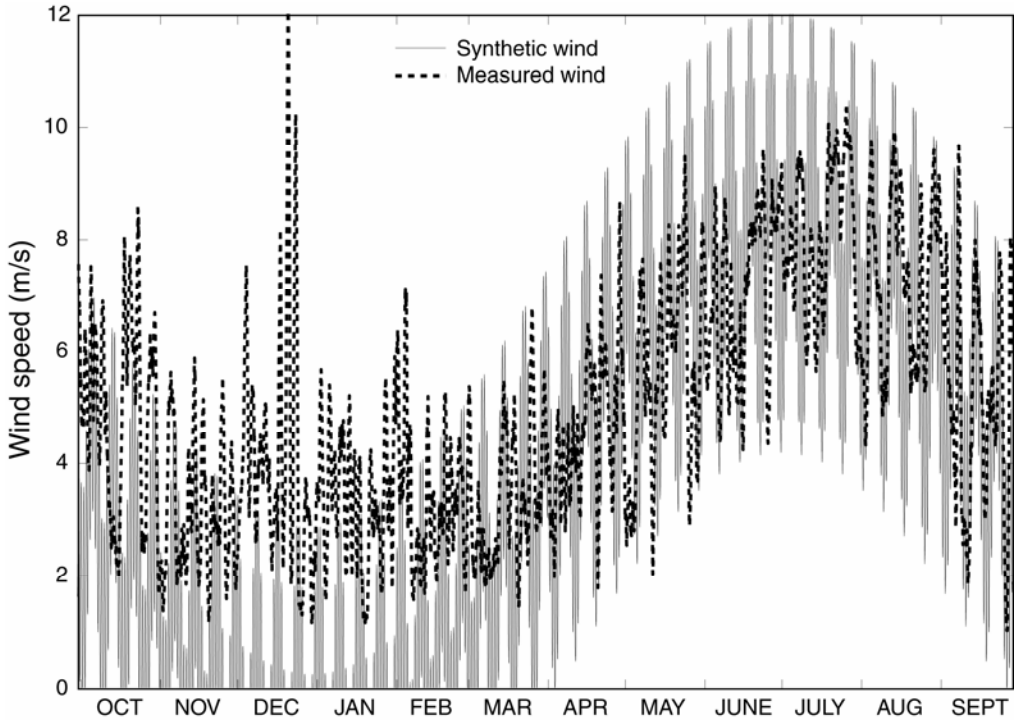

Figure 8.4 Final synthetic signal compared with measured wind from 1998. Episodic winter storm winds (notably December) in the measured record are ignored in the synthetic record.

8.3.1.3 Idealized time-stepping: morphological hydrograph and morphological factor

Computational resources are limited in many cases, and multi-decadal simulations can be computationally intensive. Simulating future scenarios of a century or more requires simplification of forcings, boundary conditions, and/or time-stepping. Prior efforts have idealized the variability of tides and winds (e.g. Latteux, 1995), while others have modified the bed-updating process, to extrapolate bed changes over limited periods (e.g. Hibma et al., 2003; Roelvink, 2006; Lesser et al., 2004). The latter method allows for a careful modeling of bed evolution, with reduced computational expense.

A common theme in extended estuarine geomorphic simulations is the concept of the morphological tide. A single tide can be identified that, when repeated, gives the same morphological result as the actual tides. This concept can be extended to all of the requisite forcings, including the concept of a "morphological hydrograph". For historical simulations (when actual hydrographs are not available), the aforementioned matching procedure (Section 8.3.1.2.1) selects a representative hydrograph from a limited set of modern data. For example, for the simulation period 1867-1887, three modern hydrographs are repeated several times (1969, 1975, 1978; Fig. 8.5). The representative hydrographs (and sediment loads) can be scaled such that the mean sediment loads are the same as the entire period. These hydrographs can then be modeled individually, with the same initial conditions, and their individual bathymetric changes can be scaled up by their rate of occurrence. Following this concept, modern hydrographs can be compared to a limited set of hydrographs that represent different types of flow signatures (which may also have different morphological signatures): rainfall-dominated, snowmelt-dominated, mixed, and drought. This limits the number of simulations necessary and extends the concept of the morphological tide to the hydrograph as well.

Once a limited set of hydrographs, i.e. P_1, P_2, P_3…. P_n, are identified, matched to actual years, and scaled, each morphological hydrograph is used as input for a one-year simulation, using initial bathymetry. The bathymetric changes for each year, Δh_{P1}, Δh_{P2}, Δh_{P3}…Δh_{Pn}, are scaled up based on the occurrence rate of each prototype in the record. The sum of these bathymetric changes represents the modeled bathymetric change over the entire period. For the 1867-1887 period, the matching procedure selected 1969, 1975,

and 1978 four times each. The mean sediment loads of the three hydrographs (10 Mt), in this case, is the same as the mean sediment load for the 1867-1887 period (Ganju et al., in review).

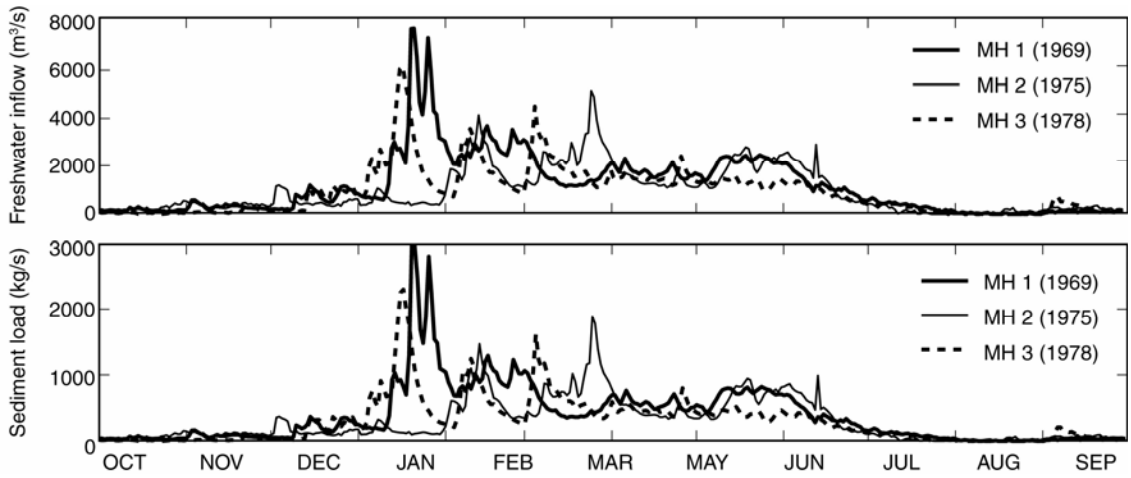

Figure 8.5 Freshwater flows and sediment loads for the three morphological hydrographs (MH).

The other essential modification is the use of a morphological acceleration factor (Lesser et al., 2004; Roelvink, 2006), which accelerates bed changes within the model. Details of the implementation are given in Warner et al. (in review). At each time step, the calculated bed sediment fluxes are scaled up by the factor, to produce an accelerated bed change. This follows the concept of the lengthened tide (Latteux, 1995), and allows for correct extrapolation of short-term bed changes. By using a factor of 20, for example, the changes over one tidal cycle now represent the changes over 20 tidal cycles; changes over one year now represent the changes over 20 years; feedback between the morphology and hydrodynamics are not ignored (as would be the case with an offline-extrapolation). For each morphological hydrograph, a one-year simulation with a morphological factor can represent the scaled-up changes in bathymetry that would result from twenty years of that particular hydrograph. The changes computed for all morphological hydrographs can be

averaged to yield the simulated 20 year change. The use of the morphological acceleration factor and the morphological hydrograph has not been verified with field data to date; this study will demonstrate the possible benefits and shortcomings of the two methods.

8.3.1.4 Selection of calibration goals

There are several levels of calibration success that can be evaluated for a morphological simulation, here I identify two primary goals: accurate representation of net vertical deposition within the entirety of Suisun Bay over the 1867-1887 period, and accurate representation of net vertical erosion or deposition in specific depth ranges. Satisfying the net bed change in specific depth ranges will necessarily satisfy the net bed change in all of Suisun Bay. Parameters that will be varied include critical erosion shear stress, wave period, and bed density (Table 8.1). These parameters were chosen due to their influence on sediment transport and vertical accretion. I seek to minimize the error between observed and predicted depth changes for individual depth ranges, keeping in mind the areal extent of those depth ranges. For example, areas shallower than 2 m cover 40% of Suisun Bay (Fig. 8.6), and are potentially important zones of ecological production (e.g. Lopez et al., 2006). An additional metric is the areally weighted average of error as a percentage of depth; i.e. 0.1 m of error in 10 m gives an error percentage of 1%, the same as 0.01 m in 1 m of water. For each depth range, these errors are weighted by the area, and averaged to yield a mean weighted error relative to depth.

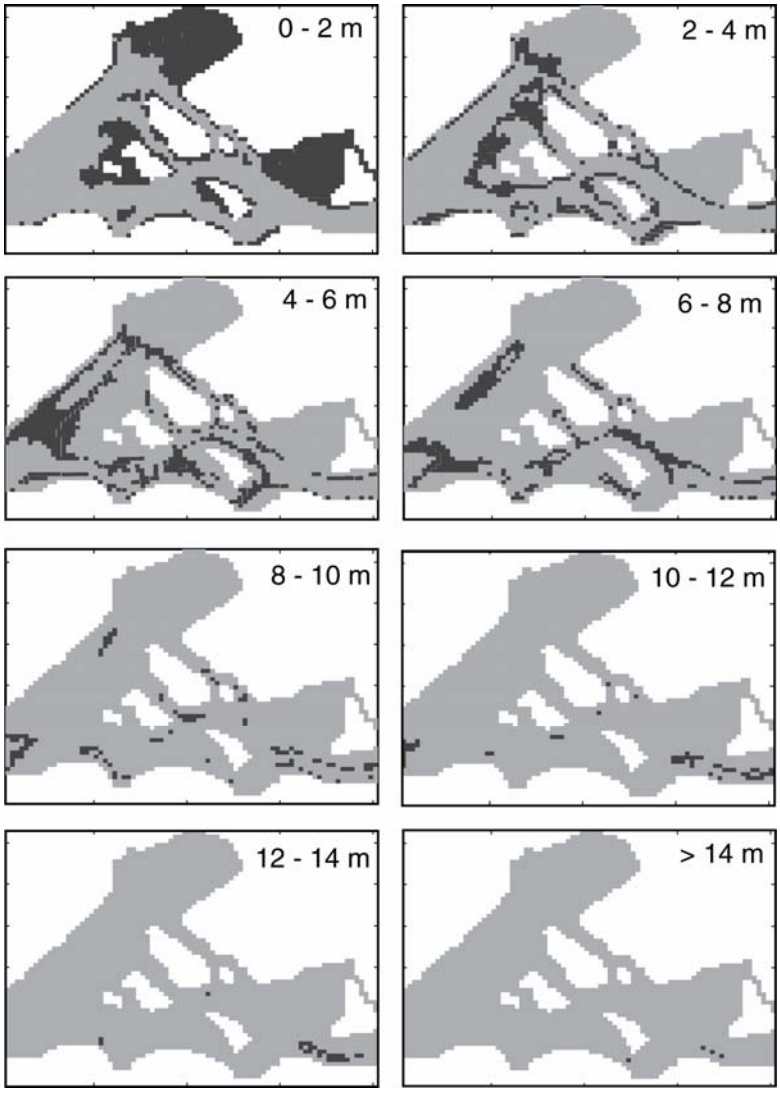

Figure 8.6 Depth ranges in Suisun Bay, referenced to MLLW. Darker areas indicate areas of specified depth range.

8.3.1.5 Sensitivity analysis

In Chapter 7 I identified the most sensitive parameters for simulation of sediment fluxes; for these simulations I must test the sensitivity to the morphological acceleration factor. The use of a morphological factor does not necessarily scale the simulation up by the value of the factor: the frequency of episodic events, relative to the regular tidal forcing, complicates the use of the factor. Additionally, for a given set of bed parameters, the

morphological factor may not scale up linearly with time (David Schoellhamer, writ. comm.). Other approaches, such as a temporally variable factor or temporal compression of riverine events (Dano Roelvink, writ. comm.), are beyond the scope of this work. Nonetheless, I can identify an optimal factor, that when used with specific sediment and forcing parameters, gives the best agreement with observed changes. Holding those parameters constant and varying the morphological factor will indicate how sensitive morphological acceleration is to model parameters. I will use additional morphological factors of 10 and 40, and compare with the initial results (morphological factor of 20, morphological hydrograph 1).

8.3.2 Results

8.3.2.1 Bathymetric change induced by composite results

The composite results of the three morphological hydrographs result in a 2.5% weighted error, relative to depth (Table 8.2). Total deposition is 0.41 m, as opposed to the measured deposition of 0.40 m. The profile of bathymetric change with depth (Fig. 8.7) suggests that minor differences in flow and sediment load timing between the morphological hydrographs are smaller than the changes brought about by the other forcings (enhanced sediment supply, wind-wave resuspension, tidal currents). Major features that are reproduced include deposition in Grizzly and Honker Bays, erosion in portions of the Reserve Fleet channel, and erosion in the landward end of the main channel (Fig. 8.8).

Table 8.2 Observed bathymetric change and modeled bathymetric change for three morphological hydrographs (MH), in depth intervals of 2 m. Mean error, in bold, is the total error of the net basin change prediction.

Depth range	Area (km^2)	Obs. change (m)	MH 1 change (m)	MH 2 change (m)	MH 3 change (m)	Mean (m)	Error (m)	Areally weighted error/depth
0-2 m	39.50 (45%)	0.25	0.27	0.14	0.20	0.20	-0.05	2.29%
2-4 m	15.20 (17%)	0.54	0.89	0.84	0.85	0.86	0.32	1.83%
4-6 m	16.60 (19%)	0.27	0.42	0.30	0.31	0.35	0.07	0.27%
6-8 m	10.10 (11%)	0.66	0.39	0.37	0.34	0.37	-0.29	0.48%
8-10 m	4.15 (5%)	1.13	1.12	1.11	1.09	1.11	-0.02	0.01%
10-12 m	1.84 (2%)	1.34	0.53	0.67	0.61	0.60	-0.73	0.14%
12-14 m	0.96 (1%)	0.13	-0.91	-0.72	-0.81	-0.81	-0.94	0.08%
>14 m	0.24 (<1%)	-0.03	-0.49	-0.37	-0.43	-0.43	-0.39	0.01%
Total	88.59	0.40	0.46	0.37	0.40	0.41	0.01	**2.50%**

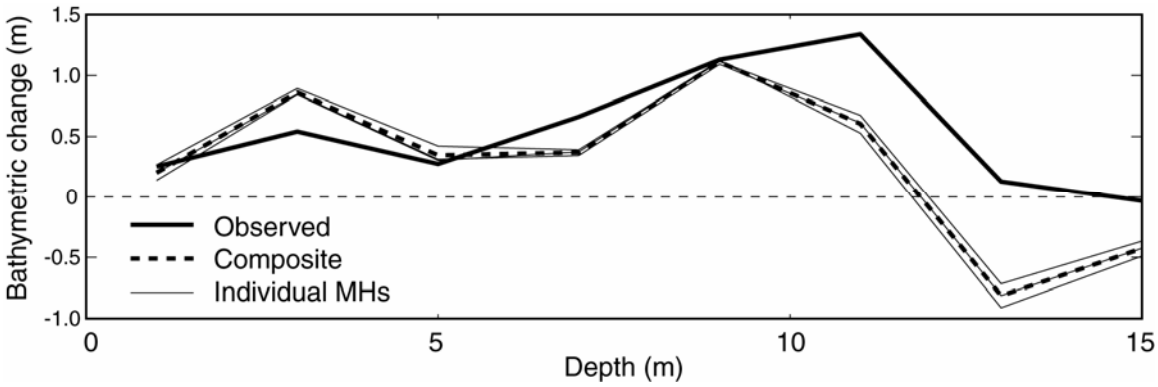

Figure 8.7 Profile of observed, composite, and individual morphological hydrograph depth changes.

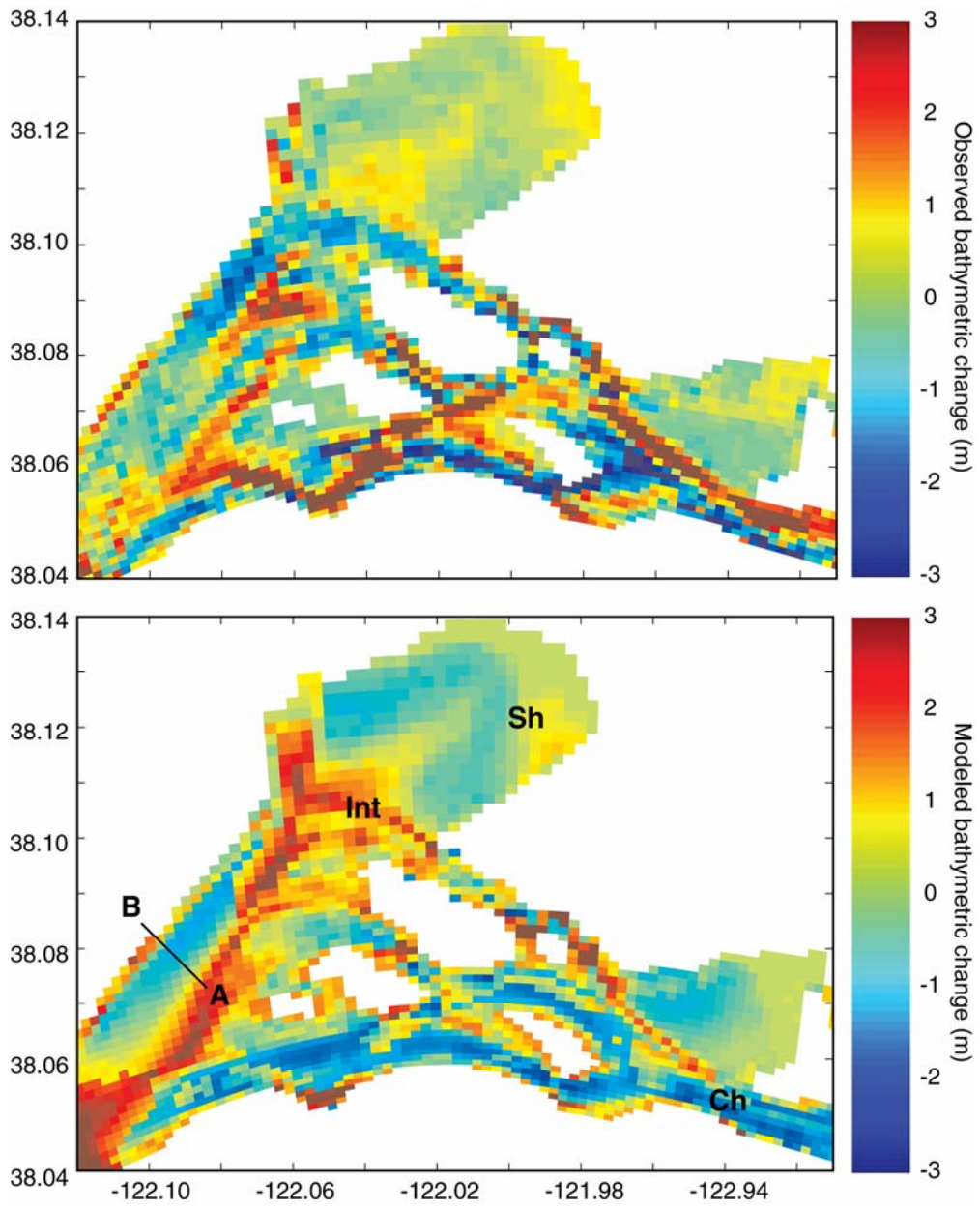

Figure 8.8 Observed and modeled bathymetric change for 1867-1887 period. Modeled change is the composite results obtained with three morphological hydrographs. Observed change results were interpolated on to the numerical grid used for this study; actual data density is substantially higher (Fig. 8.1). Locations Sh, Int, and Ch used in Fig. 8.11; cross-section AB used in Fig. 8.13.

8.3.2.2 Bathymetric change anomalies induced by each morphological hydrograph

MH 1 produces greater sediment redistribution than the composite result: channels are relatively more erosional, while deposition is enhanced on the shoulder of the Reserve

Fleet channel, and in Grizzly and Honker Bays. MH 2, which had the smallest absolute bed changes, shows less redistribution as compared to the mean: main channels are less erosional, and intermediate and shoal areas are less depositional. MH 3 produces changes that are intermediate relative to MH 1 and MH 2. It should be stressed that the relative changes between morphological hydrographs, due to differences in flow timing, are small compared to the overall changes caused by relatively high sediment supply, wind-waves, and tidal currents.

The anomaly surfaces, relative to the composite surface, all show a pronounced curved feature in Grizzly Bay, this feature is essentially the boundary between the subtidal and intertidal domain. Wetting and drying is not implemented in the model (see Section 8.4.5), therefore cells are always active. If a cell deposits enough sediment to break through the water surface, the depth is held below the water surface to prevent a model crash. The eventual effect is the creation of virtual intertidal areas. The heads of both Grizzly and Honker Bays display the creation of virtual intertidal areas, and the curved feature is the intersection between these areas and subtidal areas. Because all three morphological hydrographs produced a similar distribution of virtual intertidal areas (Fig. 8.9), the anomalies are greatest at the intersection.

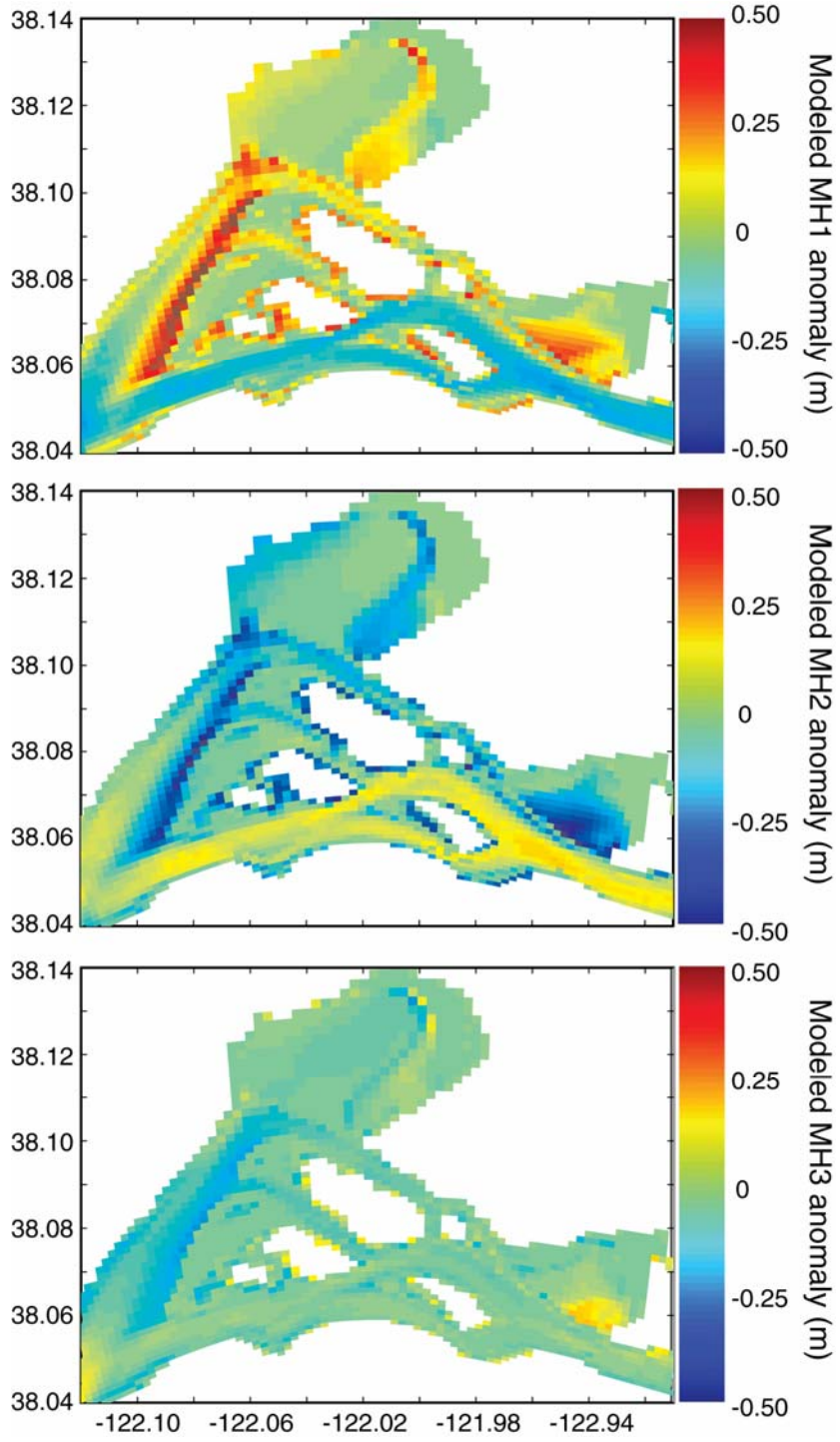

Figure 8.9 Bathymetric change anomalies for each morphological hydrograph, obtained by differencing individual and mean results. Positive values indicate deposition relative to the mean result, negative values indicate erosion relative to the mean result.

8.3.2.3 Calibration performance

Best agreement was achieved by altering bed sediment fractions and wave period. Initial runs with a spatially uniform fine/coarse distribution showed systemic erosion in deeper channels; once the distribution was rectified to reflect coarser conditions in the channel, bathymetric changes in the channels were more reasonable. Channel areas deeper than 7 m were initialized with 20/80 fine/coarse sediment distribution (as opposed to 40/60 elsewhere). Improving agreement in shallow areas (<4 m) was achieved by varying the constant wave period (to 1.425 s) when deposition was overestimated. The worst agreement, relative to depth, is in the transition zone between channel and shoal (2-4 m): these areas are not as directly susceptible to wind-wave resuspension or tidal erosion, and are more affected by exchange between shallows and channels.

Sutherland et al. (2004) detail the use of the Brier Skill Score (BSS) with regard to morphological models, including the decomposition of the BSS (Murphy and Epstein, 1989). The reader is directed to Sutherland et al. (2004) for a full description of the decomposition. Briefly, α is a measure of phase error (i.e. discrete locations of erosion and deposition) and approaches 1 for perfect prediction. Parameter β is a measure of amplitude error; perfect prediction of phase and amplitude gives $\beta=0$. Parameter γ is a measure of the mean bed change error, averaged over the domain; a value of zero indicates perfect prediction. Using the proposed provisional classification of Sutherland et al. (2004), the BSS for this effort results in an “excellent” prediction for 23% of the area, “poor” prediction for 56% of the area, and “bad” prediction for 21% of the area (Table 8.3). However, our calibration goal of representing net bed level changes is met:

the value of γ is less than 0.03 for over 80% of the domain. Sutherland et al. (2004) achieved an overall value of 0.03 for their morphological simulations. Considering the early phase of this type of investigation, this is a useful benchmark.

In the shallowest depth interval, which occupies over 40% of the area, correlation is poor, while average bed level change is excellent. Visual inspection of the observed and simulated changes (Fig. 8.8) suggests that some depositional and erosional features in Grizzly and Honker Bays are not modeled well: while observations show deposition in the northern half of Honker Bay, model results display deposition in the eastern half. In Grizzly Bay, the model shows erosion in the northwest section, while observations show little change. I have chosen to represent all areas shallower than 7 m with homogenous initial bed characteristics, and this may account for some discrepancies. There are model modifications, such as coarsening the bed in over-erosional areas, that would improve agreement, but these types of modifications cannot be justified without accompanying field data from the period of interest, which does not exist.

Table 8.3 Decomposition of Brier Skill Score by depth interval, with proposed BSS classification of Sutherland et al. (2004).

Depth interval	Percent area	α	β	γ	BSS	Classification
0-2 m	45%	0.11	0.21	0.003	0.05	Poor
2-4 m	17%	0.51	0.02	0.06	0.54	Excellent
4-6 m	19%	0.06	0.45	<0.001	<0	Bad
6-8 m	11%	0.11	0.19	0.002	0.01	Poor
8-10 m	5%	0.45	0.01	0.009	0.59	Excellent
10-12 m	2%	0.04	0.51	0.01	<0	Bad
12-14 m	1%	0.46	0.62	0.21	0.19	Fair
>14 m	<1%	0.03	0.00	0.53	<0	Bad

Classification: 1.0-0.5, excellent; 0.5-0.2, good; 0.2-0.1, fair; 0.1-0.0, poor, <0, bad.

8.3.2.4 Sensitivity analysis

Bathymetric changes in specific depth ranges varied with the value of the morphological acceleration factor (Fig. 8.10, Table 8.4), with all other parameters held constant. Doubling of the MF does not lead to a corresponding doubling of bathymetric change, due to nonlinear feedback between hydrodynamics and bathymetry. An increase in MF expectedly amplifies bathymetric changes, but this is ultimately also a function of sediment bed properties, and sediment supply. Use of a large MF is not appropriate for a system with limited sediment supply: the total accretion should not exceed the total availability of sediment from landward and seaward sources (scaled by the MF) during the simulation period. In other words, a system with a rapid decline or increase in sediment supply may not be adequately modeled with large MF.

Table 8.4 Bathymetric changes in depth intervals for three morphological acceleration factors (MF). Positive percent changes indicate more bathymetric change relative to the MF=20 case, negative percent changes less bathymetric change relative to the MF=20 case.

Depth range	MF=20 (m)	MF=10 (m)	Percent change using MF=10	MF=40 (m)	Percent change using MF=40
0-2 m	0.27	0.09	-67%	0.43	60%
2-4 m	0.89	0.67	-25%	1.11	24%
4-6 m	0.42	-0.04	-109%	0.96	128%
6-8 m	0.39	0.08	-80%	0.83	113%
8-10 m	1.12	0.75	-33%	1.64	46%
10-12 m	0.53	0.41	-23%	0.81	53%
12-14 m	-0.91	-0.64	-30%	-0.97	7%
>14 m	-0.49	-0.35	-29%	-0.39	-21%
Total	0.46	0.19	-59%	0.74	61%

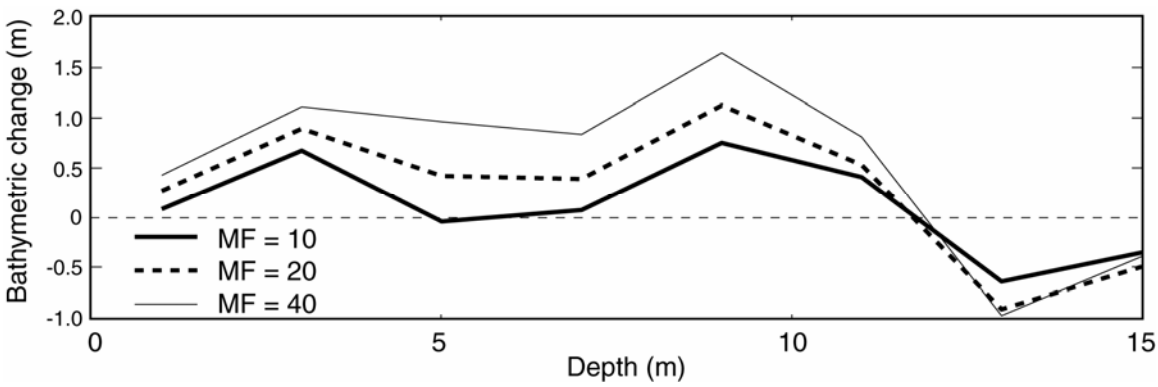

Figure 8.10 Profile of simulated bathymetric changes for three morphological acceleration factors (MF).

8.4 Discussion

8.4.1 Mechanism for bathymetric change patterns

The primary mechanism for the net observed and modeled bathymetric change is the increased delivery of watershed sediment during hydraulic mining. Wind-wave resuspension and tidal processes are largely responsible for the spatial distribution of bathymetric changes: this is evident from the relatively small changes between morphological hydrographs (due to flow timing), as opposed to the larger changes in net bathymetric change for the composite result (e.g. Fig. 8.7). Episodic freshwater flow and sediment delivery tend to scour the main channel, and deposit sediment in adjacent intermediate depth (2-6 m) areas (Fig. 8.11). Shoal areas (< 2 m) are relatively unaffected by episodic flow peaks, but respond instead to wind-wave resuspension. Transfer of sediment between intermediate depth and shoal areas during the wind-wave season leads to shoal erosion and intermediate area deposition.

With other forcings held constant, water years with large peak flows tend to cause greater redistribution than water years with lower peak flows. The three morphological

hydrographs chosen for this hindcasting effort represent typical conditions in terms of flow timing, magnitude, and sediment supply during the late 19th century. However, there are differences between those hydrographs in terms of peak flow, total flow, and total sediment load. Those differences are represented in the bathymetric change anomalies (Fig. 8.9). In terms of peak flow, MH 1 had the largest peak (Table 8.5; Fig. 8.5), followed by MH 3, and MH 2 had the smallest peak. Because of a large flow peak, MH 1 produces greater sediment redistribution than the other morphological hydrographs. Deposition in channel-adjacent areas in Grizzly and Honker Bays is enhanced for the MH 1 simulation, relative to the composite. While wind-wave resuspension and tidal currents are the primary forcings, peak flow magnitude is clearly capable of altering redistribution as well.

Table 8.5 Flow, sediment load, and bed change characteristics of three morphological hydrographs.

Morphological hydrograph	Peak flow (m^3/s)	Sediment load (Mt)	Net bed change (m)	Mean absolute value of bed change (m)
1	7553	12.3	0.46	0.87
2	5023	9.6	0.37	0.78
3	5999	9.6	0.40	0.81

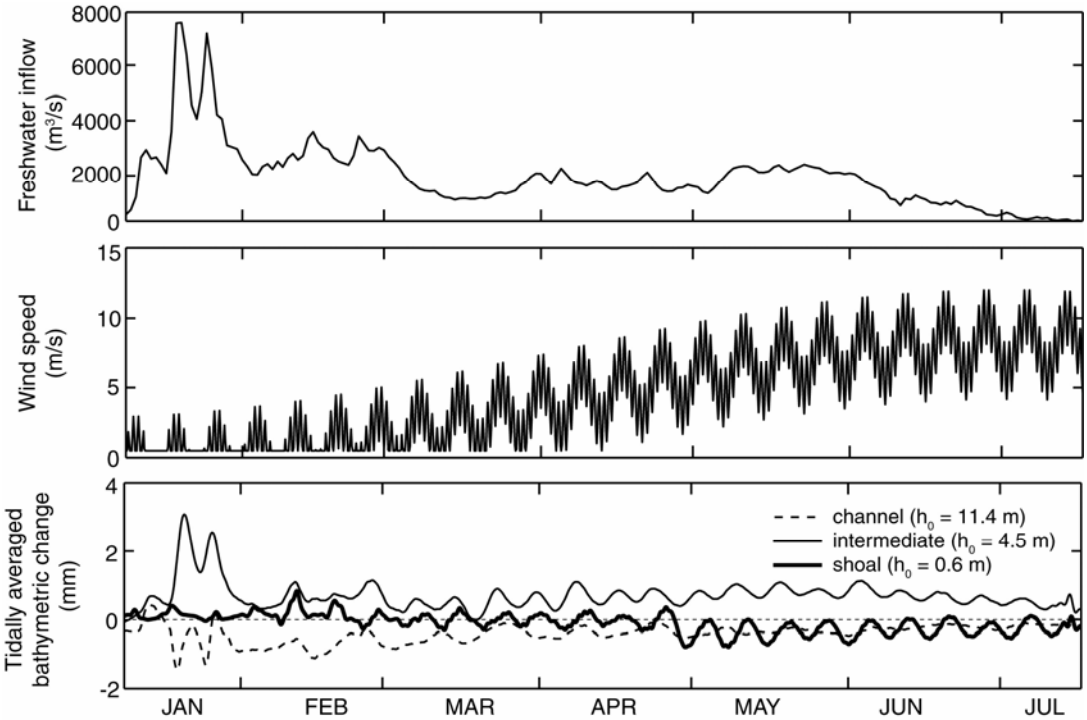

Figure 8.11 Freshwater inflow (MH 1), wind speed, and tidally averaged bathymetric changes (in 15 min intervals) for three depth regimes of Suisun Bay (marked in Fig. 8.8): channel (Ch, landward end of main channel), intermediate (Int, mouth of Grizzly Bay), and shoal (Sh, head of Grizzly Bay).

8.4.2 Importance of parameterizing major forcings

The bathymetric changes induced by the different morphological hydrographs are greater than the changes between the individual simulations: this suggests that the timing and magnitude of freshwater flows are secondary to the net sediment supply, tidal energy, and wave energy. For a non-stationary situation such as intense hydraulic mining, it can be expected that the most of the bathymetric change is induced by the dominant forcing. In this case, that is the enhanced sediment supply from the watershed. The sediment load estimates of Gilbert (1917), Porterfield (1980), and Ganju et al. (in review) provide the most important set of data needed for this modeling endeavor. Tidal and wave energy, though variable on the decadal-timescale, can be approximated using idealized functions

with relative success. Because sediment supply was more variable than these forcings, it is necessary to estimate sediment loads in a more robust manner, as done by those previous researchers. Once a reasonable set of morphological hydrographs are selected, and appropriate sediment rating curves applied, the net bathymetric result will respond to the net sediment loads provided as a landward boundary condition.

8.4.3 Concept of morphological hydrograph

Use of the morphological hydrograph has greatly reduced input needs and computational expense for this effort. As stated in the previous section, bathymetric change during hydraulic mining was more sensitive to net sediment loads than specific hydrograph shape. Nonetheless, it is evident that performance is sensitive to peak flow (Table 8.5). Following the concept of the morphological tide, there is a reduced set of hydrographs that will yield the same geomorphic result as the full set (within some specified error). Using the measured bathymetric change of Cappiella et al. (1999) as the specific goal, the use of three morphological hydrographs is capable of generating reasonable bathymetric changes. The ideal test of the morphological hydrograph would be comparing the continuous simulation result (with the real set of hydrographs) to the composite, morphologically accelerated simulation results. However the computational expense is too great for this type of simulation, and I must instead rely on a comparison to measured bathymetric change as a test of the method.

When considering the selection of the morphological hydrographs, it is critical to consider the type of climatic condition that the hydrograph represents. Using MH 3 as a

reference, MH 1 and MH 2 represent more and less volatile hydrographs, respectively. MH 1, with a large, early peak flow, produces greater redistribution overall (Fig. 8.12) and greater deposition on channel flanks (Fig. 8.13). MH 2, with a later, smaller peak flow, shows less redistribution and less deposition on channel flanks, as compared to MH 3. Ideally, one must represent the distribution of water year types when selecting morphological hydrographs. With regards to climate change, a trend towards earlier, larger flow peaks (e.g. Knowles and Cayan, 2002) would tend to create greater sediment redistribution than later, smaller flow peaks.

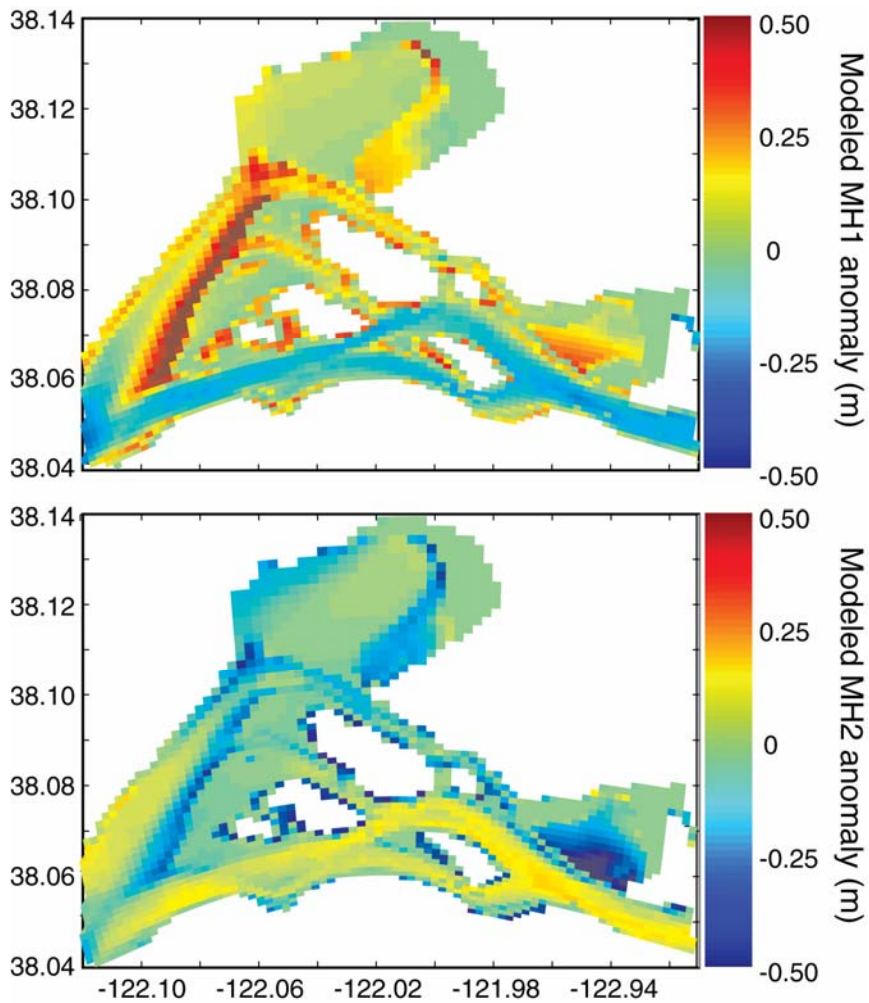

Figure 8.12 Bathymetric change anomalies of MH 1 and MH 2, as compared to MH 3.

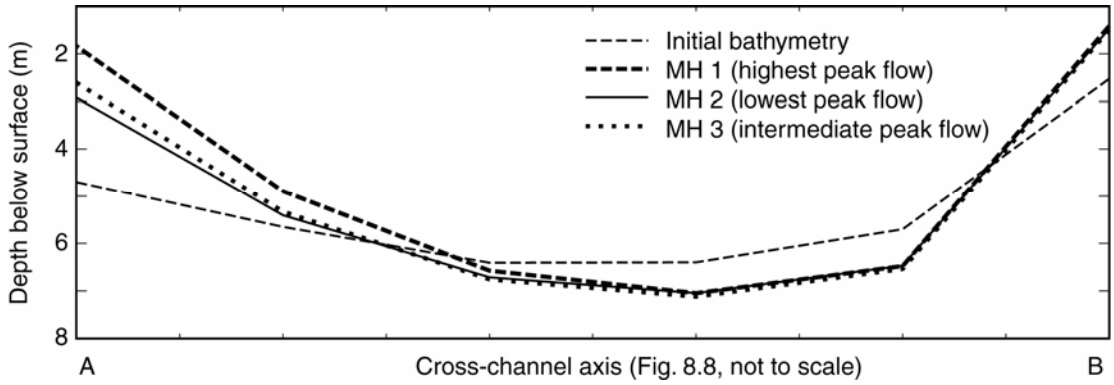

Figure 8.13 Bathymetric change of a cross-section of the Reserve Fleet Channel (Fig. 8.8), for three morphological hydrographs.

8.4.4 Morphological acceleration factor in non-stationary systems

In non-stationary systems, the morphological acceleration factor must be used with caution. For example, I have simulated the 1867-1887 period using a factor of 20. This is appropriate because the dominant forcing, sediment supply, was large and relatively constant during this period. However, if I wished to model 1867-2007 as a one-year simulation (using a factor of 140), I would likely overestimate deposition, as the sediment supply has decreased drastically since 1887. Therefore the morphological acceleration factor can only represent the time period over which the dominant forcings are relatively constant. To extend a simulation to 2007, I would need to begin a new simulation starting in 1887, with a new set of morphological hydrographs that represent a reduction in watershed sediment supply. I can apply a morphological acceleration factor equivalent to the timescale of constant forcing. In highly variable systems, where forcings may vary on annual timescales, the morphological acceleration factor may be inappropriate.

8.4.5 Morphological acceleration, episodic forcing, and wetting and drying

Preliminary simulations with the morphological acceleration factor and wetting/drying module indicated a fundamental difficulty in episodic systems, such as Suisun Bay. In the early portion of the simulation, during the episodic sediment delivery, large depositional features grew in Grizzly and Honker Bays, eventually becoming dry (i.e. land cells). The accelerated morphological change caused these features to grow at a 20-fold rate, as desired. However, as the dry cells were converted to zero-flux boundaries, flow patterns within the shallows were altered, creating minor channels in the shoals that do not appear with the non-wetting/drying simulation. Though the depositional features eroded as the

wind-wave season commenced, the fundamental changes in channel patterns were noticeable, and did not agree with observations. Therefore it was decided to not utilize wetting and drying in the final simulations. Allowing fluxes to and from all cells during these simulations was necessary to keep these artifacts from appearing.

8.4.6 Evaluating performance

Simulating geomorphic change or any parameter with dense spatial coverage must be evaluated in some consistent, quantitative manner, as suggested by Sutherland et al. (2004). Visual comparison of observed and modeled changes is not sufficient and is prone to both intentional and unintentional distortion. Use of the decomposed Brier Skill Score appears to be a valuable tool to evaluate performance. The three main parameters quantify errors in phase, amplitude, and net bed level; the modeler can determine beforehand which characteristic is of greatest importance. In this effort, I determined that net bathymetric change in the shallowest 2 m was of greatest relevance, due to the ecological importance of these areas. While I have failed to get adequate agreement in phase (i.e. discrete locations of erosion and deposition), I did achieve satisfactory agreement in net deposition over those areas. Surprisingly, the BSS for the 2-4 m depth interval was excellent, but the error in net deposition (relative to depth) was the greatest. In reality, the BSS does not take into account the actual depth: an error of 0.1 m in 10 m of water is given the same importance as an error of 0.1 m in 1 m of water. My alternative quantification method factors in the importance of water depth in assessing the performance of morphological models (Table 8.2), and can be used in conjunction with the BSS.

8.5 Conclusion

In this chapter I successfully calibrated the model to decadal-timescale bathymetric change in Suisun Bay, with the use of a more advanced wind-wave module and innovative time-stepping techniques: the morphological hydrograph and morphological acceleration factor. Values that were modified include bed sediment parameters and wave period; these modifications are warranted because the 1867-1887 period is a different temporal period than the modern simulations of the last chapter, and in this chapter I use a different wind-wave module which allows for feedback between geomorphic evolution and the calculated wave height.

Hindcasting estuarine bathymetric change is a computationally and data intensive endeavor, that requires adequate calibration data, idealization of boundary conditions, and innovative input reduction techniques. I have performed a successful hindcast of bathymetric change in Suisun Bay, between 1867-1887, when sediment supply was increased due to hydraulic mining. The observations of Cappiella et al. (1999) provide a bathymetric change data set for calibration purposes. Major idealizations used include synthetic functions for seaward SSC, wind speed, and salinity. Computational expense is reduced through the use of a morphological acceleration factor, that scales tidal-timescale bed changes by a constant value, and updates the bathymetry within the model. Reconstruction of historical freshwater flows and sediment loads led to the identification of a limited set of hydrographs, known as morphological hydrographs, which provide the same bathymetric change as the set of real hydrographs. Performance of the model is quantified by comparing observed net depth changes, in specific depth intervals, with

simulated depth changes. Each morphological hydrograph is modeled separately, and the results are composited. Mean error was 2.5%, while the areally weighted error as a percentage of depth, 2.29% was greatest in the shallowest 2 m of water (i.e. error of 0.029 m in 1 m of water). Qualitative patterns of erosion and deposition within Suisun Bay are also modeled well. Performance is also evaluated using the Brier Skill Score (BSS), though this does not adjust error relative to depth. Decomposition of the BSS, over depth intervals, is a useful tool for evaluating performance in different depth regimes. This modeling framework provides a quick and robust approach for simulating geomorphic change in estuaries, especially when computational power and data availability are limited.

9 Objective E: Application of calibrated model to future scenarios

9.1 Introduction

In the previous chapters I established the validity of my approach towards modeling sediment transport on the tidal, annual, and decadal-timescale. With this tool, I can now simulate changes in geomorphology in response to future scenarios, including climate change, sea-level rise, and decreased watershed sediment supply. The primary effects of climate change on Suisun Bay are the alteration of the freshwater flow hydrograph (Knowles and Cayan, 2002), and sea-level rise (Ryan et al., 1999). Climate simulations have demonstrated that a moderate warming over California will lead to decreased snowpack, causing earlier and flashier flows. Continued warming throughout the world, combined with polar icecap loss, will increase the volume of the world's oceans, and increase sea level. In addition to these climatically induced changes, an ongoing decrease in sediment supply from the Central Valley and Sierra Nevada (Wright and Schoellhamer, 2004) may be a signal of equal or greater relevance. The results of the previous chapter show that net sediment load induces greater changes in bathymetry than shape of the hydrograph, so it is necessary to include a scenario of decreasing sediment supply.

To my knowledge, there have been no previous studies evaluating estuarine geomorphic response to climate change, but it is possible to infer what changes may be induced by climate change and decreasing sediment supply. A flashier hydrograph will alter the seasonal pattern of sediment transport, by transporting more sediment seaward earlier in the water year. Dry season landward transport may increase and move further landward

in response to decreased dry season freshwater flows. Therefore seasonal patterns of sediment transport will be intensified, thereby intensifying seasonal changes in geomorphic change. Water management effects, however, may trump natural hydrograph changes.

Sea-level rise will push the salinity intrusion limit landward, turning all portions of the estuary saltier. This may also intensify gravitational circulation and landward sediment transport, shifting depositional patterns landward. An increase in sea-level rise will also slightly alter the wind-wave resuspension patterns, especially in shallower areas. The relationship between water depth and wave-induced bottom orbital velocity dictates a decrease in energy transferred to the sediment bed. Overall, this will move the cross-shore profile of erosion and deposition landward. In areas with fringing mudflats and tidal wetlands, this sediment transport feature may be critical to the survival of intertidal areas.

The most certain change in future conditions may be watershed sediment supply. Since the peak in sediment loads during hydraulic mining in the Sierra Nevada, a persistent decrease in sediment loads from the Central Valley has been observed by several researchers. The most recent study, by Wright and Schoellhamer (2004), noted a 50% decrease in sediment supply from the Sacramento River from 1957 to 2004. This trend is largely attributed to a reduction in available mining debris and sediment trapping in reservoirs behind dams. As this trend continues, sediment supply may continue to decrease. This will increase the importance of seaward sediment supply from San Pablo

Bay to Suisun Bay for maintaining elevation. Nonetheless, a reduction in watershed sediment supply will ultimately lead to a relative increase in erosion throughout San Francisco Bay.

9.2. Methods

9.2.1. Modeling domain

The modeling domain for these simulations is identical to that of Chapter 7: the 1990 bathymetry with the modern idealized Delta geometry. Conceptually, this simulation will represent the 1990-2010 period, under normal conditions (scenario B) or 2030 conditions (scenarios WS, DS, WDS, below). The results of these simulations will be expressed as differences between scenarios, not absolute predictions. Therefore changes between results will be due to the effect of the altered forcing in each scenario. A sensitivity analysis will establish the validity of scenario modeling with uncertain parameters.

Table 9.1 Model parameters for future scenario simulations.

Model parameter	Value
# of x-direction cells, size range	160, 72 – 394 m
# of y-direction cells, size range	87, 102 – 593 m
# of z-direction cells	4
baroclinic time step	40 s
barotropic time step	2 s
simulation steps	788400
settling velocity	0.10/0.25 mm s^{-1}
erosion rate	$2x10^{-5}$ kg m^{-2} s^{-1}
critical stresses	0.10/1.0 N m^{-2}
porosity	0.60
bed density	2000 kg m^{-3}
initial bed thickness	2.0 m
wave period	1.425 s
wave fetch	20 km
water depth (for wave model)	evolving bathymetry
tidal boundary velocity, stage	Flather (radiation)
river boundary velocity, stage	Flather (radiation)
tidal boundary tracers	clamped
river boundary tracers	clamped
morphological acceleration factor	20

9.2.2. Implementation of landward and seaward boundary conditions

9.2.2.1 Scenario B: base-case

Landward boundary conditions

Using the concept of the morphological hydrograph, three years are selected to represent the 1990-2010 period: a dry year (2001), a moderate year (1999), and a wet year (2006) (Table 9.2; Fig. 9.1). These years were selected based on peak flows and sediment loads: the average of the peak flows and sediment loads of 1999, 2001, and 2006 are close to the average peak flows and sediment loads of the 1990-2006 period. This provides a low, middle, and high sediment load morphological hydrograph. As seen in Chapter 8, total load and peak flow magnitude are the features of greatest relevance for simulating estuarine geomorphic change, therefore the use of three morphological hydrographs that

span these extremes is sufficient. The measured sediment loads of the Sacramento and San Joaquin rivers will be specified at the boundary.

Table 9.2 Total and peak flow and sediment load characteristics of morphological hydrographs and represented period (1990-2006).

Period	Yearly total flow (10^9 m^3)	Peak flow (m^3/s)	Yearly sediment load (Mt)
MH1 (1999)	27.80	4054	2.02
MH2 (2001)	8.56	1600	0.75
MH3 (2006)	54.03	11538	3.65
Average of MHs	30.13	5730	2.14
Average of 1990-2006	23.74	5133	2.22

Seaward boundary conditions

Seaward tides and water velocities are provided by the same harmonic predictions used in prior simulations (Sec. 7.3.1.2.2). Seaward salinity is computed using the same salinity gradient-flow relationship detailed in Section 7.3.1.2.2. The synthetic SSC function is again specified as a combination of flow, wind, and tidal signals (Sec. 7.3.1.2.2).

9.2.2.2 Scenario WS: warming and sea-level rise by 2030

Landward boundary conditions

The three morphological hydrographs can be scaled to represent the warming conditions modeled by Knowles and Cayan (2002). Simulations of 1967-1987 flows, with 1967-1987 precipitation and 2030 temperature conditions, were compared to the same flows adjusted to 2000 temperature conditions. This provides a scaling curve for the hydrograph that modulates a current hydrograph to 2030 conditions. All three morphological hydrographs were scaled using this curve (Fig. 9.1). Again, the measured sediment loads of the Sacramento and San Joaquin Rivers will be specified at the

boundary. Total yearly sediment input is conserved with this approach, the only difference is the timing and magnitude of the flows and sediment loads. The changes in flow timing and magnitude by 2030 are minor compared to the changes in sediment load generated in the following scenarios. This approach does not take into consideration management response to the altered snowpack regime.

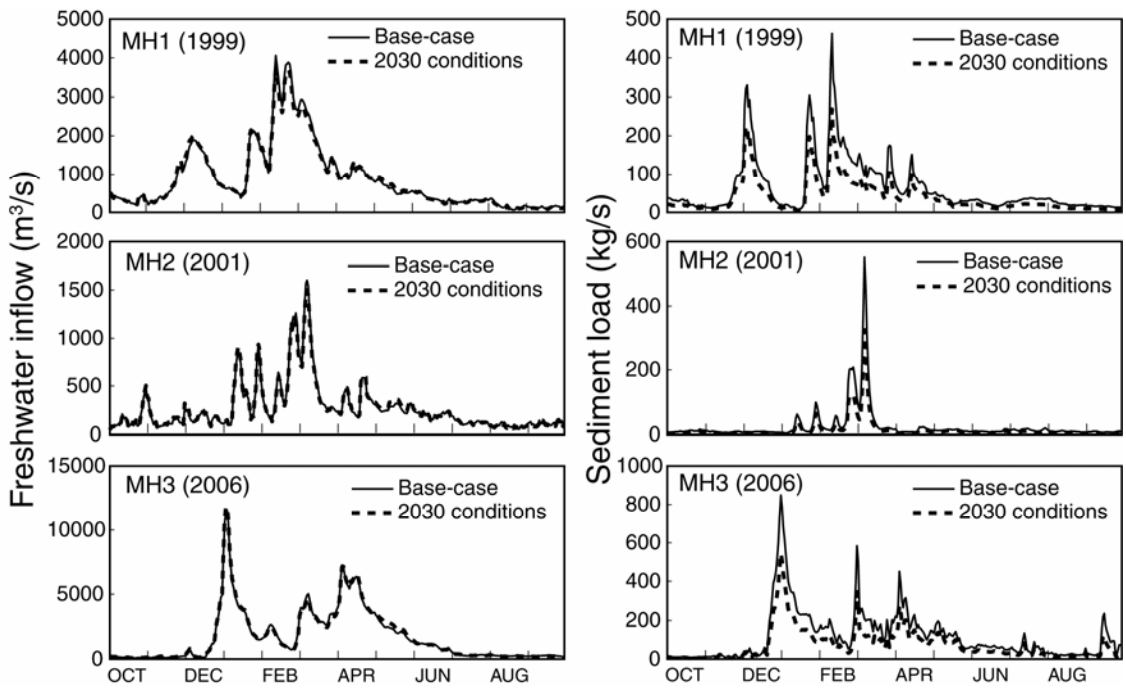

Figure 9.1 Hydrographs and sediment loads for base-case and 2030 conditions, for three morphological hydrographs (1999, 2001, 2006).

Seaward boundary conditions

The only modification made at the seaward boundary for this simulation is the addition of 0.06 m to the tidal elevation time-series, at the seaward boundary, to represent sea-level rise by 2030. This is a relatively conservative estimate, based on the current trend of 0.002 m/y (over a 30 y period) at the Golden Gate. It may be possible that the relationship between freshwater flow and salinity gradient established earlier may change

with sea-level rise; however there are no data or simulation tools available to estimate this change. The increase in water level at the seaward boundary should represent the possible increased salt intrusion adequately.

9.2.2.3 Scenario DS: decreased sediment supply and sea-level rise by 2030

Landward boundary conditions

Using the base-case hydrographs (no warming signal), I alter the sediment loads to represent a decrease in sediment supply by scaling the SSC boundary condition. To estimate the reduction in sediment supply, I extend the decrease identified by Wright and Schoellhamer (2004), which was 50% in 44 y, to a period 30 y in the future. This method yields a decrease of 34% over the next 30 y, and this factor is applied to the measured sediment load time-series (Fig. 9.1).

Seaward boundary conditions

The sea-level rise changes made in the previous section are retained here, and I modulate the seaward SSC function to represent a decrease in watershed sediment loads, as described in Section 7.3.1.2.2.

9.2.2.4 Scenario WDS: warming, decreased sediment supply, and sea-level rise by 2030

Landward boundary conditions

For this simulation the modified hydrographs (warming signal), along with the decreased SSC boundary condition are used (Fig. 9.1).

Seaward boundary conditions

The sea-level rise changes and seaward SSC changes made in the previous section are retained here.

9.2.3 Sensitivity analysis

The goal of scenario modeling is not predicting absolute bathymetry, but changes in depth distribution due to warming, sea-level rise, and decreased sediment supply. Therefore the goal of the sensitivity analysis is to compare changes between two scenarios with the original parameters, and changes between the two scenarios with perturbed parameters. If the changes are similar, then incorrect parameter specification has a minor effect on the changes between scenarios of geomorphic change.

Sensitivity analyses on one major parameter for both the scenario B (base-case) and scenario WDS (warming, decreased sediment supply, sea-level rise) can be performed following Section 3.5. The difference between the base-case and future scenario with original parameters, and perturbed parameters will be compared (Eq. 3.3). This relationship may vary depending on the size of the perturbation. Here I use wave energy (in terms of wave period) as the parameter of choice. Previously, I established that sediment fluxes were most sensitive to this parameter, therefore this is the most stringent test. Wave period will be decreased by 10% (favoring deposition), and morphological hydrographs for the scenario B and scenario WDS will be simulated.

9.3 Results

9.3.1 Specific and Bulk changes in sedimentation for each scenario

9.3.1.1 Scenario B: differences between morphological hydrographs

The composite net bed level change for the three morphological hydrographs was 0.163 m (Table 9.3), with individual changes of 0.09 m (2006), 0.12 m (1999), and 0.27 m (2001). Net deposition was a function of peak and total freshwater flow, with the driest year (2001) being the most depositional. For all three morphological hydrographs, deposition was observed in all depth ranges shallower than 11 m (Fig. 9.2). Deeper areas were more erosional in the wettest year (2006). The composite result is closest to the intermediate year (1999), similar to the result from Chapter 8. The largest area in terms of depth interval, 0-2 m, was slightly depositional for all three morphological hydrographs and the composite result.

Anomalies of modeled change (Fig. 9.3) suggest that dry years favor enhanced deposition in the seaward portions of Suisun Bay, while wet years favor enhanced deposition in the landward portions of Grizzly and Honker Bays. Channels are relatively more erosional in the wet year (MH3), and more depositional for the dry year (MH2).

Table 9.3 Bed level (BL) and relative water depth (RWD) changes for all scenarios. Positive BL values indicate deposition, positive RWD values indicate deepening, with sea-level rise included.

Depth range	Area (km^2)	Sc. B BL (m)	Sc. WS BL change (m)	Sc. WS RWD change (m)	Sc. DS BL change (m)	Sc. DS RWD change	Sc. WDS BL change (m)	Sc. WDS RWD change (m)
0-2 m	45.72 (48%)	0.018	0.026	0.034	0.019	0.041	0.018	0.042
2-4 m	13.08 (14%)	0.366	-0.003	0.063	-0.014	0.074	-0.017	0.077
4-6 m	11.98 (13%)	0.192	-0.013	0.073	-0.029	0.089	-0.031	0.091
6-8 m	8.05 (11%)	0.329	-0.007	0.067	-0.030	0.090	-0.032	0.092
8-10 m	6.65 (7%)	0.481	0	0.060	-0.027	0.087	-0.028	0.088
10-12 m	5.15 (5%)	0.320	0.003	0.057	-0.035	0.095	-0.034	0.094
12-14 m	2.17 (2%)	0.167	-0.006	0.066	-0.029	0.089	-0.029	0.089
14-16 m	1.12 (1%)	-0.189	-0.010	0.070	-0.031	0.091	-0.030	0.090
16-18 m	0.73 (<1%)	-0.215	-0.013	0.073	-0.030	0.090	-0.030	0.090
18-20 m	0.13 (<1%)	0.697	-0.041	0.101	-0.026	0.086	-0.033	0.093
Total	94.76	0.163	0.010	0.050	-0.004	0.064	-0.005	0.065

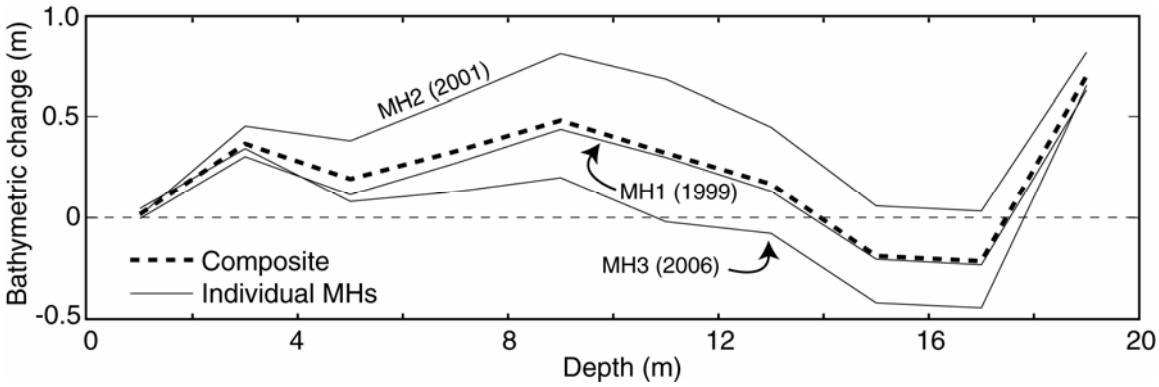

Figure 9.2 Bathymetric changes, by depth interval, induced by the morphological hydrographs for scenario B, and the composite result.

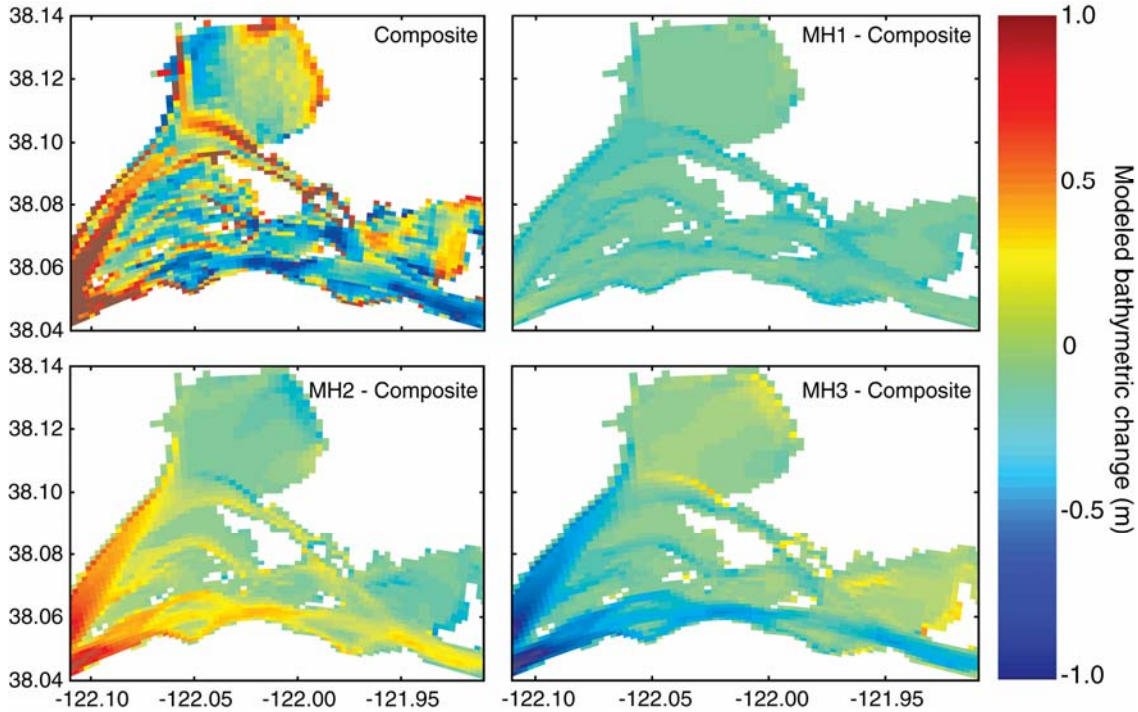

Figure 9.3 Composite bathymetric change result, and anomalies (as compared to composite) of the three morphological hydrographs.

9.3.1.2 Scenario WS: effect of warming and sea-level rise

Slight changes in the hydrograph and a step-increase in sea-level rise induced an increase in net deposition, and bed level, of 0.01 m. However, relative water depth increased by 0.05 m, indicating an overall deeper estuary, due to sea-level rise. The bed level changes, as a function of depth, suggest that sea-level rise (the dominant forcing in this scenario) induces more deposition in shoal areas (+0.026 m in the 0-2 m depth interval), and less deposition in all other areas. However, in order to keep pace with the prescribed rise in sea-level, bed level change would need to average 0.06 m over the entire domain. The net increase in deposition of 0.01 m suggests that sediment supply cannot maintain elevations relative to sea-level rise.

While the expanses of Grizzly and Honker Bays show an increase in deposition, the shallowest fringes of Grizzly Bay are less depositional in this scenario. Increases in water level reduce the effect of wind-wave resuspension, as areas become deeper and less susceptible to bottom shear caused by wave orbital velocities. The changes in water level, in Grizzly Bay, led to a 9% reduction in peak wave orbital velocity (from 0.119 m/s to about 0.108 m/s), during the summer months. Therefore less redistribution, and more deposition are observed in the areas most susceptible to wind-wave resuspension.

9.3.1.3 Scenario DS: effect of decreased sediment supply and sea-level rise

A reduction in watershed sediment supply, coupled with sea-level rise, led to 0.004 m less deposition than scenario B and 0.014 m less deposition than scenario WS. Relative water depth increased by 0.064 m, due to reduced deposition and sea-level rise. The increase in sea-level (and decrease in wave orbital velocities) still increased deposition in the shallowest depth interval, but a reduction in sediment supply from the watershed and seaward sources decreased deposition in all other areas of Suisun Bay, nearly uniformly in areas deeper than 4 m (Table 9.3).

Reducing watershed sediment supply, while keeping other forcings constant, decreases net sediment transport into Suisun Bay from the landward end, leading to decreased deposition. The effect of reduced watershed sediment supply was greatest for the MH 3 simulation (24% reduction in deposition), which had the largest sediment load, and the smallest effect was observed during the MH 2 simulation (4% reduction in deposition), which had the lowest sediment load. The seaward SSC boundary condition, which is

partially a function of watershed sediment supply (Section 7.3.1.2.2, Eq. 7.11), is reduced for the decreased sediment supply scenario, and therefore leads to a decrease in deposition at the seaward end of Suisun Bay (Fig. 9.4).

9.3.1.4 Scenario WDS: effect of warming, decreased sediment supply, and sea-level rise

The combined effect of warming, decreased sediment supply, and sea-level rise led to a net decrease in deposition, from scenario B, of 0.005 m. Relative water depth increased by 0.065 m. The shallowest 2 m of Suisun Bay were still more depositional, while all other intervals were less depositional. The overall change in net deposition between scenario DS and this scenario is 0.001 m, and is attributed to increased seaward flow velocities during the episodic freshwater flows. The minor differences between this scenario and scenario DS, which are caused by the altered timing and magnitude of freshwater flows, are discussed below. It should be noted that this change is less than 1% of the net bed change in the simulation.

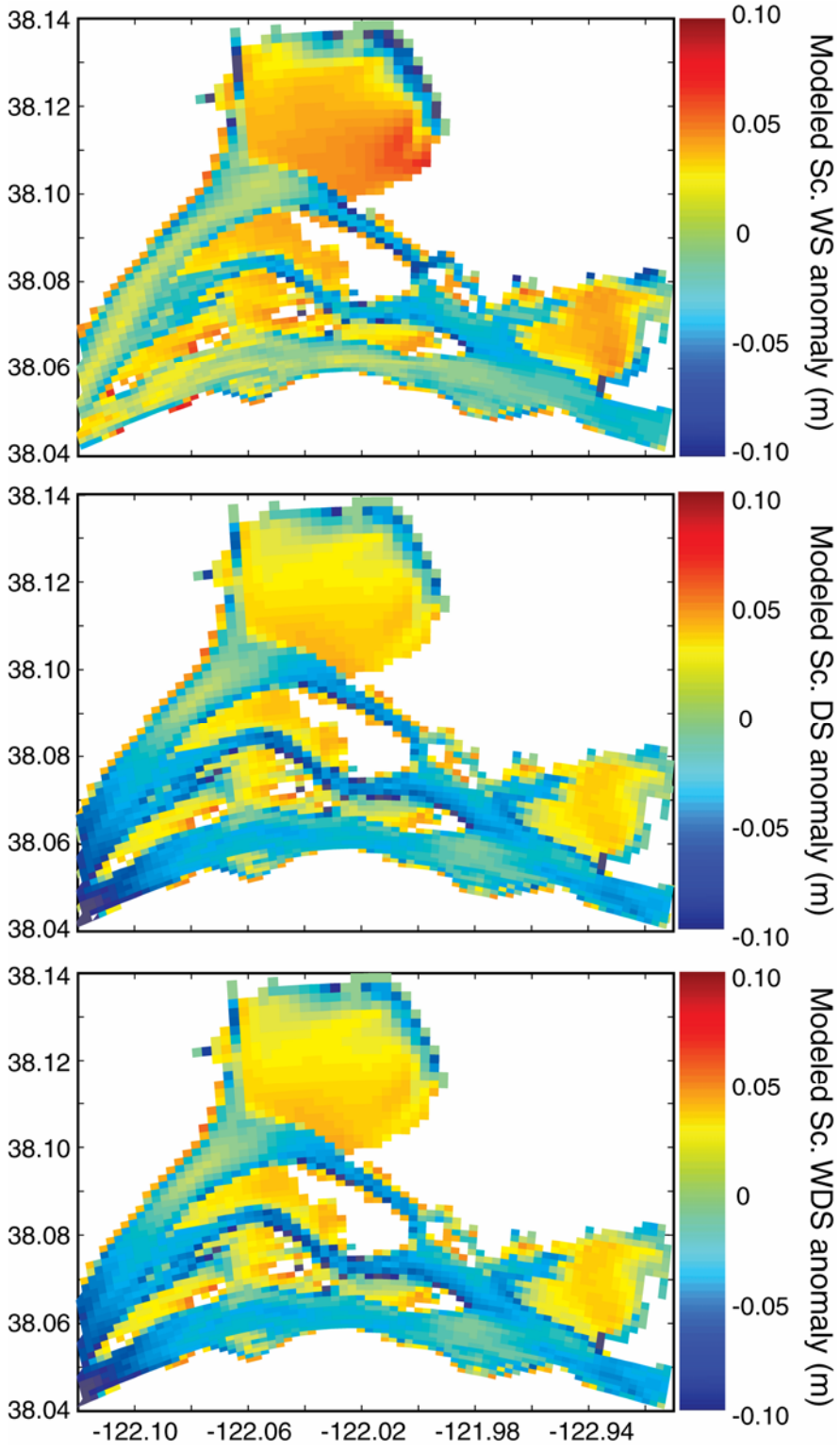

Figure 9.4 Anomalies, relative to the base-case simulation, of bed level change for three scenarios. Positive values indicate increased sediment mass on the bed for the scenario, relative to the base case.

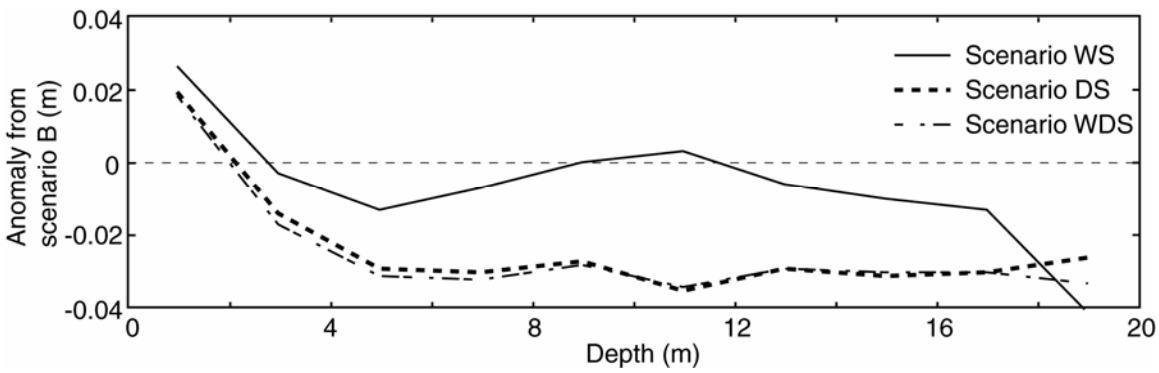

Figure 9.5 Anomaly of bed level changes, by depth interval, between the base scenario and the three future scenarios. Results are the composite of three morphological hydrographs for each scenario.

9.3.2 Sensitivity analysis

A 10% decrease in wave period results in a bathymetric difference change between scenario B and WDS of -0.003 m, over the entire domain (Table 9.4). The largest effect is seen in the 0-2 m depth interval, suggesting that relationship between wave energy, bottom shear stress, and subsequent transport is most critical in the shallowest depths. It should be noted that these changes are all less than 0.01 m, over a 20 y morphologically accelerated simulation. Sutherland et al. (2004) cite bathymetric measurement errors ranging between 0.026 and 0.1 m for modern surveys. The net difference of 0.003 m over 20 y is well below the error of measurements, and is therefore considered reasonable. This exercise indicates that uncertainty in modeling parameters, when evaluating differences between scenarios, creates errors that are still substantially less than other typical sources of error, such as field measurement.

Table 9.4 Sensitivity analysis results, comparing non-perturbed and perturbed simulations (scenario B and WDS), with wave period perturbed by a 10% decrease.

Depth range	Area (%)	$\Delta h(\xi)$ (m)	$\Delta h(\xi+\xi')$ (m)	Change (m)
0-2 m	48%	0.018	0.009	-0.009
2-4 m	14%	-0.017	-0.021	-0.004
4-6 m	13%	-0.031	-0.023	+0.008
6-8 m	11%	-0.032	-0.026	+0.006
8-10 m	7%	-0.028	-0.025	+0.003
10-12 m	5%	-0.034	-0.033	+0.001
12-14 m	2%	-0.029	-0.028	+0.001
14-16 m	1%	-0.030	-0.031	-0.001
16-18 m	<1%	-0.030	-0.031	-0.001
18-20 m	<1%	-0.033	-0.031	+0.002
Total	100%	-0.005	-0.008	**-0.003**

9.4 Discussion

9.4.1 Comparison of dry and wet year bathymetric change

Greater deposition is observed in dry years because the seaward source of sediment, San Pablo Bay, is relatively more important when freshwater flows are decreased. Despite a decreased seaward SSC boundary condition in dry years (Section 7.3.1.2.2), the other contributors to seaward SSC (wind-wave and tidal energy) remain, and allow for significant landward sediment transport. Watershed sediment loads are in decline (Wright and Schoellhamer, 2004), while San Pablo Bay has a pool of available sediment (Jaffe et al., 2007). In dry years, landward transport becomes more important and Suisun Bay turns more estuarine: the seaward end of Suisun Bay becomes more depositional, and watershed sediment loads become less important. In wet years, Suisun Bay becomes more riverine: seaward residual velocities are increased, contributing to greater total sediment export during episodic freshwater flows. Those flows are nonetheless capable of redistributing sediment towards the off-channel shoals, which are relatively more depositional during wet years. If future climatic changes induce prolonged wet or dry

periods, this will change the relative importance of seaward and watershed sediment sources.

9.4.2 Effect of sea-level rise: scenario B vs. scenario WS

Sea-level rise, prescribed at the seaward boundary, propagates through the domain and deepens the estuary. While wave propagation in an irregularly shaped estuary is complex, a relative deepening should reduce bottom orbital velocities (which reduces resuspension). Depending on the wave model used, the geomorphic response will vary. With the simple wave model used here, a 0.06 m increase in the seaward tidal elevation boundary condition leads to a 9% decrease in peak orbital velocity during the summer. In systems with significant intertidal area and tidal marsh, sea-level rise will possibly increase the availability of sediment to landward portions of these habitats. However, if supply is limited, the marsh surface will not accrete fast enough to keep up with the rise.

In these simulations, the net increase in deposition in the shallowest areas (0-2 m) was 0.026 m, while relative water depth increased by 0.034 m. The increase in deposition at these depths was less in the decreased watershed sediment supply scenario (0.018 m), and relative water depth increased by 0.042 m, suggesting that the shallowest areas cannot keep up with sea-level rise, under present or future sediment supply conditions. It is necessary, however, to investigate intertidal sediment transport with more robust wetting/drying and wave propagation schemes, to estimate the change in mudflat profile or marsh accretion. Wave-breaking on mudflats and marsh trapping of sediment are

major processes that are not considered here, and may change sediment transport on the estuary fringe.

9.4.3 Effect of warming: scenario DS vs. scenario WDS

Though the climatic effect on snowpack is relatively minor over the next two decades, I have represented the changes in the hydrograph. Indeed, the effect on geomorphic change is minor: a net decrease in deposition of 0.001 m is simulated. It is important to note that this result is concurrent with sea-level rise and decreased sediment loads. Spatially, the greatest difference is observed in the landward sections of Grizzly Bay. These extremely minor changes are attributed to the change in water levels throughout Grizzly Bay, which are affected by the change in hydrographs between the two scenarios. The relative changes in water levels, combined with depth-dependent wave-induced resuspension, combine to create these anomalies. Under the more extreme snowpack changes by the end of this century (Knowles and Cayan, 2002), it is possible that the phasing between water level and wind-wave resuspension will be less important than the overall shifting of sediment loads to earlier in the water year, and relatively little sediment load in the late spring. With a stable wind signal, the relative timing of sediment loads and the wind-wave season may be more important than minor changes in water level.

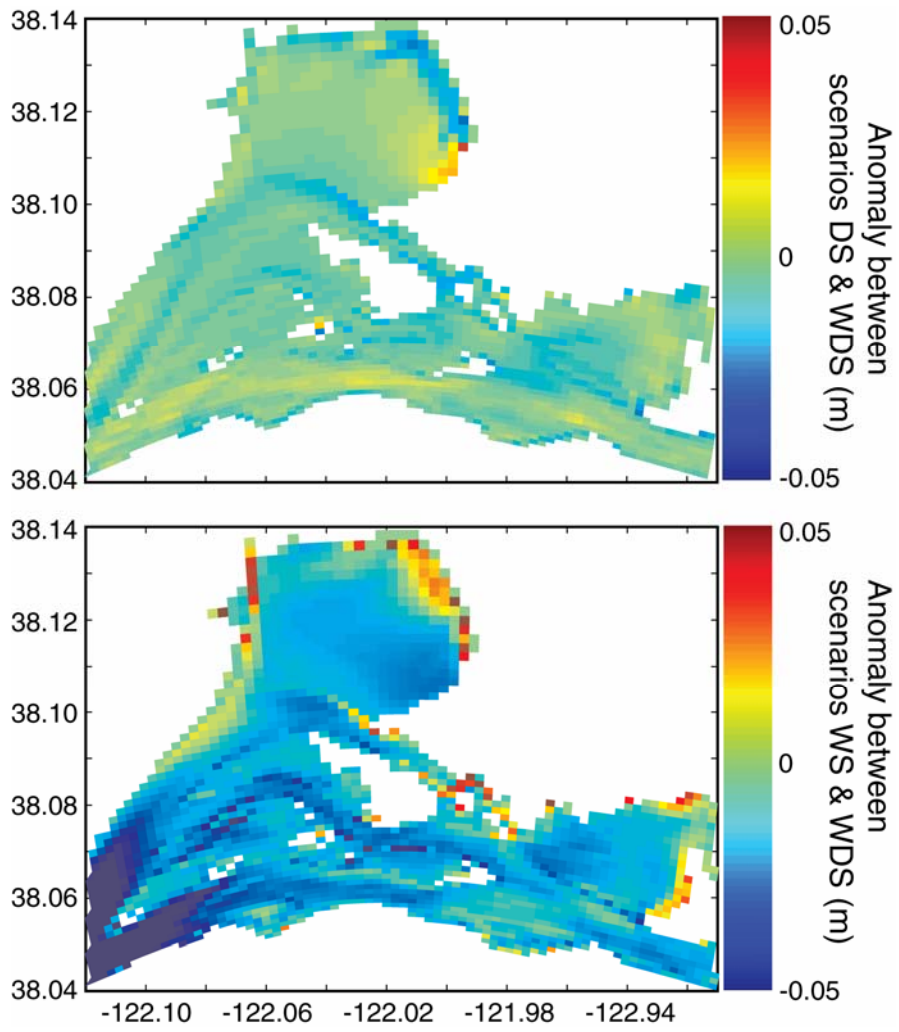

Figure 9.6 Anomaly between scenarios DS and WDS (showing the effect of warming and altered hydrograph) and anomaly between scenarios WS and WDS (showing the effect of decreased watershed sediment supply). Negative values indicate decreased sediment mass on the bed for the WDS scenario relative to the DS and WS scenarios, respectively.

9.4.4 Effect of decreased sediment loads: scenario WS vs. scenario WDS

With other forcings constant, reduced sediment supply from any boundary will result in a net decrease in deposition within an estuary. Depending on the magnitude of the reduction and the distance between the boundary and the estuary, the reduction may be linear or weakly non-linear. For example, the reduction in deposition for MH 2, under the decreased sediment supply scenario, was only 4%, but 24% for MH 3. The greater

freshwater flow in MH 3 allowed watershed-derived sediment to reach and bypass Suisun Bay, whereas the low freshwater flow of MH 2 did not supply much sediment to Suisun Bay no matter what the load. Because MH3 provided a substantial amount of sediment to Suisun Bay, under present conditions, the decreased sediment supply under 2030 conditions is more evident in the bathymetric changes of Suisun Bay.

The combined anomaly (Fig. 9.6) is dominated by the signal from MH 3, which had the largest reduction in deposition. Most areas of Suisun Bay became less depositional, though isolated portions of Grizzly and Honker Bay were more depositional. Phasing between sediment supply, deposition, and wind-wave resuspension are responsible for these variations: with a reduction in sediment supply, landward areas of Grizzly Bay are relatively deeper at the end of the freshwater flow period (before the wind-wave period). This relative increase in depth leads to a lesser influence of wave orbital velocities on the bed, leading to less erosion during the summer. This echoes the idea from above: the timing of sediment delivery relative to the summer wind-wave period may be important in decadal-timescale geomorphic change.

9.4.5 Changes in optical depth

Changes in bathymetry, water level, and suspended-sediment concentrations may indirectly alter ecological function, due to changes in optical depth. Optical depth (*OD*), which is inversely proportional to mean light irradiance, is defined as

$$OD = Dk_t \tag{9.1}$$

where

$$k_t = k_{ssc} + k_p \tag{9.2}$$

and D is total water depth (m), k_t is the light attenuation coefficient (m^{-1}), and k_{ssc} and k_p are the light attenuation contributions of suspended sediment and phytoplankton, respectively (Cloern 2007). Furthermore,

$$k_{ssc} = a_{ssc}SSC \tag{9.3}$$

where a_{ssc} normally falls in the range of 0.05 and 0.06 (J. Cloern, writ. comm.). Optical depth indicates the ecological function of a given habitat, between autotrophic (primary production, OD<10) and heterotrophic (secondary production, OD>20) (Cloern, 2007). In a purely autotrophic system, organisms convert light and other inorganic compounds into energy; in a heterotrophic system organisms depend on other organic sources (e.g. other organisms) for energy. Changes in optical depth due to future scenarios can be estimated by simulating tidal-timescale turbidity, with current and future bathymetry. Because of the overall deeper conditions (favoring increased optical depth) and decreases in sediment supply (favoring decreased optical depth) in scenario WDS, increases in optical depth indicate that deepening outweighs decreases in turbidity; conversely a decrease in optical depth suggests that despite deeper conditions, reductions in turbidity dominate.

Two cases are simulated here, using MH 3: 1) base; the current hydrograph, sea-level rise, and sediment load conditions for one year, with the 1990 bathymetry; and 2) future; the 2030 hydrograph, sea-level rise, and sediment load conditions with the final, evolved bathymetry from scenario WDS. In these simulations, morphological acceleration is switched off, in order to represent realistic tidal-timescale turbidities. Mean optical depths over the entire water year are calculated assuming $k_p = 0$ and $a_{ssc} = 0.05$. As an indicator of overall system function, I compare the total areas of regions with OD<10 and OD>20. In the base simulation (Table 9.5), 48% of Suisun Bay and the western Delta area characterized by a mean *OD*<10, while 37% have *OD*>20. In contrast, the future simulation yields 50% of the area with *OD*<10, and 36% with *OD*>20. The overall effect is a 2% increase in autotrophic habitat and a 1% decrease in heterotrophic habitat, under the prescribed scenario. The increase in low-*OD* area is attributed to the overall decline in suspended-sediment concentrations (due to decreased watershed sediment supply), especially in the shallower areas of Suisun Bay (where wave-energy is reduced due to increased sea-level). Sea-level rise acts to increase *OD*, while decreased sediment supply (and therefore decreased SSC) acts to decrease *OD*; therefore these two forces counteract each other to yield relatively small changes in *OD*.

Table 9.5 Percent area of Suisun Bay and western Delta characterized by optical depth ranges.

OD range	% area base scenario	% area future scenario
<10	48%	50%
10-20	15%	14%
>20	37%	36%

9.5 Conclusion

After calibrating and applying the ROMS model to tidal, annual, and decadal-timescale processes, it is suitable for use in evaluating future geomorphic evolution. Future scenarios of global warming, sea-level rise, and decreased watershed sediment supply may combine to modulate geomorphic evolution in Suisun Bay, thereby altering habitat distribution and turbidity. I have applied the model to four scenarios: 1) base-case, 2) warming and sea-level rise, 3) decreased watershed sediment supply and sea-level rise, and 4) warming, sea-level rise, and decreased watershed sediment supply. Sea-level rise resulted in a reduction in wave orbital velocity, reducing sediment redistribution and promoting overall sediment deposition in the shallowest 2 m of Suisun Bay, while decreased watershed sediment supply decreased deposition through most of Suisun Bay. The moderate warming signal of 2030, reflected in altered streamflow timing and magnitude, had the most minor effect on overall geomorphic change. However, changes by the end of the 21st century may be sufficient to alter the sediment transport patterns within Suisun Bay. In all cases, the observed deposition was not sufficient to counteract the increase in sea level, which has major ramifications for intertidal and marsh areas of Suisun Bay. In all scenarios with sea-level rise, relative water depth increased throughout the estuary.

While this study does not consider climatic changes such as extended drought, the relative effect of drier years as opposed to wetter years is quantified. Drier years allow more landward sediment transport from San Pablo Bay, which currently has a stable supply of sediment. Under present-day watershed sediment yield conditions, San Pablo

Bay is an important source of sediment to Suisun Bay. If future climatic changes favor drought as opposed to wet or normal conditions, the seaward end of Suisun Bay may become relatively more depositional, while the landward end becomes relatively more erosional. This may dictate whether Suisun Bay imports sufficient sediment to maintain intertidal and marsh habitat, and also suggests the composition of deposited sediment will reflect a more seaward source.

The ultimate product of this effort is a tool for estimating ecological changes due to estuarine geomorphic change. The model is used to estimate a future scenario of changes in optical depth (*OD*), a critical variable for characterizing estuarine productivity. Despite increases in water level (which favor increases in *OD*), a reduction in suspended-sediment concentration leads to a 2% increase in low-*OD* area (*OD*<10), suggesting clearer waters with greater phytoplankton biomass. From an ecological point-of-view, this indicates that the changes in sediment supply are more relevant than sea-level rise, at least at present rates of change. However, it should be noted that future increases in sea-level will inundate more intertidal and marsh areas; if current declines in sediment supply continue, those areas may not accrete enough to maintain elevation. This is another effect that estuarine geomorphic change will on the ecosystem. The modeling results here show that accretion cannot keep pace with sea-level rise, though the complex sediment transport between the estuary and intertidal/marsh areas is not directly simulated.

There are inherent limitations to scenario modeling of this type, beyond uncertainty in modeling parameters. These simulations assume static conditions in terms of wind

regime, bed properties, shoreline configuration, and seaward boundary conditions over a 20 y period. A change in any these properties may invalidate the qualitative and quantitative results of this study. Changes between scenarios may also change due to non-stationary processes.

10 Conclusions

10.1 Satisfaction of research objectives

The research objectives specified in Chapter 1 are reiterated here, followed by the final outcome of those efforts.

10.1.1 Objective A: Development of a reliable modeling approach

My first objective was to develop a reliable modeling approach that provides the greatest confidence in model output. I achieved this objective by first addressing the relationship between models and the theories they are based on, and the relationship between models and the world they aim to represent. Proper verification, calibration, and validation establish the veracity of those relationships, while model-building techniques provide confidence in the modeling approach. My multiple-timescale calibration approach ensures that errors on the tidal-timescale will not accumulate to confound annual-timescale modeling, and that errors on the annual-timescale will not accumulate to confound decadal-timescale modeling.

10.1.2 Objective B: Calibration and application to tidal-timescale processes

The second objective was to modify, apply, and calibrate the model to tidal processes in Suisun Bay. This objective was successfully achieved by calibrating the model to tidal stage, validating to salinity dynamics, and accurately modeling the lateral movement of the estuarine turbidity maximum. Best agreement was obtained by modifying the bottom roughness in the logarithmic drag formulation. This step indicated the ability of the model to represent tidal-timescale dynamics, which can accumulate to alter annual-

timescale phenomena in estuaries: mainly the representation of gravitational circulation and near-bed landward sediment transport. The importance of tidal-timescale gravitational circulation, for example, can be seen in the annual-timescale sediment transport to Suisun Bay: during the low-flow period, landward transport accounts for the majority of sediment flux.

10.1.3 Objective C: Calibration and application to annual-timescale processes

Objective C involved modifying, applying, and calibrating the model to annual processes in Suisun Bay: suspended-sediment fluxes at two cross-sections (landward and seaward boundaries), and ultimately the net sediment budget of Suisun Bay on the annual timescale during 1997-1998, and 2002-2004. I calibrated the model by altering sediment bed characteristics, sediment distribution, and wave energy. Calibration was performed with two years of data, with the remaining three years used for validation. The model successfully simulated the net sediment budget to and from Suisun Bay for three of five years, and captured seasonal and episodic patterns reasonably. These simulations established a baseline set of parameters for geomorphic modeling, and the suitability of the model: simulating net bed change over one year first requires accurate simulation of net fluxes over one year. This step also validated my use of idealized functions for salinity, SSC, and wave energy.

10.1.4 Objective D: Calibration and application to decadal-timescale processes

Hindcasting known historical bathymetric change was the objective for the final calibration step. A major improvement from the annual-timescale simulations is the

inclusion of varying bathymetry in the wind-wave solution, due to changes in bathymetry. Here I established the validity of two major simplifications: use of a morphological acceleration factor, and use of a limited set of morphological hydrographs. These two simplifications, when implemented into the model, reduced computational expense and input needs while still accurately modeling changes in depth for the 1867-1887 period. The most critical finding during this step was the importance of total sediment load and wave parameterization: redistribution of delivered sediment from wind-waves is largely responsible for the final geomorphic outcome, while timing and total magnitude of freshwater flows are relatively minor. Peak freshwater flows, however, are capable of affecting redistribution significantly. Error is quantified using a metric that accounts for the error relative to total depth, along with a skill score that was recently proposed for use in geomorphic modeling. The combination of these metrics gives a robust evaluator of performance for use in any model of spatial processes.

10.1.5 Objective E: Application of calibrated model to future scenarios

The final objective is to apply the calibrated model and approach to a 20 y climate change scenario. Here I simulated four scenarios: base-case, moderate warming with sea-level rise, sediment supply decrease with sea-level rise, and combined warming, sediment supply decrease, and sea-level rise. Using the concept of the morphological hydrograph, I selected three hydrographs representing wet, moderate, and dry years, and modulated them for each scenario. This step showed the importance of net sediment supply and sea-level rise over minor changes in timing and magnitude of freshwater flow. Sea-level rise encouraged 0.01 m more of sediment deposition due to the reduced effect of wave orbital

velocities on the bed in deeper water, though relative water depth increased by 0.05 m; decreased sediment supply reduced deposition more in wet years (24 % reduction) than dry years (4% reduction). Streamflow timing and magnitude led to relatively minor changes in geomorphic change (0.001 m), due to slight changes in water depth induced by freshwater flow pulses. Under the worst-case (and most likely) scenario of warming, decreased sediment supply, and sea-level rise, an overall deepening of 0.065 m was modeled. Scenarios modeling, when evaluating differences, is shown to be relatively insensitive to parameter uncertainty.

10.2 Summary

Prior efforts in estuarine geomorphic modeling have laid substantial groundwork for robust modeling, but observational data at the decadal-timescale is usually lacking. The concept of the morphological tide and morphological acceleration factor reduce input needs and computational expense, which enable decadal-timescale modeling simulations. The wealth of tidal, annual, and decadal-timescale data for Suisun Bay, California, makes it a prime candidate for developing a robust calibration and application procedure for simulating estuarine geomorphic change. I have used concepts from prior efforts and observational data in Suisun Bay to calibrate and apply the Regional Ocean Modeling System to tidal, annual, and decadal-timescale data. A major contribution of this work is the concept of the morphological hydrograph, whereby a limited set of hydrographs can provide the same geomorphic change result as the real set of hydrographs, limiting input needs. I have also performed a decadal-timescale calibration of a tidal-timescale model, using measured bathymetric change data. I have established a method of assessing

performance: accurate representation of area-weighted bathymetric change in depth intervals, and minimizing the ratio of error to total depth. In this study, I achieved a ratio of 5%: for example, an error of 0.05 m in 1 m of water. Based on the importance of specific depth ranges in an ecological sense, one can minimize error in those regions using these metrics. Performance can also be evaluated with a decomposed Brier Skill Score, which indicates if phase, amplitude, or net bed change is responsible for poor agreement, though the score does not account for error relative to total water depth.

The model successfully captured processes at all timescales, and was then applied to three scenarios of future change: warming and sea-level rise; decreasing sediment supply and sea-level rise; and warming, decreasing sediment supply, and sea-level rise. The relative effects of each process were evaluated, with sea-level rise inducing greater landward transport and deposition, while decreased sediment supply reduced deposition, especially in years with larger sediment supply. Freshwater flow timing and magnitude, at least under mild warming conditions, were secondary forcings on estuarine geomorphology.

10.3 Recommendations for future work

10.3.1 Study-specific recommendations

Proper representation of modern Delta, seaward embayments, and sediment transport

Computing limitations have led to many idealizations in this study, including idealization of the geometry of the Sacramento/San Joaquin Delta, and idealization of seaward boundary conditions. Inclusion of the actual Delta in this study may have increased the

domain by 200%, and required more tuning of in-Delta parameters to attain proper hydrodynamics and sediment transport. Including the entire domain of San Francisco Bay would also increase computational expense and require proper representation of wind-waves and sediment parameters. Ideally, the entire model domain would stretch from the tidal limit of the Delta to the ocean boundary. Of course this would then require more calibration data and more uncertainty, but sediment transport within and between the Delta and ocean must be represented.

Sources of particles

The calibrated model may be a helpful tool for evaluating sources of particles to the ecologically important areas of Suisun Bay. Sources of contaminants, which adhere to sediment particles, may be the watershed or seaward embayments. Differentiating seaward and landward sediment classes, while keeping particle characteristics the same, can trace the composition of the bed sediments during the simulation. Under different scenarios, such as sea-level rise, the fraction of seaward sediments may increase within Suisun Bay. This would suggest that the composition of bed sediments would reflect a seaward source. It is known that certain contaminants are found in higher concentrations in San Pablo Bay, this tool could evaluate a possible increase in those constituents within Suisun Bay.

Simulation of wave propagation with SWAN

This study has demonstrated that wave energy is the most sensitive parameter for geomorphic simulations in Suisun Bay. Due to the significant areas of shoals and regular

wind patterns, resuspension over Grizzly and Honker Bays are major mechanisms for transport and subsequent deposition patterns. The simplified wave field used here is able to reproduce net bed changes, but precise patterns are not well-reproduced. This may be alleviated by use of a modern wind-wave model, such as SWAN, which simulates the propagation of waves over bathymetry (which the present configuration does not). Wave propagation in Suisun Bay is more complex than what is specified in this study, and SWAN may better model the resuspension of bed sediment over the shoals.

10.3.2 General recommendations

Comparison of continuous 20 year simulation with morphologically accelerated version

Limitations in computational power have required the use of a morphological acceleration factor and the morphological hydrograph for this study. Though the time required for a continuous 20 y simulation is prohibitive for this model configuration, it would be worthwhile to compare this result to the morphologically accelerated version in a simpler case. This would further validate the use of the morphological acceleration factor, and the morphological hydrograph. Both idealized and actual test cases could be tested in this way. Model sensitivity to acceleration factor and number of morphological hydrographs should also be tested.

Use of morphological acceleration factor in episodic systems

The use of a morphological acceleration factor in tidal systems has been relatively well-explored, but in systems with episodic sediment delivery, research is quite limited. In conjunction with the above task, it would be possible to conduct several runs, with

morphological acceleration, that give varying weight to the episodic signal. The morphological acceleration factor could be held constant during the tidally dominated periods, but scaled up or down during high freshwater flows or the wind-wave period. This would be a more robust sensitivity analysis, that would also give insight to the behavior of morphological acceleration in episodic systems.

General requirements for developing estuarine geomorphic models

Before attempting to develop an estuarine geomorphic model, data at multiple timescales must be available. Tidal-timescale data, such as stage, velocity, and SSC, must be collected over at least an annual period at multiple locations, in order to capture inter-annual processes (such as episodic freshwater flows, wind-waves, and stratification). These data can be used to calibrate and validate the model at the tidal-timescale. Additionally, these data can be used as surrogates to estimate cross-sectional sediment fluxes (e.g. Ganju and Schoellhamer, 2006).

Cross-sectional sediment fluxes, over the annual-timescale, provide insight into the processes that govern net sediment budgets within an estuary. Persistent landward or seaward residual fluxes, due to inter-annual forcing, must be modeled adequately to provide the correct mass of sediment to the estuary. Model calibration and validation to these data is an intermediate step towards simulating decadal-timescale geomorphic change.

The most critical data source for decadal-timescale simulations is measured bathymetric change. Hindcasting of measured data builds confidence in the model development and application, and assists in testing sensitivity to boundary conditions, forcings, and time-stepping approaches. While these data are expensive and difficult to obtain, they are necessary for model testing. Though the interval between surveys depends on the magnitude of erosion and deposition within the estuary, data collected at decadal intervals seems to be adequate for model development.

References

Aguado, E., Cayan, D., Riddle, L., and Roos, M., 1992. Climatic fluctuations and the timing of West Coast streamflow. Journal of Climate, 5, 1468–1483.

Aller, J.Y., and Stupakoff, I., 1996. The distribution and seasonal characteristics of benthic communities on the Amazon shelf as indicators of physical processes. Continental Shelf Research 16, 717–751.

Ariathurai, R., and Arulanandan, K., 1978. Erosion rates of cohesive soils. Proceedings of the American Society of Civil Engineering, Journal of the Hydraulics Division, 104, 279–283.

Arzayus, K.M., Dickhut, R.M., and Canuel, E.A., 2002. Effects of physical mixing on the attenuation of polycyclic aromatic hydrocarbons in estuarine sediments. Organic Geochemistry 33, 1759–1769.

Barnola, J.M, Raynaud, D., Korotkevich, Y.S., and Lorius, C., 1987. Vostok ice core provides 160,000-year record of atmospheric CO_2. Nature, 329, 408–414.

Bartholdy, J., Christiansen, C., and Kunzendorf, H., 2004. Long term variations in backbarrier salt marsh deposition on the Skallingen peninsula – the Danish Wadden Sea. Marine Geology, 203, 1-21.

Bergamaschi, B.A., Kuivila, K.M., and Fram, M.S., 2001. Pesticides associated with suspended sediments entering San Francisco Bay following the first major storm of water year 1996. Estuaries, 24, 368–380.

Blaber, S.J.M., and Blaber, T.G., 1980. Factors affecting the distribution of juvenile estuarine and inshore fish. Journal of Fish Biology, 17, 143–162.

Blanton, J.O., Seim, H., Alexander, C., Amft, J., and Kineke, G., 2003. Transport of salt and suspended sediments in a curving channel of a coastal plain estuary: Satilla River, GA. Estuarine, Coastal and Shelf Science 57, 993–1006.

Booij, N., Ris, R.C., and Holthuijsen, L.H., 1999. A third-generation wave model for coastal regions, Part I, Model description and validation. Journal of Geophysical Research, 104, 7649–7666.

Buchanan, P.A., and Ganju, N.K., 2005. Summary of suspended-sediment concentration data in San Francisco Bay, California, water year 2003: U.S. Geological Survey Data Series 113.

Burau, J.R., Simpson, M.R., and Cheng, R.T., 1993. Tidal and residual currents measured by an acoustic Doppler current profiler at the west end of Carquinez Strait, San Francisco

Bay, California, March to November 1988. U.S. Geological Survey Water-Resources Investigations Report 92-4064, 79 p.

Burningham, H., and French, J., 2006. Morphodynamic behaviour of a mixed san-gravel ebb-tidal delta: Deben estuary, Suffolk, UK. Marine Geology, 225, 23–44.

Cahoon, D.R., Lynch, J.C., and Powell, A.N., 1996. Marsh vertical accretion in a southern California estuary, U.S.A. Estuarine, Coastal and Shelf Science, 43, 19–32.

California Department of Water Resources, DAYFLOW program, http://iep.water.ca.gov/dayflow. Accessed at various times.

Cappiella, K., Malzone, C., Smith, R., and Jaffe, B., 1999. Sedimentation and bathymetry changes in Suisun Bay, 1867-1990. U.S. Geological Survey Open-File Report 99-563.

Carlton, J.T., Thompson, J.K., Schemel, L.E., and Nichols, F.H., 1990. The remarkable invasion of San Francisco Bay (California, USA) by the Asian clam *Potamocorbula amurensis*, I, Introduction and dispersal. Marine Ecology Progress Series, 66, 81-94.

Cayan, D.R., Bromirski, P.D., Hayhoe, K., Tyree, M., Dettinger, M.D., and Flick, R.E., in press. Climate change projections of sea level extremes along the California coast. Climatic Change.

Cloern, J.E., 2007. Habitat connectivity and ecosystem productivity: implications from a simple model. The American Naturalist, 169, E21-E33.

Coastal Engineering Research Center, 1984. Shore Protection Manual. U.S. Army Corps of Engineers, Waterways Experiment Station, Vicksburg, Mississippi.

Dame, R., Alber, M., Allen, D., Mallin, M., Montague, C., Lewitus, A., Chalmers, A., Gardner, R., Gilman, C., Kjerfve, B., Pinckney, J., and Smith, N., 2000. Estuaries of the south Atlantic coast of North America: their geographical signatures. Estuaries, 23, 793-819.

Darrigol, O., 2005. Worlds of flow: A history of hydrodynamics from the Bernoullis to Prandtl. Oxford University Press, New York, 356 pp.

Day, J.W., Rybczyk, J., Scarton, F., Rismondo, A.. Are, D., and Cecconi, G., 1999. Soil accretionary dynamics, sea-level rise and the survival of wetlands in Venice Lagoon: a field and modelling approach. Estuarine, Coastal and Shelf Science, 49, 607–628.

Dean, R.G., and Dalyrymple, R.A., 1991. Water wave mechanics for scientists and engineers. World Scientific Publishing, Singapore, 353 pp.

De Vriend, H.J., Capobianco, M., Chesher, T., De Swart, H.E., Latteux, B., and Stive, M.J.F., 1993. Approaches to long-term modelling of coastal morphology: a review. Coastal Engineering, 21, 225–269.

Douillet, P., Ouillon, S., and Cordier, E., 2001. A numerical model for fine suspended sediment transport in the southwest lagoon of New Caledonia. Coral Reefs, 20, 361–372.

Dyer, K.R., 1974. The salt balance in stratified estuaries. Estuarine and Coastal Marine Science, 2, 273–281.

Federal Aviation Administration, 2003. Proposed SFO runway reconfiguration project, Predicted changes in hydrodynamics, sediment transport, water quality, and aquatic biotic communities associated with SFO runway reconfiguration alternatives BX-6, A3, and BX-R. Final Technical Report.

Fenster, M.S., and Fitzgerald, D.M., 1996. Morphodynamics, stratigraphy, and sediment transport patterns of the Kennebec River estuary, Maine, USA. Sedimentary Geology, 107, 99-120.

Flick, R.E., Murray, J.F., and Ewing, L.C., 2003. Trends in the United States tidal datum statistics and tide range. Journal of Waterway, Port, Coastal, and Ocean Engineering, 129, 155-164.

Ganju, N.K, Knowles, N., and Schoellhamer, D.H., in review. Temporal downscaling of decadal sediment load estimates to a daily interval for use in hindcast simulations. Journal of Hydrology.

Ganju, N.K., and Schoellhamer, D.H., 2006. Annual sediment flux estimates in a tidal strait using surrogate measurements. Estuarine, Coastal and Shelf Science, 69, 165–178.

Ganju, N.K. and Schoellhamer, D.H., in press(a). Lateral variability of the estuarine turbidity maximum in a tidal strait. In: Kusuda, T., Yamanishi, H., Spearman, J., and Gailani, J.Z. (eds.), Sediment and Ecohydraulics: INTERCOH 2005, Elsevier, Amsterdam, Netherlands.

Ganju, N.K., and Schoellhamer, D.H., in press(b). Calibration of an estuarine sediment transport model to sediment fluxes for robust simulation of geomorphic evolution. Continental Shelf Research.

Ganju, N.K., Schoellhamer, D.H., Warner, J.C., Barad, M.F., and Schladow, S.G., 2004. Tidal oscillation of sediment between a river and a bay: a conceptual model. Estuarine, Coastal and Shelf Science, 60, 81–90.

Gartner, J.W., and Cheng, R.T., 1982. Observations from moored current meters in San Francisco Bay. US Geological Survey Open-File Report 82-153, 91 p.

Geyer, W.R., Signell, R.P., and Kineke, G.C., 1998. Lateral trapping of sediment in a partially mixed estuary. In: Eighth Biennial Conference on Physics of Estuaries and Coastal Seas, 1996. A. A. Balkema, Rotterdam, The Netherlands, pp. 115–126.

Geyer, W.R., Woodruff, J.D., and Traykovski, P., 2001. Sediment transport and trapping in the Hudson River Estuary. Estuaries, 24, 670–679.

Gilbert, G.K., 1917. Hydraulic mining debris in the Sierra Nevada. U.S. Geological Survey Professional Paper 105, 148 pp.

Grabemann, I., Uncles, R.J., Krause, G., and Stephens, J.A., 1997. Behaviour of turbidity maxima in the Tamar (U.K.) and Weser (F.R.G.) Estuaries. Estuarine, Coastal and Shelf Science, 45, 235–246.

Haberle, S.G., and Maslin, M.A., 1999. Late quaternary vegetation and climate change in the Amazon Basin based on a 50,000 year pollen record from the Amazon Fan, ODP Site 932. Quaternary Research, 51, 27–38.

Haff, P.K., 1996. Limitations on predictive modeling in geomorphology. In: Rhoads B.L., and Thorn, C.E. (eds.), The scientific nature of geomorphology, John Wiley & Sons Ltd, pp. 337–358.

Hibma, A., de Vriend, H.J., and Stive, M.J.F, 2003. Numerical modeling of shoal pattern formation in well-mixed elongated estuaries. Estuarine, Coastal and Shelf Science, 57, 981–991.

Hornberger, M.I., Luoma, S.N., van Geen, A., Fuller, C., and Anima, R., 1999. Historical trends of metals in the sediments of San Francisco Bay, California. Marine Chemistry, 64, 39–55.

Hulme, M., Mitchell, J., Ingram, W., Lowe, J., Johns, T., New, M., and Viner, D., 1999. Climate change scenarios for global impacts studies. Global Environmental Change, 9, S3–S19.

Islam, M.S., Ueda, H., and Tanaka, M., 2005. Spatial distribution and trophic ecology of dominant copepods associated with turbidity maximum along the salinity gradient in a highly embayed estuarine system in Ariake Sea, Japan. Journal of Experimental Marine Biology and Ecology, 316, 101–115.

Jaffe, B.E., Smith, R.E., and Foxgrover, A.C., 2007. Anthropogenic influence on sedimentation and intertidal mudflat change in San Pablo Bay, California: 1856-1983. Estuarine, Coastal and Shelf Science, 73, 175-187.

Jaffe, B. E., Smith, R. E., and Torresan, L. Z., 1998. Sedimentation and bathymetric change in San Pablo Bay: 1856 to 1983. U.S. Geological Survey Open-File Report 98-759.

Jassby, A.D., and Powell, T.M., 1994. Hydrodynamic influences on interannual chlorophyll variability in an estuary: Upper San Francisco Bay-Delta (California, U.S.A.). Estuarine, Coastal and Shelf Science, 39, 595–618.

Jay, D. A., and Musiak, J.D., 1994. Particle trapping in estuarine turbidity maxima. Journal of Geophysical Research, 99, 446–461.

Kimmerer, W.J., Burau, J.R., and Bennett, W.A., 1998. Tidally oriented vertical migration and position maintenance of zooplankton in a temperate estuary. Limnology and Oceanography, 43, 1697–1709.

Knowles, N. and Cayan, D., 2002. Potential effects of global warming on the Sacramento/San Joaquin watershed and the San Francisco estuary. Geophysical Research Letters, 29, 38–1.

Krone, R.B. 1979. Sedimentation in the San Francisco Bay system. In: Conomos, T.J. (ed.), San Francisco Bay: The Urbanized Estuary, Pacific Division of the American Association for the Advancement of Science, San Francisco, California, pp. 85-96.

Latteux, B., 1995. Techniques for long-term morphological simulation under tidal action. Marine Geology, 126, 129-141.

Leonard, L.A., 1997. Controls of sediment transport and deposition in an incised mainland marsh basin, southeastern North Carolina. Wetlands, 17, 263–274.

Lesser, G.R., Roelvink, J.A., van Kester, J.A.T.M, and Stelling, G.S., 2004. Development and validation of a three-dimensional morphological model. Coastal Engineering, 51, 883–915.

Linville, R.G., Luoma, S.N., Cutter, L., and Cutter, G.A., 2002. Increased selenium threat as a result of invasion of the exotic bivalve *Potamacorbula amurensis* into the San Francisco Bay-Delta. Aquatic Toxicology, 57, 51–64.

Longino, H.E., 2002. The fate of knowledge. Princeton University Press, New Jersey, 233 pp.

Lopez, C. B., Cloern, J.E., Schraga, T.S., Little, A.J., Lucas, L.V., Thompson, J.K., and Burau, J.R., 2006. Ecological values of shallow-water habitats: implications for restoration of disturbed ecosystems. Ecosystems, 9, 422–440.

Lugo, A.E., and Snedaker, S.C., 1974. The ecology of mangroves. Annual Review of Ecology and Systematics, 5, 39–64.

Lumborg, U., and Pejrup, M., 2005. Modelling of cohesive sediment transport in a tidal lagoon – an annual budget. Marine Geology, 218, 1–16.

Lynch, P., 2006. The emergence of numerical weather prediction: Richardson's dream. Cambridge University Press, New York, 279 pp.

Madsen, O. S., 1994. Spectral wave-current bottom boundary layer flows. Proceedings, 24th International Conference Coastal Engineering Research Council, 384–398.

McDonald, E.T. and Cheng, R.T., 1997. A numerical model of sediment transport applied to San Francisco Bay, California. Journal of Marine Environmental Engineering, 4, 1–41.

McKee, L.J., Ganju, N.K., and Schoellhamer, D.H., 2006. Estimates of suspended sediment entering San Francisco Bay from the Sacramento and San Joaquin Delta, San Francisco Bay, California. Journal of Hydrology, 323, 335–352.

Means, T.H., 1928. Saltwater problem: San Francisco Bay and Delta of Sacramento and San Joaquin Rivers. Report prepared for the Association of Industrial Water Users of Contra Costa and Solano Counties.

Meehl, G.A., Stocker, T.F., Collins, W.D., Friedlingstein, P., Gaye, A.T., Gregory, J.M., Kitoh, A., Knutti, R., Murphy, J.M., Noda, A., Raper, S.C.B., Watterson, I.G., Weaver, A.J., and Zhao, Z.C., 2007. Global Climate Projections. In: Solomon, S., Qin, D., Manning, M., Chen, Z., Marquis, M., Averyt, K.B., Tignor, M., and Miller, H.L., (eds.), Climate Change 2007: The Physical Science Basis. Contribution of Working Group I to the Fourth Assessment Report of the Intergovernmental Panel on Climate Change Cambridge University Press, Cambridge, United Kingdom and New York, NY, USA.

Meko, D.M., Therrell, M.D., Baisan, C.H., and Hughes, M.K., 2001. Sacramento River flow reconstructed to A.D. 869 from tree rings. Journal of the American Water Resources Association, 37, 1029–1039.

Meko, D.M., Touchan, R., Hughes, M., and Caprio, A.C., 2002. San Joaquin River flow reconstructed from tree rings: In West, G.J., Blomquist, N.L. (eds.), Proceedings of the 19th Annual Pacific Climate Workshop: Interagency Ecological Program for San Francisco Estuary Technical Report 71, p. 186.

Meyer-Peter, E., and Mueller, R., 1948. Formulas for bed-load transport. In: Report on the 2nd Meeting International Association Hydraulic Structure Research. Stockholm, Sweden, pp. 39–64.

Monismith, S., Burau, J.R., and Stacey, M., 1996. Stratification dynamics and gravitational circulation in northern San Francisco Bay. In: Hollibaugh, J.T. (ed.), San Francisco Bay: The Ecosystem. Pacific Division of the American Association for the Advancement of Science, San Francisco, pp. 123–153.

Morrison, M., and Morgan, M.S., 1999. Models as mediating agents. In: Morgan, M.S. and Morrison, M. (eds.), Models as mediators (Cambridge University Press, Cambridge, U.K., 401 pp.

Murphy, A.H., and Epstein, E.S., 1989. Skill scores and correlation coefficients in model verification. Monthly Weather Review, 117, 572–581.

Murray, A.B., 2003. Contrasting the goals, strategies, and predictions associated with simplified numerical models and detailed simulations. Prediction in geomorphology, Geophysical Monograph 135, American Geophysical Union, 15 pp.

Oltmann, R.N., 1998. Indirect measurement of Delta outflow using ultrasonic velocity meters and comparison to mass-balance calculated outflow. Interagency Ecological Program Newsletter 11, 5–8.

Oreskes, N., Shrader-Frechette, K., and Belitz, K., 1994. Verification, validation, and confirmation of numerical models in the earth sciences. Science, 263, 641-646.

Orth, R.J., Heck, Jr., K.L, and van Montfrans, J., 1984. Faunal communities in seagrass beds: a review of the influence of plant structure and prey characteristics on predator: prey relationships. Estuaries, 7, 339–350.

Ouillon, S., Douillet, P., and Andréfouët, S., 2004. Coupling satellite data with in situ measurements and numerical modeling to study fine suspended-sediment transport: a study for the lagoon of New Caledonia. Coral Reefs, 23, 109–122.

Peterson, D.H., Conomos, T.J., Broenkow, W.W., and Doherty, P.C., 1975. Location of the non-tidal current null zone in northern San Francisco Bay. Estuarine and Coastal Marine Science, 3, 1–11.

Pethick, J., 1993. Shoreline adjustments and coastal management: physical and biological processes under accelerated sea-level rise. The Geographical Journal, 159, 162–168.

Pilkey, O.H., and Pilkey-Jarvis, L., 2007. Useless arithmetic: why environmental scientists can't predict the future. Columbia University Press, New York, 256 pp.

Pont, D., Day, J.W., Hensel, P., Franquet, E., Torre, F., Rioual, P., Ibanez, C., and Coulet, E., 2002. Response scenarios for the deltaic plain of the Rhone in the face of an acceleration in the rate of sea-level rise with special attention to *Salicornia*-type environments. Estuaries, 25, 337–358.

Porterfield, G., 1980. Sediment transport of streams tributary to San Francisco, San Pablo, and Suisun Bays, California, 1909-1966. U.S. Geological Survey Water Resources Investigations 80-64, 92 pp.

Preston-Thomas, H., 1990. The International Temperature Scale of 1990 (ITS-90). Metrologia, 27, 3-10.

Pritchard, D.W., 1967. What is an estuary: physical viewpoint. In: Estuaries (Lauff, G.H., ed.), American Association for the Advancement of Science, Publication 83, Washington D.C.

Reed, D.J., 2002. Understanding tidal marsh sedimentation in the Sacramento-San Joaquin Delta, California. Journal of Coastal Research, Special Issue 36, 605–611.

Regional Monitoring Program, 2006. Regional monitoring program data access website. http://sfei.org/rmp/rmp_data_access.html

Revelle, R.R., 1990. Sea level change. National Academy Press, Washington, D.C., 234 pp.

Ridd, P.V., Stieglitz, T., and Larcombe, P., 1998. Density-driven secondary circulation in a tropical mangrove estuary. Estuarine, Coastal and Shelf Science, 47, 621–632.

Roache, P.J., 1997. Quantification of uncertainty in computational fluid dynamics. Annual Review of Fluid Mechanics, 29, 123-160.

Roeckner, E., Bengtsson, L., Feichter, J., Lelieveld, J., and Rodhe, H., 1999. Transient climate change simulations with a coupled atmosphere-ocean GCM including the tropospheric sulfur cycle. Journal of Climate, 12, 3004–3032.

Roelvink, J.A., 2006. Coastal morphodynamic evolution techniques. Coastal Engineering, 53, 277–287.

Rouse, H., 1937. Modern conceptions of the mechanics of fluid turbulence. Transactions of the American Society of Civil Engineers, 102, 463–541.

Ruhl, C.A., and Schoellhamer, D.H., 2004. Spatial and temporal variability of suspended-sediment concentrations in a shallow estuarine environment. San Francisco Estuary and Watershed Science, 2(2), article 1.

Ryan, H.F., Gibbons, H., Hendley II, J.W., and Stauffer, P., 1999. El Niño sea-level rise wreaks havoc in California's San Francisco Bay region. U.S. Geological Survey Fact Sheet 175-99, 4 pp.

Sanford, L.P., Suttles, S.E., and Halka, J.P., 2001. Reconsidering the physics of the Chesapeake Bay estuarine turbidity maximum. Estuaries, 24, 655–669.

Schoellhamer, D.H., 2001. Influence of salinity, bottom topography, and tides on locations of estuarine turbidity maxima in northern San Francisco Bay. In: McAnally, W.H., and Mehta, A.J. (eds.), Coastal and Estuarine Fine Sediment Transport Processes, Elsevier Science B.V., Amsterdam, Netherlands, pp. 343–357.

Schoellhamer, D. H., Burau, J. R., 1998. Summary of findings about circulation and the estuarine turbidity maximum in Suisun Bay, California. U.S. Geological Survey Fact Sheet FS-047-98. 6 pp.

Schoellhamer, D.H., Ganju, N.K., Mineart, P.R., and Lionberger, M.A., in press. Sensitivity and spin up times of cohesive sediment transport models used to simulate bathymetric change. In: Kusuda, T., Yamanishi, H., Spearman, J., and Gailani, J.Z. (eds.), Sediment and Ecohydraulics: INTERCOH 2005, Elsevier, Amsterdam, Netherlands.

Shchepetkin, A.F. and McWilliams, J.C., 2005. The Regional Ocean Modeling System (ROMS): A split-explicit, free-surface, topography-following coordinates ocean model. Ocean Modelling, 9, 347–404.

Simas, T., Nunes, J.P., and Ferreira, J.G., 2001. Effects of global climate change on coastal salt marshes. Ecological Modelling, 139, 1–15.

Simpson, M. R., and Bland, R., 2000. Methods for accurate estimation of net discharge in a tidal channel. Institute of Electrical and Electronics Engineers Journal of Oceanic Engineering, 25, 437–445.

Soulsby, R. L. and Damgaard, J. S., 2005. Bedload sediment transport in coastal waters. Coastal Engineering, 52, 673–689.

Spinelli, G.A., Fisher, A.T., Wheat, C.G., Tryon, M.D., Brown, K.M., and Flegal, A.R., 2002. Groundwater seepage into northern San Francisco Bay: Implications for dissolved metal budgets. Water Resources Research 38, 10.1029/2001WR000827.

Styles, R., and Glenn, S. M., 2000. Modeling stratified wave and current bottom boundary layers on the continental shelf. Journal of Geophysical Research 105, 24119–24140.

Sutherland, J., Peet, A.H., and Soulsby, R.L., 2004. Evaluating the performance of morphological models. Coastal Engineering, 51, 917–939.

Taylor, S.E., Birch, G.F., and Links, F., 2004. Historical catchment changes and temporal impact on sediment of the receiving basin, Port Jackson, New South Wales. Australian Journal of Earth Sciences, 51, 233–246.

Temmerman, S., Govers, G., Meire, P., and Wartel, S., 2003. Modelling long-term tidal marsh growth under changing tidal conditions and suspended sediment concentrations, Scheldt estuary, Belgium. Marine Geology 193, 151–169.

Temmerman, S., Govers, G., Wartel, S., and Meire, P., 2004. Modelling estuarine variations in tidal marsh sedimentation: response to changing sea level and suspended sediment concentrations. Marine Geology, 212, 1-19.

Thomas, C.G., Spearman, J.R., and Turnbull, M.J., 2002. Historical morphological change in the Mersey Estuary. Continental Shelf Research, 22, 1775–1794.

Thompson, J., 1957. The settlement geography of the Sacramento-San Joaquin Delta, California. Ph.D. dissertation, Stanford University.

Tobin, A., Schoellhamer, D.H., and Burau, J.R., 1995. Suspended-solids flux in Suisun Bay, California. Proceedings of the First International Conference on Water Resources Engineering. San Antonio, Texas, pp. 1511–1515.

Umlauf, L., and Burchard, H., 2003. A generic length-scale equation for geophysical turbulence models. Journal of Marine Research, 61, 235–265.

Van der Wal, D., Pye, K., and Neal, A., 2002. Long-term morphological change in the Ribble Estuary, northwest England. Marine Geology, 189, 249–266.

Vargas, J.A., 1995. The Gulf of Nicoya Estuary, Costa Rica: past, present, and future cooperative research. Helgoland Marine Research, 49, 1-4.

Walling, D.E., 2006. Human impact on land-ocean sediment transfer by the world's rivers. Geomorphology, 79, 192–216.

Warner, J.C., Geyer, W.R., and Lerczak, J.A., 2005a. Numerical modeling of an estuary: a comprehensive skill assessment. Journal of Geophysical Research, 110, C050001.

Warner, J.C., Schoellhamer, D.H., Ruhl, C.A., and Burau, J.R., 2004. Floodtide pulses after low tides in shallow subembayments adjacent to deep channels. Estuarine, Coastal and Shelf Science, 60, 213–228.

Warner, J.C., Sherwood, C.R., Arango, H.G., and Signell, R.P., 2005b. Performance of four turbulence closure models implemented using a generic length scale method. Ocean Modelling, 8, 81–113.

Warner, J.C., Sherwood, C.R., Signell, R.P, Harris, C.K., and Arango, H.G., in review. Development of a three-dimensional, regional, coupled wave-, current-, and sediment-transport model. Computers and Geosciences.

Washington, W.M., Weatherly, J.W., Meehl, G.A., Semtner, Jr., A.J., Bettge, T.W., Craig, A.P., Strand, Jr., W.G., Arblaster, J., Wayland, V.B., James, R., and Zhang, Y., 2000. Parallel climate model (PCM) control and transient simulations. Journal Climate Dynamics, 16, 755–774.

Wilby, R.L., and Dettinger, M.D., 2000. Streamflow changes in the Sierra Nevada, California, simulated using a statistically downscaled general circulation model scenario of climate change. In: McLaren, S., and Kniveton, D., (eds.),Linking climate change to land surface change, Kluwer, Netherlands.

Williams, K., Ewel, K.C., Stumpf, R.P., Putz, F.E., and Workman, T.W., 1999. Sea-level rise and coastal forest retreat on the west coast of Florida, USA. Ecology, 80, 2045–2063.

Woodruff, J.D., Geyer, W.R., Sommerfield, C.K., and Driscoll, N.W., 2001. Seasonal variation of sediment deposition in the Hudson River estuary. Marine Geology, 179, 105–119.

Wright, L.D., and Nittrouer, C.A., 1995. Dispersal of river sediments in coastal seas: six contrasting cases. Estuaries, 18, 494–508.

Wright, S.A., and Schoellhamer, D.H., 2004. Trends in the sediment yield of the Sacramento River, California, 1957–2001. San Francisco Estuary and Watershed Science, 2, Article 2.

Wright, S.A., and Schoellhamer, D.H., 2005. Estimating sediment budgets at the interface between rivers and estuaries with application to the Sacramento-San Joaquin River Delta. Water Resources Research, 41, W09428, doi:10.1029/2004WR003753.

Zedler, J.B., and Callaway, J.C., 2001. Tidal wetland functioning. Journal of Coastal Research, Special Issue 27, 38–64.